UNIVERSITÉ DE LORRAINE

École doctorale IAEM Lorraine

Estimation de sources corticales : du montage laplacian aux solutions parcimonieuses
Cortical source imaging : from the laplacian montage to sparse inverse solutions

THÈSE

présentée et soutenue publiquement le 26 février 2016

pour l'obtention du

Doctorat de l'Université de Lorraine

Mention Automatique, Traitement du Signal et des Images, Génie informatique

par

Gundars KORĀTS

Composition du jury

Rapporteurs :	Lofti SENHADJI	LTSI, UMR 1099 Université de Rennes 1 - INSERM
	Christophe COLLET	iCube, UMR 7357 Université de Strasbourg - CNRS
Examinateurs :	Jérôme IDIER	IRCCyN, UMR CNRS 6597
	Valérie LOUIS-DORR	CRAN, UMR 7039 Université de Lorraine - CNRS
	Radu RANTA	CRAN, UMR 7039 Université de Lorraine - CNRS
	Steven LE CAM	CRAN, UMR 7039 Université de Lorraine - CNRS
Invité :	Louis MAILLARD	CRAN, UMR 7039 Université de Lorraine - CNRS, CHU Nancy

Centre de Recherche en Automatique de Nancy CNRS – UMR 7039

Université de Lorraine

I would like to express my gratitude to Ventspils City Council as well as Ventspils University College for financing my PhD studies in Nancy, France.

I also feel that my great colleagues Radu RANTA, Steven LE CAM and Valérie LOUIS-DORR together with all CRAN team deserve thanks for your ongoing support, leadership and making this work possible.

Spacial thanks to my family and friends, especially to Kristine BERGMANE who kept me going when I wanted to give up.

Contents

Résumé en français

L'étude des mécanismes cérébraux représente un enjeu capital pour la compréhension de ses fonctionnements et dysfonctionnements. Depuis la découverte de la présence de phénomènes électriques dans les hémisphères cérébraux de singes et de lapins par Adolf Beck en 1875, d'énorme progrès dans ce domaine ont été accomplis. Cependant, de nombreuses questions sur la façon dont cet impressionant calculateur biologique (environ 86 milliards de neurones dans le cerveau humain adulte) perçoit le monde et interagit avec son environnement restent ouvertes. Aujourd'hui, les avancées médicales et technologiques permettent de combiner des méthodes et des dispositifs de plus en plus évolués pour explorer ces fonctions et ces structures à différentes échelles temporelles et spatiales. Dans cette thèse, nous nous concentrons sur les phénomènes physiologiques à l'échelle macroscopique en exploitant des mesures non invasives électrophysiologiques de scalp (EEG). L'objectif de ce travail est d'estimer la localisation de sources électrophysiologique dans le cadre de potentiels évoqués par stimulation cognitive ou dans un cadre pathologique pour la localisation de sources épileptogènes.

L'activation des processus neuronaux se traduit en termes bio-physiologiques par la transmission de flux ioniques à travers les membranes cellulaires des neurones et des synapses. Ces échanges d'informations à l'intérieur des circuits neuronaux produisent des signaux électriques perceptibles: par exemple la localisation d'une augmentation de consommation d'oxygène ou la génération d'un champ électromagnétique découle des activités neuronales sous-jacentes et de leur dynamiques. Ces connaissances contribuent à la compréhension des mécanismes de commandes neuromotrices et cognitives humaines, ou encore à la modèlisation de comportements anormaux tels que ceux observés dans l'épilepsie ou la maladie de Parkinson. Dans ces derniers cas pathologiques, l'intérêt est aussi d'ordre clinique, où la délimitation précise de la structure responsable de la maladie dans le volume cérébrale est décisive pour le succès du traitement curatif, qu'il soit pharmaceutique et plus encore s'il est chirurgical.

Les récents développements technologiques dans le domaine de la neuro-imagerie non-invasive ont ouvert de nouvelles perspectives. Diverses méthodes d'investigation clinique peuvent être util-

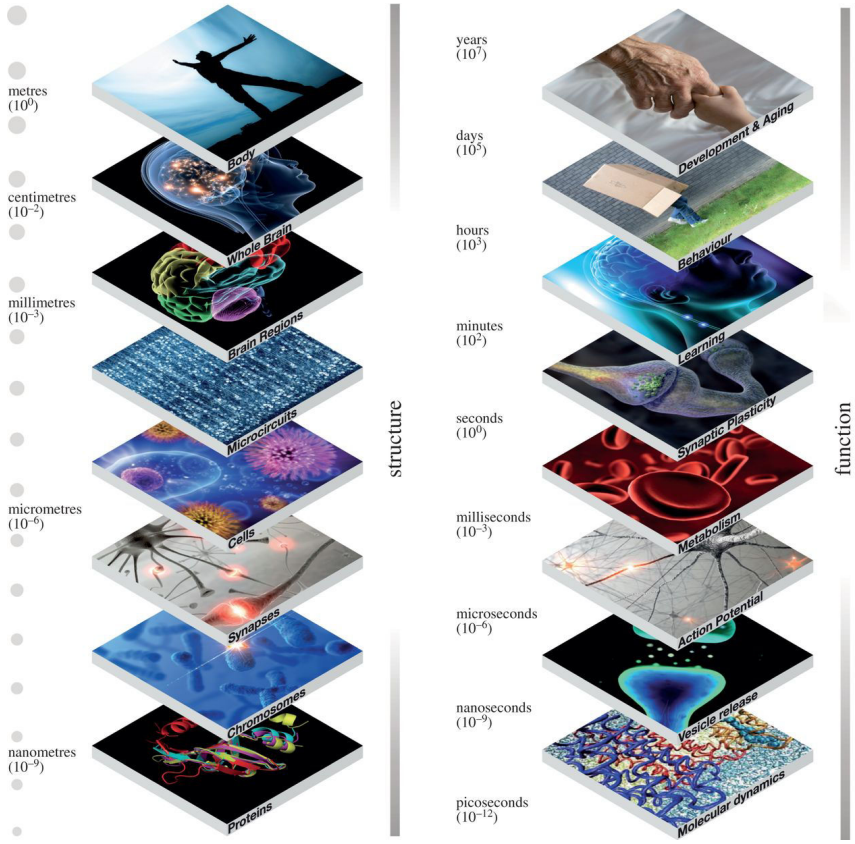

Figure 1: Le cerveau est un système intrinsèquement multi-échelle. Il peut être étudié à l'échelle du nanomètres (des protéines) jusqu'aux mètres (le corps humain). Evidemment les dynamiques temporelles des processus qui le constitue sont également très variables: cela peut aller de la picosecondes (pour les interactions atomiques) aux années (la durée de la vie d'un être humain). (41)

isés allant de modalités telles que l'imagerie (TEP, IRM) à la magnétoencéphalographie (MEG) et l'électroencéphalographie (EEG, la SEEG). Les mesures électroencéphalographiques ont le grand avantage de prodiguer une résolution temporelle de l'ordre de la milliseconde à l'échelle de la dynamique des processus étudiés, tout en restant une technique non-invasive utilisée en routine clinique. Cependant, la localisation des sources actives et la reconstruction de leur dynamique à partir de ces enregistrements EEG de surface restent un défi, et ce pour plusieurs raisons. La première est liée à leur faible résolution spatiale, offrant une vision superficielle du volume cérébral limitée à la surface supérieure de l'enveloppe corticale. La présence de l'os du crâne amplifie davantage cette difficulté, en atténuant fortement la propagation électrique des sources, où seules les sources les plus énergétiques restent visibles sur les enregistrements de surface. De plus l'EEG de scalp reste

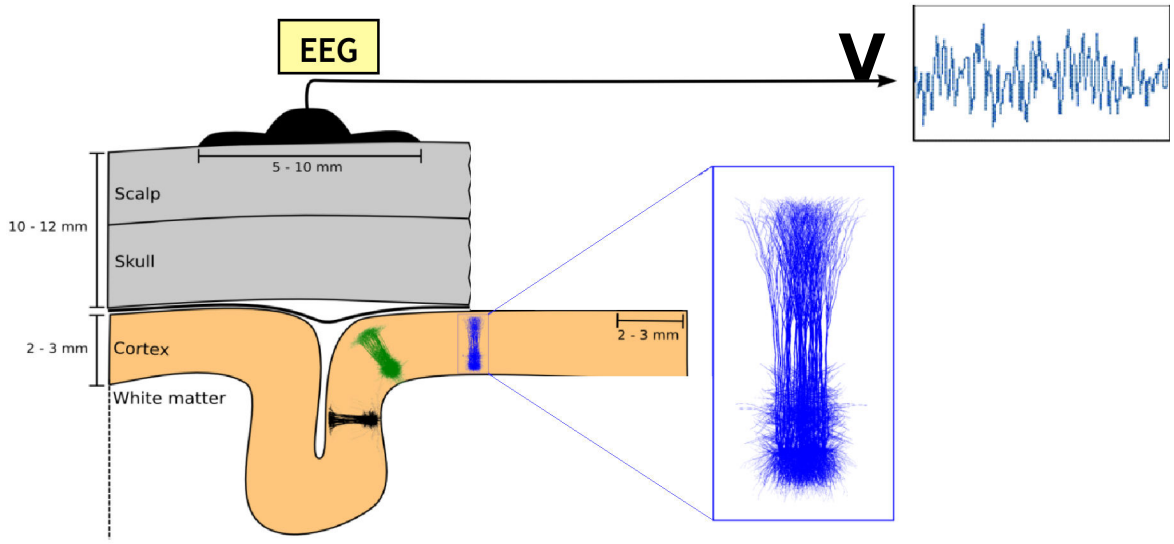

Figure 2: Diagramme schématique d'un EEG (mesures sur la surface de cuir chevelu(EEG de scalp)). Modifié de Einevoll G.T., BNNI2015.

une modalité particulièrement perturbée par des sources d'artefacts tels que l'electromyogramme , les clignements d'yeux... Pour ces raisons, nous avons restreint les objectifs de cette thèse à la reconstruction de cartes d'activation des sources corticales de surface. Cette reconstruction joue néanmoins un rôle important pour la compréhension des processus cérébraux que ce soit sur le versant fonctionnel ou pathologique. Cette reconstruction permet de relier l'activation de certaines zones corticales en réponse à un stimulus cognitif donné, et donc d'étudier les co-activations des réseaux fonctionnels sous-jacents. Il est également utile dans l'identification et la localisation des structures cérébrales pathologiques corticales superficielles .

Pourtant, et malgré ce cadre d'étude restreint, le nombre d'électrodes d'enregistrements reste faible au regard de la taille de l'espace des sources: l'ensemble du manteau corticale. L'imagerie de sources cérébrales est connue pour être un problème inverse particulièrement mal posé. De nombreuses méthodes ont été proposées pour régulariser ce problème, en intégrant des informations et des *a priori* bio-physiologiques de plus en plus précis. En particulier, on peut citer la conception de modèles de propagation toujours plus détaillés, atteignant un paroxysme avec l'utilisation de modèles numériques basés sur des méthodes par éléments finis, tenant compte à la fois des inhomogénéités des conductivités et du caractère non isotrope des tissus cérébraux, et ce voxel par voxel. Toutefois, la contribution réelle de telles cathédrales numériques reste difficile à quantifier, principalement en raison de fortes incertitudes liées à la segmentation des tissus, à l'estimation des conductivités, et à

de nombreux paramètres non observés, non intégrés ou volontairement négligés dans le cadre de la réduction de modéle.

A l'inverse, cette thèse commence par reconsidérer la pertinence d'une résolution du problème inverse lorsque peu d'informations sont disponibles à l'exception des seuls enregistrements EEG. Notre premier objectif est ainsi des méthodes se basant sur des caractéristiques basiques mais universelles portant sur la géométrie de la boîte cranienne humaine ainsi que sur la propagation physiologique des sources. Ces approches apparemment simplistes sont néanmoins rapides et robustes et fournissent des informations d'intérêt sur l'activation des régions corticales. En dépit des qualités pré-citées, nous reconnaissons que nous ne pouvons soutenir ce parti pris lorsque des informations anatomiques fiables sont à disposition. Il est certain que des informations plus précises sur les générateurs neuronaux et leurs dynamiques spatio-temporelles peuvent être extraites de la fusion d'informations issue des données EEG et des structures anatomiques, à condition que les *a priori* utilisés pour contraindre le problème soient en effet concordant avec l'électro-physiologie des phénomènes observés. Si il est vrai que cet organe est un important consommateur d'énergie, il a été prouvé qu'il régule très efficacement cette consommation, peu de structures cérébrales étant simultanément actives et présentant des durées d'activation très courtes. Nous explorons ainsi les approches produisant des activations parcimonieuses des aires corticales, tout en assurant la plausibilité physiologique de leurs décours temporels en tenant compte de leur aspect hautement non-stationnaire, de leurs caractéristiques temps-fréquences, ainsi que des possibles synchronisations entre sources.

Structure de la thèse, développements et résultats

Le premier chapitre du manuscrit est consacré à une brève introduction de l'anatomie du cerveau et sur l'état des connaissances actuelles sur le fonctionnement électro-physiologique cérébral à l'échelle des sources. Nous présentons ensuite diverses techniques d'acquisition de données d'imagerie, telles que l'Imagerie par Résonance Magnétique (IRM), la tomodensitométrie (CT) ainsi que l'imagerie par résonance magnétique fonctionnelle (IRMf). Nous abordons ensuite l'acquisition par magnétoencéphalographie (MEG), qui détecte et mesure les champs magnétiques émis au prix de très coûteux dispositifs médicaux. Puis nous décrivons la modalité électroencéphalographique (EEG), très couramment utilisé dans le contexte médical ainsi que dans les applications de type Interface Homme-Machine (IHM), du fait de la relative facilité de mise en œuvre de cette technique d'enregistrement. Nous présentons enfin quelques applications pour lesquelles l'identification des

structures activées sur la surface corticale est une condition préalable, motivant le sujet de cette thèse.

Du fait de sa haute résolution temporelle à l'échelle de la milliseconde, l'EEG est une modalité privilégiée pour analyser la dynamique des phénomènes neuronaux. Elle s'est avérée très utile pour l'extraction de divers indicateurs pertinents associés à des activités fonctionnelles ou pathologiques. Cependant, les questions liées à sa faible résolution spatiale et les incertitudes inhérentes au modèle de propagation utilisé rendent particulièrement difficile la reconstruction de sources à partir de cette modalité. Par conséquent, dans le deuxième chapitre, nous décrivons les nombreuses méthodes de la littérature consacrée à surmonter ces limitations. Tout d'abord, nous donnons un bref aperçu des techniques couramment utilisées pour résoudre le problème direct et construire un modèle de propagation. Ensuite, nous présentons et discutons différentes familles de méthodes permettant de résoudre le problème inverse. Nous commençons par décrire les méthodes basées sur le Laplacien de Surface (SL), qui reposent essentiellement sur les propriétés physiques de la propagation électromagnétique à travers la boite crânienne. Ces approches se montrent efficaces pour éliminer les distorsions et atténuations qui constituent la principale barrière de propagation des ondes électromagnétques . Nous introduisons ensuite les méthodes d'Imagerie de Sources Électriques (ESI), très largement étudiées et développées ces vingt dernières années. Ces méthodes sont dédiées à l'inversion de modèles de propagation, introduisant diverses contraintes afin de régulariser ce problème mal posé. Nous accordons une attention particulière à une sous-famille de ce type de méthodes qui visent à reconstruire la carte cortical en utilisant un nombre réduit de sources actives, se basant sur des stratégies d'optimisation de type Matching Pursuit pour imposer des contraintes de sparsité.

Inspirés par les approches de type Laplacien de Surface, nous proposons dans le chapitre 3 une interpolation des mesures surfaciques à l'aide de fonctions à base radiale. Ces fonctions de base sont construites en utilisant deux approximations différentes de la géométrie de la tête - plane et sphérique - produisant des projections physiologiquement plausibles (de type dipolaire) sur la surface corticale. L'opérateur d'interpolation est équivalent à l'inversion de matrice de propagation de rang plein (i.e., le nombre de sources et d'électrodes est identique), où les poids d'interpolation obtenus représentent les amplitudes estimées des sources. Il en résulte des cartes d'activation discrètes. En adoptant cette méthodologie, nous mettons en avant des liens évidents entre les approches par Laplacien de surface et les méthodes ESI classiques basées sur une contrainte de norme minimale, alors que ces deux approches apparaissent comme deux champs de recherche bien distincts dans la littérature. En simulation, les performances de l'estimateur proposé, que nous baptisons sous le nom d'Imagerie Corticale Dipolaire (ICD), sont comparées à des méthodes de type SL récentes et à une méthode

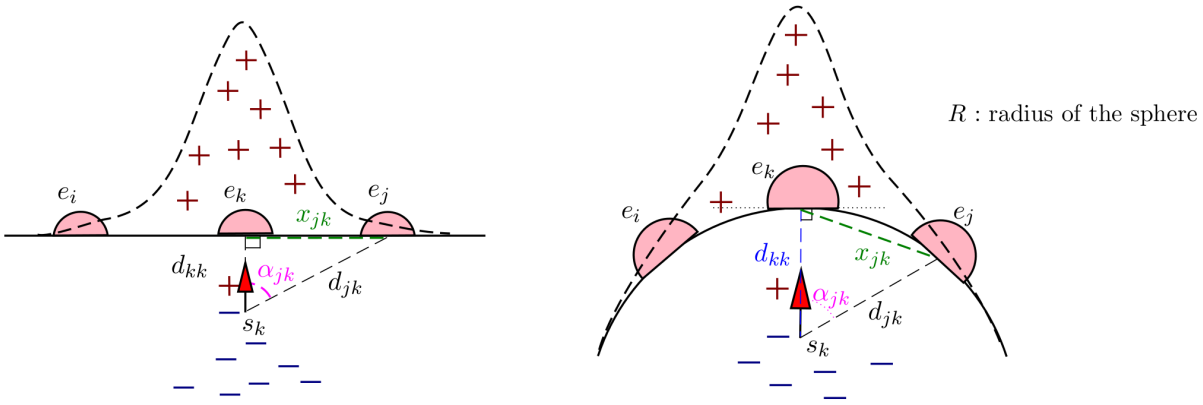

Figure 3: Les approximations géométriques de fonctions à base radiale sont utilisées pour l'interpolation plane et sphérique

de type norme minimale s'appuyant sur un modèle de propagation par éléments finis de frontière (BEM). Alors que l'approche d'imagerie basée sur le modèle BEM donne de meilleurs résultats lorsque

	Noise-free		20dB	
Method	64	128	64	128
DCM_p	0,85	0,88	0,84	**0,82**
DCM_s	0,87	**0,89**	**0,85**	0,80
DCM_{BEM}	0,94	0,95	0,85	0,48
SSL_s	**0,90**	0,86	0,78	0,56
SSL_g	0,89	**0,88**	0,79	0,62
MNE_{BEM}	0,94	0,97	0,73	0,23

Table 1: Moyenne (1000 évaluations) des performances pour de multiples patchs actifs simulés distribués aléatoirement sur la surface corticale. La corrélation entre les cartes corticales originales et les cartes estimées est utilisée comme critère de performance.

le rapport signal à bruit (RSB) est élevé, notre approche ICD est moins sensible au bruit et donne des résultats satisfaisants jusqu'à un RSB égal à 3 dB. Il procure des performances similaires lorsqu'il est comparé à des approches de type SL plus évoluées, tout en gardant une très faible complexité algorithmique et en se basant sur des considérations anatomiques et physiologiques très simplifiées.

L'approche ICD, bien qu'aisée d'implémentation, produit des cartes d'activation de faible résolution spatiale, et ne prend pas en compte les différences d'anatomie d'un patient à un autre. Dans le

chapitre 4, nous relâchons la contrainte de rang plein et nous plaçons des sources dipolaires candidates sur toute la surface corticale, produisant ainsi un modèle distribué. Nous résolvons le problème direct en implémentant un modèle par éléments finis de frontière (BEM). En conséquence la résolu-

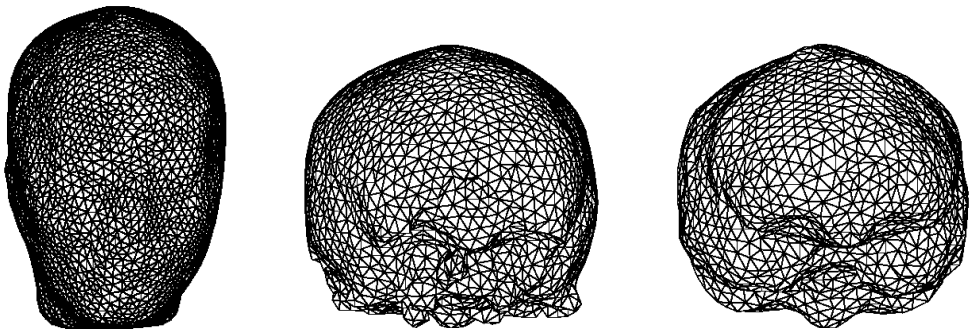

Figure 4: Modèle de BEM généré à partir de l'IRM d'un patient.

tion du problème inverse devient largement sous-déterminée. Les mesures de surface doivent être expliquées par une décomposition sur un dictionnaire d'atomes spatiaux très corrélés entre eux. En nous appuyant sur l'hypothèse physiologique selon laquelle peu de sources corticales sont simultanément actives, nous avons effectué des approches de type Matching Pursuit. Ces approches se sont révélées être efficaces pour cette même problématique d'estimation de sources cérébrales. Alors que généralement la décomposition est effectuée uniquement dans le domaine spatial en sélectionnant les dipôles qui expliquent le mieux les données, nous ajoutons une régularisation temporelle en construisant des dictionnaires combinant les domaines spatiales et temporelles. Les atomes temps/fréquences sont directement extraits des données EEG. Nous avons construit deux types de dictionnaires, soit en utilisant une Analyse en Composantes Principales (ACP), soit par une décomposition des signaux sur une base temps échelle ondelettes. L'optimisation est effectuée en utilisant deux algorithmes de type Matching Pursuit: l'algorithme Single Best Replacement (SBR), ainsi que l'algorithme Source Deflated Matching Pursuit (SDMP).

Dans le cas où les atomes sont extraits par ACP, la reconstruction de sources est satisfaisante lorsque les générateurs neuronaux simulés sont des processus stationnaires. Le principal inconvénient de cette méthode réside dans la charge de calcul, la taille du dictionnaire combinant les atomes temporels et spatiaux devenant rapidement très grande avec le nombre de composantes, monopolisant des ressources mémoires trop importantes. Le dictionnaire par ondelettes apporte lui des performances très intéressantes dans le cas de signaux non stationnaires tout en gardant une charge de calcul très limitée en terme de ressources algorithmiques, et ceci quel que soit le nombre

de sources considérées. Alors que la plupart des méthodes sont très sensibles à leur conditionnement

3dB	SBR_w	$SDMP_w$	SBR_t	$SDMP_t$	RMUSIC
GOF	**0.86**	0.46	0.57	0.56	0.81
DLE	**4.87**	11.17	10.25	8.22	4.92
FDP	**0.01**	0.19	0.30	0.34	0.05
TPR	0.95	**1.00**	0.72	0.85	0.96
FDR	**0.01**	0.45	0.13	0.13	0.03
Time	0.05	95.01	**0.04**	32.04	2.65

Table 2: (Space-time-frequency (wavelet coefficients) estimation using SBR compared to the popular and recent estimators. More detailed information about performance criteria is provided in thesis.)**Fréquence spatio-temporelle (coefficients d'ondelette) évaluation utilisant SBR comparé aux experts populaires et récents. On fournit des informations plus détaillées sur des critères de performance(prestation) dans la thèse.**

initial, souvent lié à une pré-estimation du nombre de sources, l'algorithme d'optimisation SBR combiné au dictionnaire par ondelettes montre une bonne robustesse aux erreurs de paramétrage.

Aux termes des chapitres 3 et 4, nous validons nos approches sur des données réelles fournies et expertisées par les neurologues du Centre Hospitalier Universitaire de Nancy affiliés au projet. Ces données EEG réelles ont été obtenues sur des patients atteint d'épilepsie pharmaco-résistantes au cours de la phase préopératoire. Les activités épileptiques observées sont de très courtes durées, et présentent des structures temps/fréquence bien localisées. Les localisations de sources corticales et les activités estimées sont validées par les experts neurologues et sont validées par les résultats post-opératoires. En effet les localisation estimées concordent avec la détermination de la zone épileptogène obtenue par exploration intracérébrale en Stéréo-EEG.

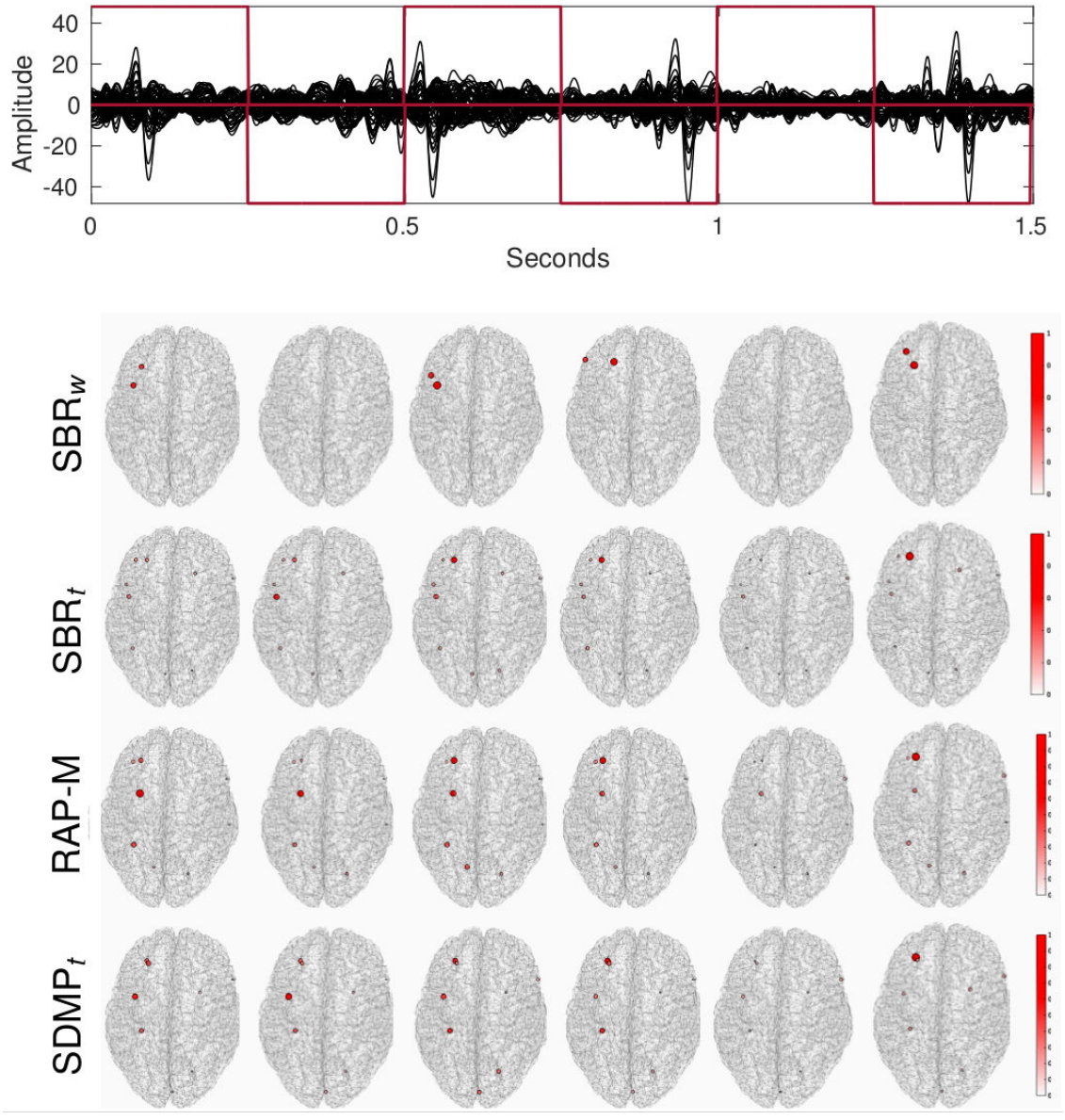

Figure 5: Performance(Prestation) de localisation sur signaux d'EEG passés de bande réels(vrais). Les emplacements Évalués correspondent aux pointes épileptiques.

Introduction

The study of the cerebral mechanisms represents a major challenge for the understanding of its functional and pathological processes. Since the first discovery of electrical phenomena within rabbits and monkeys cerebral hemispheres by Adolf Beck in 1875 (detailed in (122)), huge developments in this field have been made. However, numerous questions on how this impressive biological machinery (about 86 billion neurons in the adult human brain) perceives the world and interacts with its environment still remain open. Nowadays medical and technological development make it possible to combine complex methods and devices for the exploration of its structures and functions, resulting in the analysis of the human brain at different temporal and spatial scales. In this thesis, we focus on the physiological phenomena at the macroscopic scale by exploiting non-invasive electrophysiological scalp electrodes. The objective is to estimate the location of evoked-potential sources in response to a cognitive stimuli, or in a pathological context for locating epileptogenic zones.

Objectives and Approaches

The activation of neuronal processes is translated in bio-physiological terms by the transmission of ions through neurons and synapses. These exchange of information within the brain circuitry produce external signals, such as an augmentation of the oxygen consumption or the emission of an electromagnetic field, from which the locations of the underlying neuronal activities as well as their dynamics might be infer. Such identification is of first importance to understand how the brain governs motor and cognitive human abilities, or how pathological behaviors such as those observed in epilepsy or Parkinson's disease are appearing. In these last pathological cases, the interest is also of clinical order, where the precise delineation of the brain structures responsible for the disease is decisive for the success of the curative treatment, either surgical or pharmaceutical.

Recent technological developments in the field of non-invasive neuroimaging have opened up new path for studying the human brain functioning. Various methods of clinical investigation can be

used, from imaging modalities (PET, MRI) to electroencephalography (EEG, SEEG) and magnetoencephalography (MEG). The electroencephalographic (EEG) measurements have the great advantage to a resolution of the order of the millisecond, at the scale of the dynamic of the studied processes, while being a non-invasive technique often used in clinical routine. However the identification of the activated sources from EEG recordings remains an extremely difficult task, and this for several reasons. The first one is related to its low spatial resolution, providing a superficial vision of the brain volume almost limited to the upper surface of the cortical mantle. The presence of the skull further amplify this aspect, by strongly filtering the electrical propagation of the brain sources, only the most energetic sources being visible on the recordings. For these reasons, we have restrained the scope of this thesis to the reconstruction of cortical activation maps. Such reconstruction still plays an important role for the comprehension of the functional or pathological brain. It allows to relate the activation of particular cortical areas in response to a given cognitive stimuli, hence to study the co-activations of underlying functional networks. It is also helpful in identifying and localizing superficial pathological brain structures.

Still despite of this reduced framework, the number of recording electrodes is far less than the size of the source space. The source reconstruction is known to be a severely ill-posed problem (11). Numerous methods have been proposed to regularize this problem, by integrating more and more precise bio-physiological knowledge and priors. In particular, the available computing resources allows to design more and more detailed propagation model, based on finite elements methods, taking account of the conductivity inhomogeneities as well as the anisotropy of the brain medium, voxel by voxel. However, the true contribution of such complex model is difficult to quantify, mostly due to high degree of uncertainty related to the segmentation of the brain tissues, to the estimation of their associated conductivities, and to numerous unobserved or neglected parameters.

In the beginning of this thesis is challenged the possibility of solving the inverse problem with poor or simplified anatomical information in addition to the EEG recordings. The first objective is to study the performance of easily implementable methodologies, based on basic but universal features of the human head geometry as well as minimalist assumptions about the physiological propagation of the sources. We argue that such seemingly simplistic approaches are fast and robust while still providing exploitable information on the cortical activations. Despite its indisputable advantages, we acknowledge that we cannot support such partial point of view when reliable anatomical informations are within reach. There is no doubt that more precise information about the individual neural generators or their spatio-temporal dynamics can be extracted from these combined (EEG and anatomical) data, on condition that the priors used to constrain the problem are indeed concordant

with the electro-physiology of the brain. While it is true that this organ is a greedy energy consumer, this organ regulates very efficiently its energy consumption, meaning that few brain structures are simultaneously active and that these activations are of short durations. Pursuing our philosophy of developing economical methods involving limited number of parameters, we explore approaches producing sparse activations of the cortical map, while ensuring the physiological plausibility of their time-courses by taking into account their highly non-stationary aspect, their specific time-frequency characteristics, as well as the source synchronizations that may appear.

Thesis Structure

The first chapter is dedicated to a brief introduction to the brain anatomy and to the state of current knowledge on cerebral electro-physiological functioning. We then present various brain image acquisition techniques, such as Magnetic Resonance Imaging (MRI), Computer Tomography (CT) as well as functional Magnetic Resonance Imaging (fMRI). We explain the brain activity measurements using magnetoencephalography (MEG), which detects the magnetic fields of the brain at the cost of highly expensive medical devices. We then describe the electroencephalogram (EEG) modality, which is commonly used in medical context as well as in brain computer interfacing (BCI). Due to the accessibility and popularity of this modality, we focus in this thesis on the resolution of the inverse problems from these non-invasive scalp EEG data. We finally present few applications for which the identification of activated structure on the cortical surface is a prerequisite, motivating this thesis.

Due to its high temporal resolution at the scale of the millisecond, the EEG is a privileged modality for analyzing the fast dynamics of the neuronal phenomena. It has shown to be very useful in extracting relevant indicators of different brain fonctional or pathological activities. However, the questions related to its poor spatial resolution and to the uncertainties inherent to the used propagation model make the sources reconstruction a particularly difficult task. Therefore, in the second chapter we describe the numerous methodologies from the literature dedicated to overcome these limitations. First, we give a brief overview of the current used technics to solve the so-called forward problem and to build a propagation model, from analytical to numerical models. Then we present and discuss different families of method for solving the inverse problem. We begin by describing the surface Laplacian (SL) methodologies (32, 68, 100), which rely on the physics of the electromagnetic propagation through the skull, and is efficiently used to remove the distortion and blurring effects caused by this poorly conducting bone. The output of the SL are cortical potentials on a complete surface (interpolated) or at the discrete points underneath the scalp surface electrodes. We

then introduce the Electrical Source Imaging (ESI) family of approaches, which has been extensively studied in the past twenty years (11, 52, 85, 91). These methods are dedicated to the inversion of a given propagation model, introducing various constraints to regularize this ill-posed problem. We give particular attention to a sub-family of methods which aim at reconstructing the scalp map based on a few number of active sources, taking benefit of Matching Pursuit optimization strategies to impose this constraint of sparsity.

We reconsider the problem of cortical source imaging using exclusively the electrical activities provided through the EEG scalp measurements, assuming simplified geometry of human head, named as dipolar cortical mapping (DCM). The resulting full-rank estimators are applied on the data, which in fact resembles the interpolation-based Surface Laplacian (SL) methods which rely on the assumption that the scalp potential map is a linear combination of smooth basis functions produced by the underlying sources. We want to emphasize that, in a similar manner as SL approaches, our proposed DCM is not informed with the conductivity information. The true amplitudes are not estimated but rather the activation map that correlates with the true cortical potentials. In the contrary to SL, we propose parametrized families of interpolating functions physiologically informed.

Despite that the DCM is easily implementable full-rank estimator and does not requires complex anatomical information, thus the particularism of each patient brain anatomy is not taken into account. Therefore it provides unprecise activation maps. To overcome this, further in the thesis we relax the full rank constraint by adopting a dipolar distributed model along with a Boundary Element Modeling (BEM) of the head. The inversion of this model is regularized using a constraint of parsimony, based on the physiological assumption that only a few cortical sources are simultaneously active. Such hypothesis is particularly valid in e.g., epileptic context or in the case of cognitive tasks, where a limited number of sources are responsible of the visible activity on the EEG electrodes. The novelty of this thesis comes from the fact that sparse estimate takes into account both the spatial and the temporal dimension of the data. As a result two combined spatio-temporal dictionaries are introduced. In the first case, the temporal atoms are extracted from the data using classical principal component analysis. For the second dictionary we exploit a wavelet decomposition of the data, being more robust to noise and well adapted to the non-stationary nature of the electrophysiological data. The production of the sparse solutions is carried out using two recent sparse optimization schemes called Single Best Replacement (SBR) and Source Deflating Matching Pursuit (SDMP).

In both of the chapters we evaluate the performance of the approaches and we compare them with standard methods of the literature. We also provide validation on real clinical data, provided and expertised by the neurologists of the Centre Hospitalier Universitaire (CHU) of Nancy affiliated

to the project. These real data are related to the recordings of an epileptic patient. Such pathology produces synchronized brain activities of short durations, with very characteristic time-frequency structures, bringing a challenging context for the validation of our source reconstruction methods.

Chapter 1

Human Brain Electrophysiology

1.1 The Brain

The human body is a very complex organism controlled by the nervous system which consists of the brain and spinal cord, together known as the central nervous system (CNS), and the peripheral nervous system or nerves. As shown in **Figure** 1.1, human nervous system can be seen in different spatial scales starting from the molecular level and ending with a multi-physical integrated system. The whole nervous system controls every single part of the body. Although the main principles of the nervous system are known, according to the current knowledge the system itself is still too complex to fully understand all its underlying processes. To understand the core of such complex system researchers focused on both the biological aspects as well as the functional aspects of the human brain in order to relate different motor (movements) and cognitive activities with corresponding measured electrical neural activities. It is important to notice also that, in addition to the spatial scales, one needs to consider also a wide spread of temporal scales that varies from miliseconds for synaptic processes to years for the whole body, when different parameters of ageing is observed.

It is observed that the neural activity of the human fetus starts within the second trimester, more precisely between the 17th and 23rd week. From this early stage and throughout life electrical signals generated by the brain represent not only the brain function but also the state of the whole body (108). This observation is the basis of the motivation to apply advanced digital signal processing methods on the electroencephalogram (EEG) signals generated by the brain and measured on the scalp surface. The idea is to extract specific temporal and/or spatial characteristics of the underlying neural population activity from scalp EEG, as it will be shown further in the following chapters of the thesis. In this very first chapter we will introduce the fundamentals of anatomical aspects of

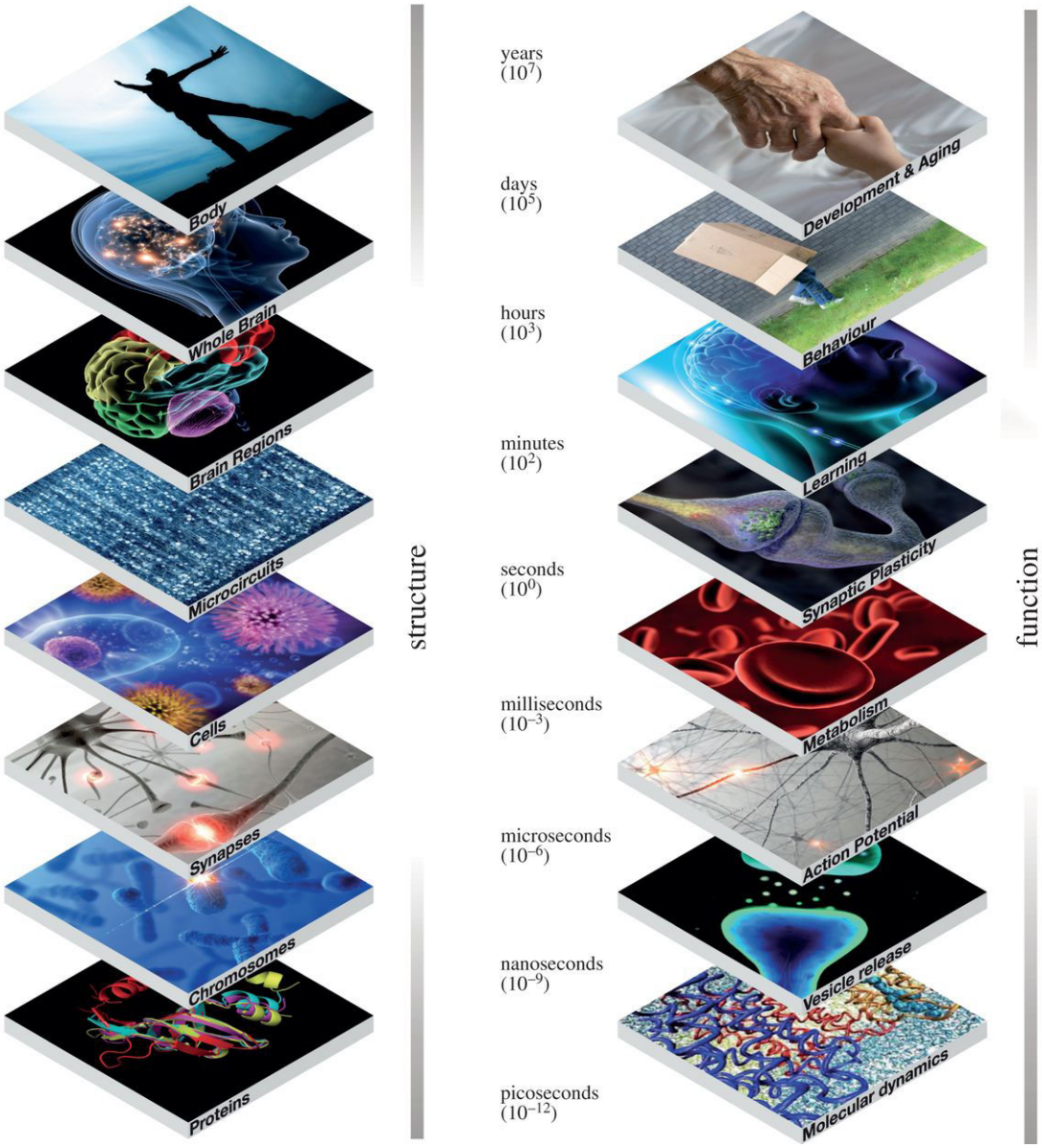

Figure 1.1: The brain is an intrinsically multi-scale, multi-level organ operating across spatial scales ranging from nanometres (proteins) to metres (the human body) and temporal scales from picoseconds (atomic interactions) to years (the lifespan of a human being). (41)

the brain and the concept of underlying neural activity. Afterwards we will show the most popular non-invasive concept of EEG measurements. Finally we will introduce different forward modelling techniques that are used to model conductive human head and its inner structures.

1.2 Anatomy

1.2.1 Brain structure

In principle, brain is subdivided into two almost equal hemispheres (**Figure** 1.2)- left and right where the hemispheres communicate with each other through a thick band of 200-250 million nerve fibers called the *corpus callosum* (1): Further each hemisphere is subdivided into four lobes (**Figure** 1.3)

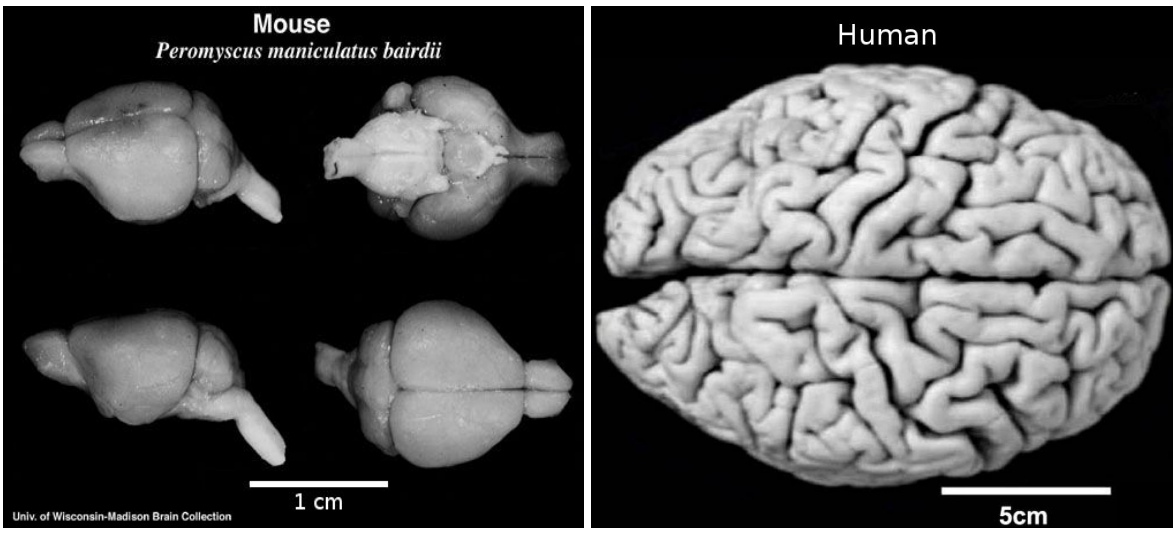

Figure 1.2: Mouse brain (NASA) VS human brain (Medexpress). One can easily notice the very different structure between human and mouse. Due to the fact that the human brain contains much more neurons, folded structure is forming in order to allow bigger number of neurons thus enables much higher cognitive ability.

which are frontal, parietal, temporal and occipital, together forming the larger superior region of the brain called *cerebrum*. Each of the lobe is responsible for following functions:

- frontal lobes: contains most of the dopamine-sensitive neurons in the cerebral cortex that is associated with reward, attention, short-term memory tasks, planning, and motivation. Dopamine-sensitive neurons tends to limit and select sensory information arriving from the thalamus to the forebrain (79).

- parietal lobes: manage sensation, handwriting, and body position. The most of the sensory inputs from the skin caused by touch, temperature, and pain receptors, relay through the thalamus to the parietal lobe;

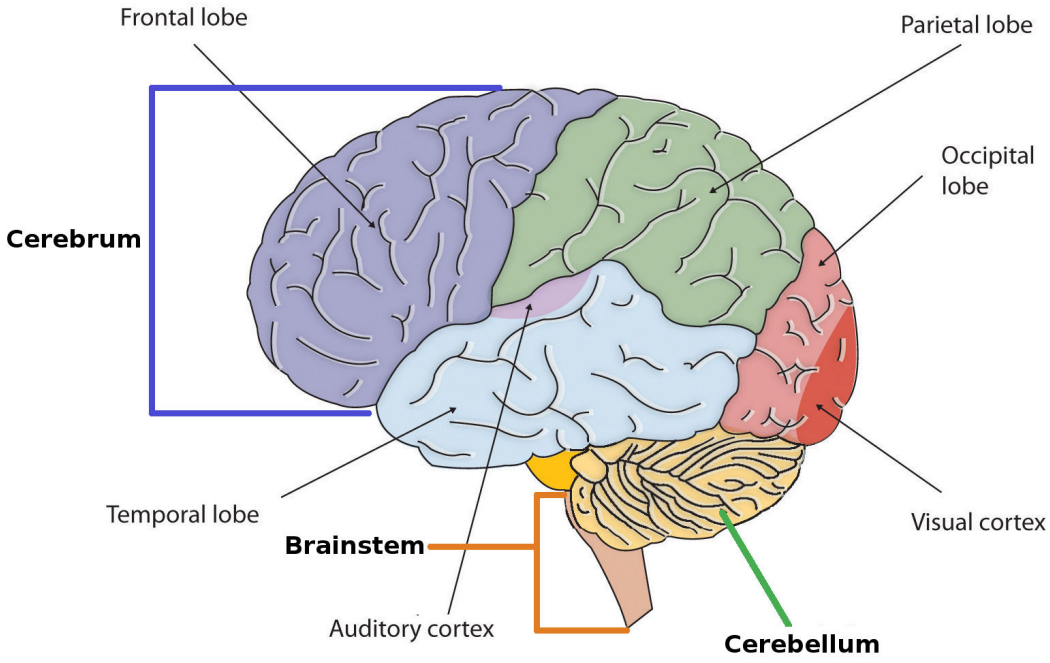

Figure 1.3: External view of brain with 3 main parts (cerebrum, brainstem, cerebellum) where cerebrum can be separated in four lobes (temporal, frontal, occipital, and parietal) (39).

- temporal lobes: manage the language, memory, hearing and the visual recognition of the objects (79, 117);
- occipital lobes: contain the brain's visual processing system (38).

The lobes were named of the overlying skull bones and were defined long before anything significant was known about the functional specialization of the cerebral cortex (79).

The diagram in **Figure** 1.3 also shows that in addition to the *cerebrum* cortical layer, the brain is also composed of the *cerebellum* and the *brainstem*. The brainstem (brains stalk) is the structure through which nerve fibres rely signals called action potentials (AP) in both directions between the spinal cord and higher brain centres. It should be pointed out that in the middle of the brain is located the *thalamus*, which is composed of two egg-shaped structures at the top and to the side of the brainstem. The Thalamus is a rely station and important integrating centre for all sensory input to the cortex except smell. The cerebellum, located at the top and the back of the brainstem,

is associated with the control of muscle movements. More recently, the cerebellum has been shown to play additional role in cognition (79).

1.2.2 Neocortical layer

The outer portion of the cerebrum, the cerebral cortex (called as neocortex and is developed in all mammals), is a folded structure varying in thickness from about 2-5mm, having a total surface area of roughly 1600 to 4000 cm^2. An interesting property of the cortical neurons is that they are strongly interconnected. According to (96), the human brain contains around 86 billion neurons interconnected with individual networks of other neurons.

Therefore it is estimated that for an average adult there are 10^{14} - 10^{15} synapses. The average number of neocortical neurons was estimated to be 19 billion in female brains and 23 billion in male brains. Due to the fact that cortex contains predominance of cell bodies, it turns gray when stained by anatomists, but remains pink when alive. For this reason cortical layer is called also the *gray matter*. Under the gray matter lies the *white matter*, which consists of nerve fibers (axons) conducting the information among neurons. In humans, white matter interconnections between cortical regions are quite numerous. Each centimeter of human neocortex may contain 10^7 input and output fibers interconnecting different regions of the cortex (79, 108).

1.2.3 Neuron

1.2.3.1 General structure

In **Figure** 1.4 is shown the diagram of typical neuron cell. The structure of a neuron cell is the following:

- the **cell body** (called also as *soma*) contains the cellular nucleus and cytoplasm which surrounds it. The soma ensures the synthesis of the components necessary to the functioning of the neuron;

- a **dendrite** is the branched projection of a neuron (dendrite tree), which allows the propagation of the related electrical signals. Dendrites act as receptors for the neuron;

- an **axon** is a long prolongation dedicated to the potential transmitter towards the other neurons;

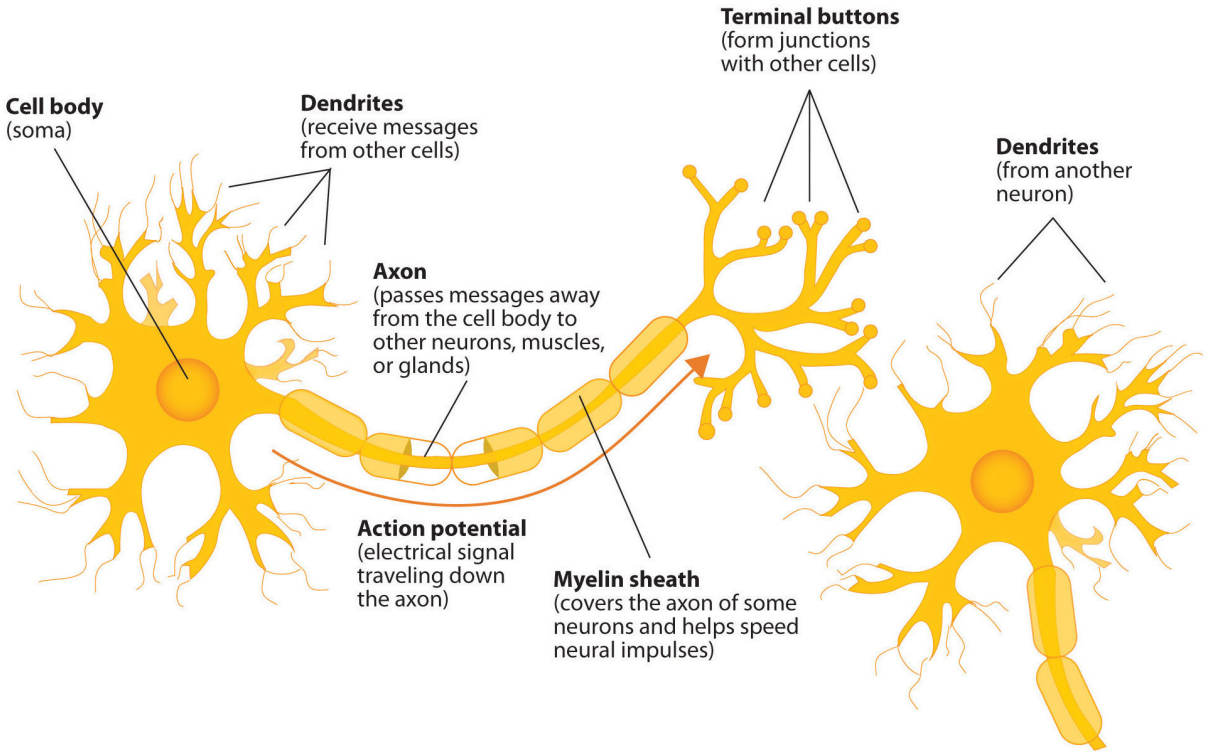

Figure 1.4: Diagram of neuron (118)

- **terminal buttons** (small knobs at the end of an axon) are responsible for releasing the chemicals called neurotransmitters into the synapses, which ensure communication between neurons.

In fact each neuron cell is responsible for the transmission of the information by generating and transmitting flux nerve impulses in the brain. In such manner neurons are "firing" and once large group of neurons are firing together, local neocortical region becomes active. Although to measure such activity on the scalp the local region must be strong enough to penetrate such poorly conducting anatomical layers as skull bone. Further in this chapter we will briefly discuss such type of neurons that are able to produce such measurable potentials.

1.2.3.2 Pyramidal neuron

Pyramidal neurons are found in most mammalian forebrain structures, including the cerebral cortex, the hippocampus and the amygdala, but not the olfactory bulb, the striatum, the midbrain, the

hindbrain or the spinal cord. Thus, they are found primarily in structures that are associated with advanced cognitive functions, and an understanding of these neurons is necessary to elucidate the neural bases of such sophisticated functions (116). In the neocortical layer the pyramidal neurons are well aligned, i.e. they are structured parallel to each other and in fact are perpendicular to the cortical surface (81). As it will be explained further, this particular spatial organization plays a critical role in the localization approaches.

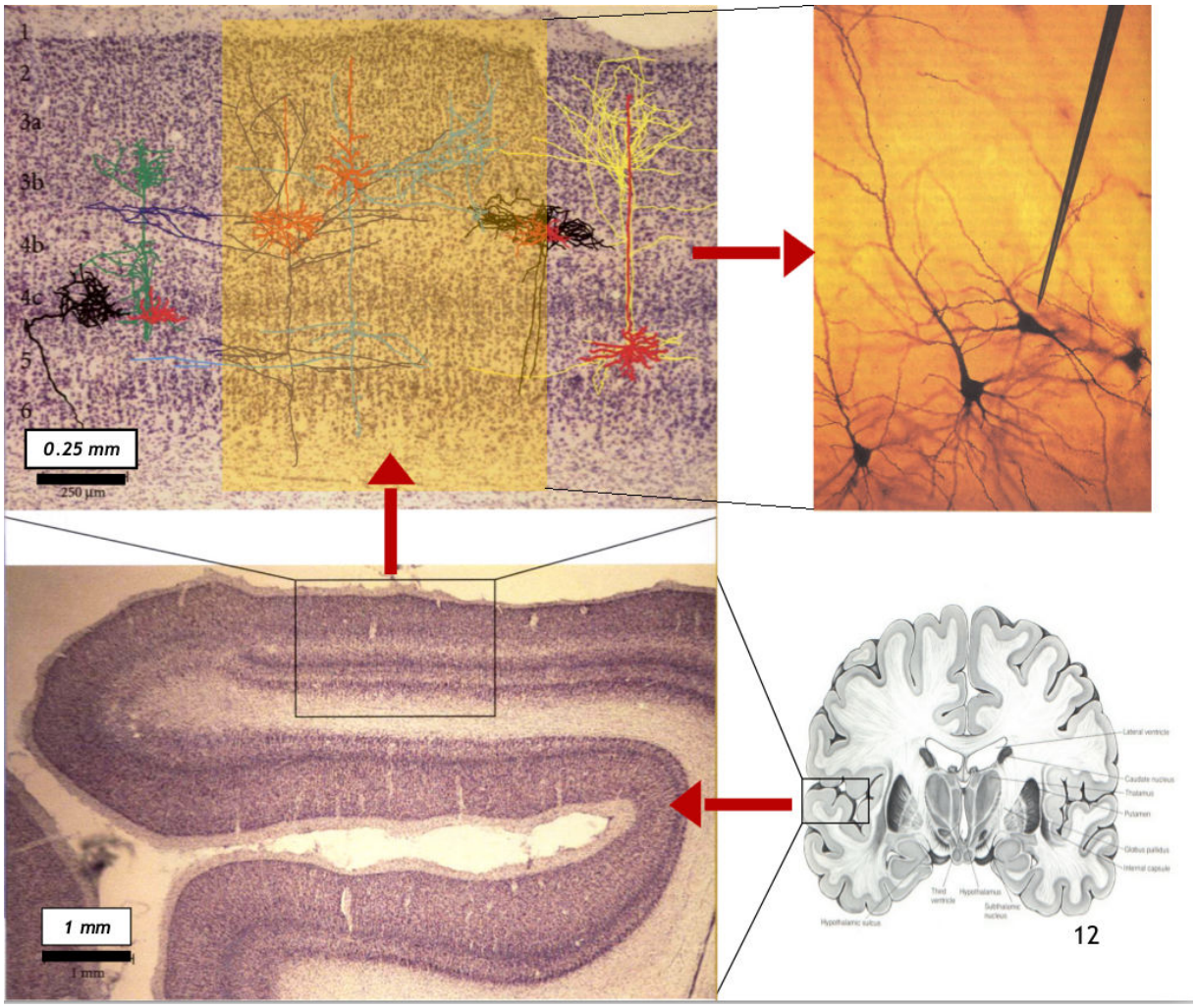

Figure 1.5: Pyramidal neurons in the cortical layer (44). Bottom-right corresponds to the slice of the human brain. Small cortical region is zoomed in bottom-left corner. Again even smaller scale of the cortical layer is shown in top-left figure where multiple pyramidal neurons are coloured in black, yellow, green, red and blue colours. Finally in the top-right corner real pyramidal neurons with laminar electrode is shown.

Till now we introduced the fundamental structure of the brain in different scales. In cellular level we showed that brain consists of neurons that allows to propagate the information through the brain. Further we will discuss the activity of neural generators which consists of large neuron groups that are synchronized and, thus, are able to produce measurable electrical potential.

1.2.4 Anatomic imaging techniques

In vivo and for our application, the head and brain anatomy of the explored patients is usually explored using imaging techniques such as computerized tomography (CT or scanner) and magnetic resonance imaging (MRI).

Computerized tomography (CT) (67) is an imaging procedure that uses specialized X-ray equipments that allow to obtain detailed scans (images) of areas inside the body. It is also called computerized tomography and computerized axial tomography (CAT). CT may involve the use of a contrast (imaging) agent, or "dye" that can be either injected into a vein or taken orally before the procedure. The contrast dye highlights specific areas inside the body, resulting in clearer pictures. Iodine and barium are two dyes commonly used in CT.

Magnetic Resonance Imaging (MRI) (37) is a technique that uses a magnetic field and pulses of radio wave energy to investigate the anatomy and physiology of the organs and structures inside the body. In our context, it is often used to extract the mathematical geometrical models of the patients head and inner structures, which is later used in different optimization schemes to solve the inverse problem. In other words the MRI is used as an auxiliary information to improve the performance of patient dependent inverse solvers.

1.3 Bioelectrical brain physiology

Understanding of neuronal functions and neurophysiological properties of the brain together with the mechanisms underlying the generation of signals and their recordings is vital for those who use such recordings for detection, diagnosis, and treatment of brain disorders and the related diseases where the human life is at stake of correct interpretation of processed data (108).

Differences of electrical potentials are caused by summed post-synaptic graded potentials from pyramidal cells that create electrical dipoles (**Figure** 1.6) between soma and apical dendrites (neural branches). Brain electrical current consists mostly of Na^+, K^+, Ca^{++}, and Cl^- ions that are pumped through channels in neuron membranes in the direction governed by membrane potential (69, 126). Only large populations of active, time synchronized and spatially aligned neurons can generate elec-

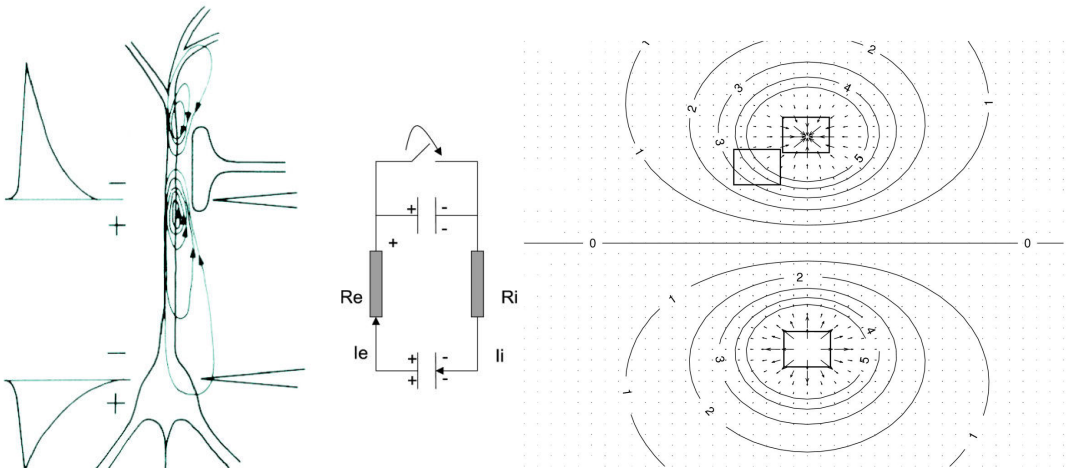

Figure 1.6: Equivalent circuit for a neuron. Left-an excitatory post synaptic potential, an simplified equivalent circuit for a neuron, and a resistive network for the extracellular environment. A neuron with an excitatory synapse at the apical dendrite. Middle-a simplified equivalent circuit is depicted. Right-the current density and equipotential lines in the vicinity of a dipole. The current density and equipotential lines in the vicinity of a current source and current sink is depicted. Equipotential lines are also given. Boxes are illustrated which represent the volumes Ω. (60).

trical activity recordable on the head surface. Thus a single electrode provides estimates of synaptic action averaged over tissue masses containing between roughly 100 million and 1 billion neurons. In fact, the extra-cranial recordings captures the neural activity which were affected fortuitously by the complex anatomical structures and the background activity of the brain, which in terms of source estimation is assumed as noise. On the other hand, much more detailed local information with the cost of spatial coverage may be obtained from intra-cranial electrodes implanted in living brains, thereby loosing the "big picture" of brain function. Furthermore, the dynamic behaviour of intra-cranial recordings depends fundamentally on the measurement scale, determined mostly by electrode size. Different electrode sizes and locations can result in substantial differences in recorded dynamic behaviour, including frequency content and coherence. In practice, intra-cranial electrical potentials might provide different information, than the one obtained from the scalp (79).

As mentioned, for these fields to be measured at a certain distance from the sources, it is important that the underlying neuronal currents are well organized both in space and time. According to Lopes Da Silva (80), at the macroscopic level, the activation of a set of neurons organized in parallel is capable of creating dipole layers. Important conditions that have to be satisfied for this to occur are the following:

- neurons should be spatially organized with the dendrites aligned in parallel, forming palisades,
- synaptic activation of the neuronal population should occur simultaneously.

In the neocortex, the small volume corresponds to hypothetical cortical modules, for example mini or macro columns with mostly parallel organized layers of principal cells and numerous interneuron types (22). Brain regions with parallel arranged dendrites and afferents, such as cortical structures, give rise to large amplitude extracellular potentials, whereas subcortical nuclei with a less orderly spatial organization generate *closed fields*, *i.e.*, small-amplitude field events. A fundamental property of a neuronal network is the capacity of the neurons to work in synchrony. This depends essentially on the way the inputs are organized and on the network inter-connectivity. Thus, groups of neurons may work synchronously as a population due to mutual connections (80).

Equivalent dipole

As determined previously all excitation and inhibition processes on the neuronal level are primarily mediated by transmembrane current flow. In fact Maxwell equations and volume conduction theory is used in order to explain the resulting secondary current and potential distribution everywhere within and on the surface of the head. Because intracranial current flow in a macroscopic scale is relatively slow in physical terms and because the brain is a good conductor, the quasi-static approach can be used, *i.e.*, current loops are closed, meaning that there is as much current flowing out of an activated neuron as there is flowing in from the extracellular space (111). Although in the microscopic scale the distribution of these current sources and sinks is very complex, at the macroscopic level, as seen for example on the distant measurements such as scalp electrodes, the situation looks much simpler. Hence the distant field can be thus approximated as a current dipole (111). This assumption is used in this thesis where dipolar point-type sources are used in order to explain the underlying cortical activity.

1.4 Functional activity measurements

Different invasive and non-invasive techniques exist for measuring and detecting the neural activity of the brain. Depending on the temporal or spatial resolution one might choose the best that suits the application. In this thesis we focus on non-invasive techniques such as EEG which is briefly explained further.

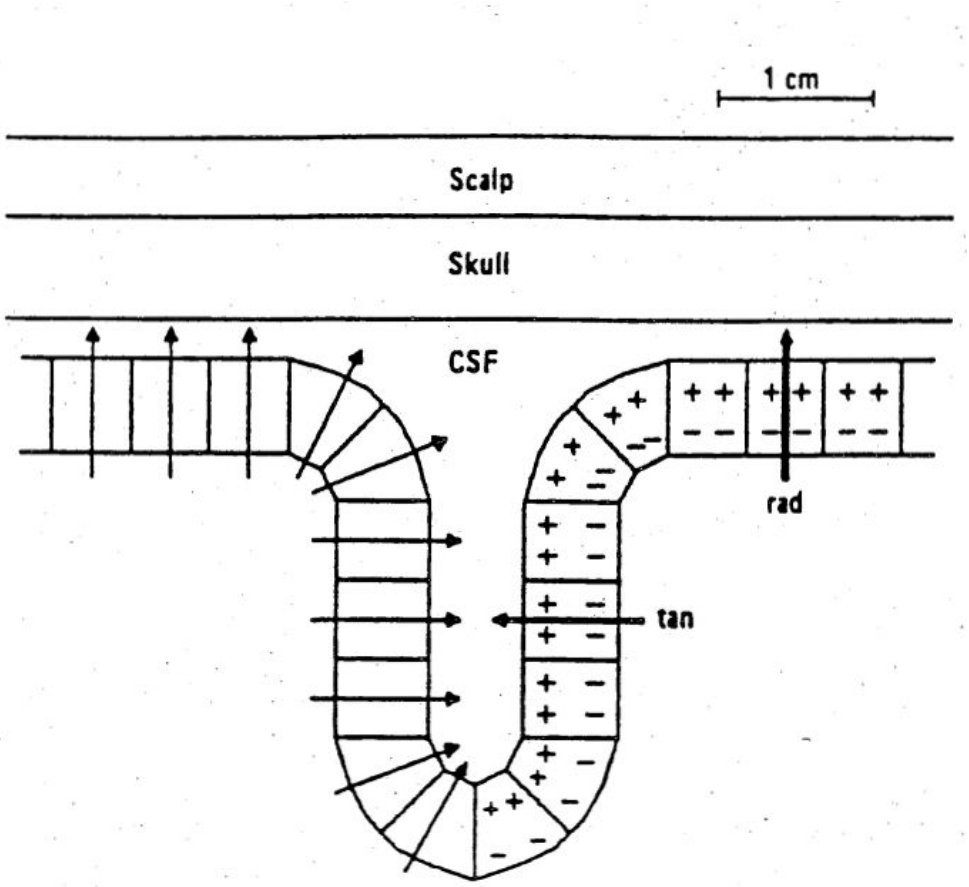

Figure 1.7: Schematic diagram of a cortical fold. Due to the columnal organization of the cortex, current sources (+) and sinks (-) are displaced perpendicular to the cortical surface. This results in radial dipoles for superficial cortical segments, in tangential dipoles for fissural segments and in oblique dipoles for the banks of fissures or differently oriented fissural segments. A single radial and single tangential equivalent dipole give a good approximation for the compound activity of all cortical segments on one side and in vicinity of a cortical fold (right) (111).

1.4.1 Electromagnetic measurements

1.4.1.1 Surface electroencephalography

Electroencephalogram, first introduced by Berger in (15), is a technique to record neural oscillations in time (**Figure** 1.8) using only scalp surface placed electrodes. Those recorded oscillations provides a very large-scale and robust measures of neocortical dynamic function. EEG is able to measure mostly the currents that flow during synaptic excitations of the dendrites of many synchronized pyramidal neurons in the cerebral cortex.

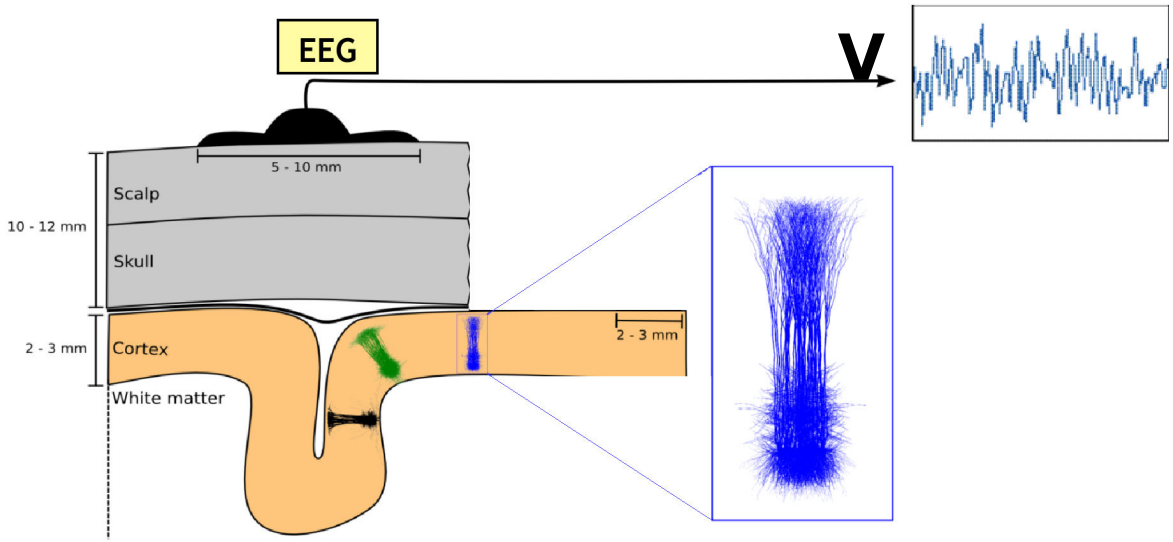

Figure 1.8: Schematic diagram of an EEG (measurements on the scalp surface) and ECoG electrodes (measurements directly on the cortex) (44).

EEG systems consist of a certain number of electrodes, a set of differential amplifiers (one for each channel) followed by filters, and and a recording device, nowadays digital, with sampling frequencies usually going from minimum 256 to 4096 or more Hz. In clinical routine, the signals are analyzed, with rare exceptions, up to at most 100 Hz.

The EEG recording electrodes and their proper function are crucial for acquiring high quality data. Different types of electrodes are often used in the EEG recording systems, such as:

- disposable (gel-less, and pre-gelled types);
- reusable disc electrodes (gold, silver, stainless steel, or tin);
- headbands and electrode caps;
- saline-based electrodes;
- needle electrodes.

For multichannel recordings with a large number of electrodes, electrode caps are often used. Commonly used scalp electrodes consist of Ag-$AgCL$ disks, less than 3 mm in diameter, with long flexible leads that can be plugged into an amplifier. Needle electrodes are those that have to be implanted under the skull with minimal invasive operations. High impedance can lead to distortion, which can even mask the actual EEG signals (108).

The international Federation of Societies for Electroencephalography and Clinical Neurophysiology has recommended the conventional electrode setting called as 10-20 system for 21 electrodes (excluding the earlobe electrodes), as depicted in **Figure** 1.9 (87). The 10-20 system avoids both

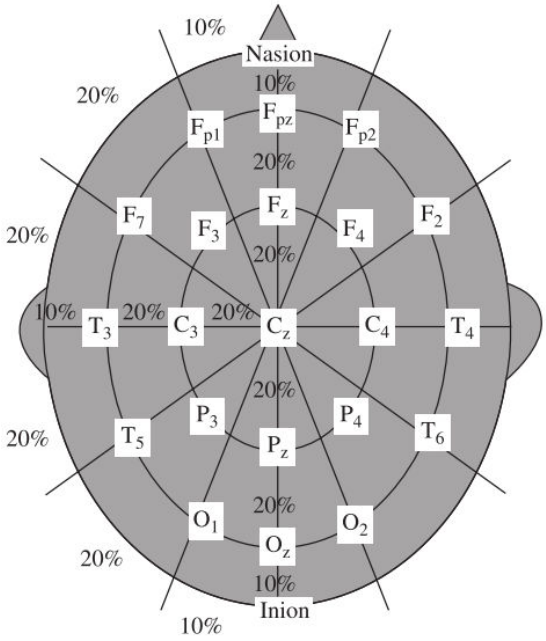

Figure 1.9: Conventional 10-20 EEG electrode positions for placement of 21 electrodes.

eyeball placement and considers some constant distances by using specific anatomic landmarks from which the measurement would be made and then uses 10 or 20% of that specified distance as the electrode interval. The odd electrodes are on the left and the even ones on the right sides of the head. For setting a larger number of electrodes using the above conventional system, the rest of the electrodes are placed in between the above electrodes with equidistance between them (87, 108). In some applications such as ERP analysis and brain computer interfacing a single channel may be used. In such applications, however, the position of the corresponding electrode has to be well determined.

In another similar setting, called the Maudsley electrode positioning system, the conventional 10-20 system has been modified to capture better the signals from epileptic foci in epileptic seizure recordings. The only difference between this system and the 10-20 conventional system is that the outer electrodes are slightly lowered to enable better capturing of the required signals. The advantage of this system over the conventional one is that it provides a more extensive coverage of the lower part of the cerebral convexity, increasing the sensitivity for the recording from basal subtemporal structures (17).

In **Figure** 1.10 is shown the neural activity measured by individual scalp EEG sensors. In fact each senor registers the mean activity of some local neighborhood and thus, with the resolution of electrode sampling (number of electrodes), we obtain the approximated time-courses of the cortical activity seen by the electrodes. In the context of time analysis, the term *rhythm* is used when

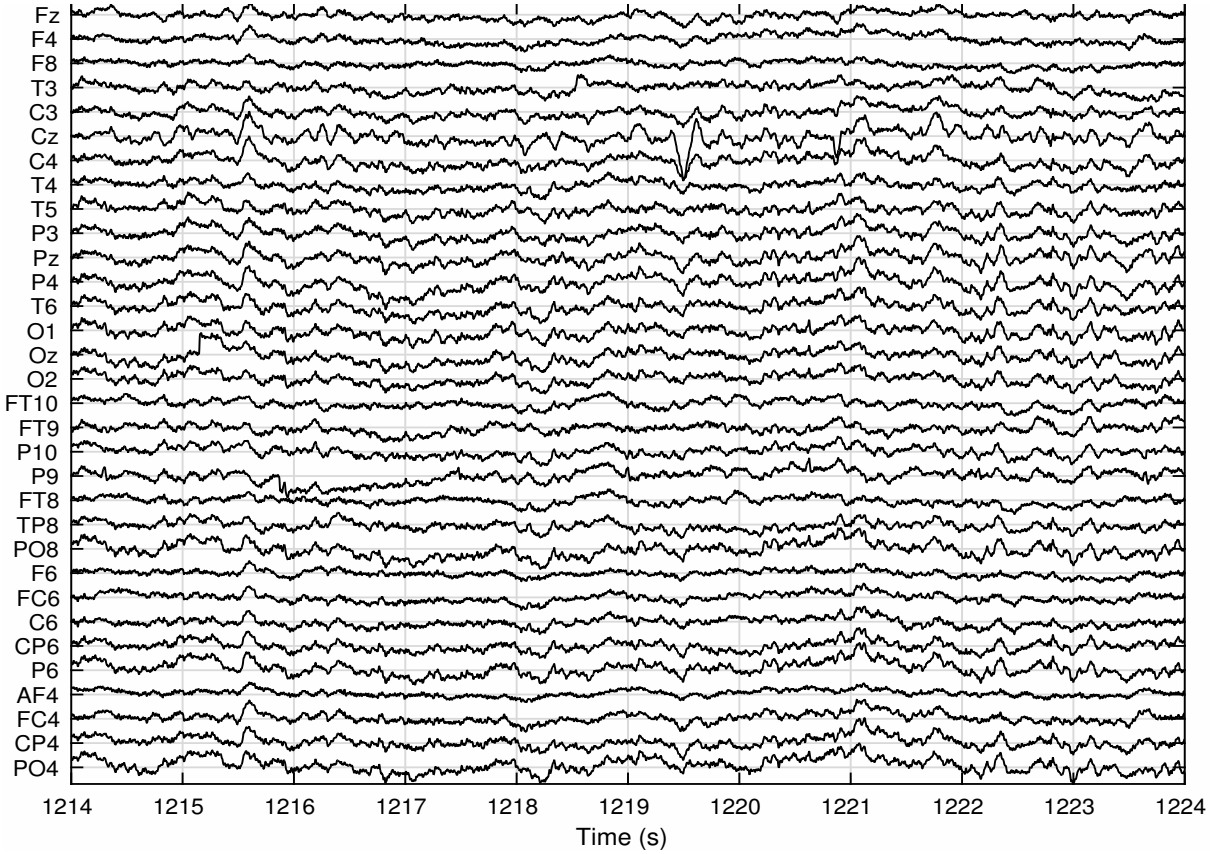

Figure 1.10: Sub-sample of 32 EEG measurements acquired using international 10-20 system of 64 sensors. Both low pass filter and average reference removal were applied on data.

the waves are quasi-stationary with homogeneous amplitudes and frequencies. In EEG, five main rhythms are distinguished, issued from a classification of the brain rhythms driven by pragmatic clinical consideration introduced by the *International Federation of Societies for Electroencephalography and Clinical Neurophysiology* in 1974. The rhythms are classified from lowest to highest frequency as follows: delta (δ), theta (θ), alpha (α), beta (β) and gamma (γ):

1. δ (0,5-4 Hz): associated with deep sleep and probably present in a state of weakness. The δ frequency is very slow and generally have a great amplitude. It appears in young children of age less than one year and in this context constitutes the dominating rhythm.

2. θ (4-8 Hz): appears during the sleep or the periods of time of concentration. Some work located a theta activity, induced by tasks of mental calculation, on the central line of the frontal lobe (89). This type of rhythm can also appear during meditation (66) and during the procedures of storage operation (110). It is frequent in children up to 13 years old but the abundant presence of a theta or asymmetrical rhythm in the conscious adult is abnormal (135).

3. α (8-13 Hz): with an amplitude between 30 and 50 μV appears mainly in the posterior areas (behind the vertex). Its distribution is bilateral and symmetrical and has a sinusoidal morphology; however, in some cases it can be presented in a form of sharp waves (108). The appearance of α rhythm is common when eyes are closed and during the relaxation therapy, it is thus attenuated by the increase in vigilance, with a tendency to disappear at the time of a mental activity and by the opening of the eyes.

4. β (13-30 Hz): has a localization in the mid-sized areas of the two hemispheres in an asynchronous way. Its amplitude is lower than 30 μV and is usually masked by the α rhythm. Beta rhythms are normal for an adult and are associated with the mental activities, such as attention, problem-solving and the comprehension of the outside world. High contents of the β rhythms can be observed in a state of panic.

5. γ (>30 Hz): refers to the frequencies beyond 30 Hz. Its small amplitude and very uncommon presence make it hardly detectable in the surface EEG but it is accessible with intracranial EEG measurements. It could be associated with the synchronization between various cerebral areas implied in the same functional network and thus it might be associated with information processing during the execution of high-level tasks (134).

1.4.1.2 Invasive electroencephalography

Other techniques exist to observe or to improve the observation of the neural activity (see **Figure** 1.11). The most invasive Stereoelectroencephalography (SEEG) (124) is a procedure of recording electroencephalographic signals using electrodes that are surgically implanted into the brain tissue. It is used in epileptic patients that do not respond to medical treatment and thus are potential candidates to receive brain surgery in order to control seizures.

Somehow less invasive is the Electrocorticography (ECoG) (49, 63), or intracranial electroencephalography (iEEG). This type of electrophysiological monitoring uses electrodes placed directly on the exposed surface of the brain in order to record the electrical activity from the cerebral cortex,

thus it risks less brain damages. On the other hand, this technique requires the partial removal of the skull that covers the area of interest, which implies more aggressive surgery for the other head tissues (scalp, bone, ...).

1.4.1.3 Magnetoencephalography

Magnetoencephalography (MEG) is a non-invasive neurophysiological technique that measures the magnetic fields generated by neuronal activity of the brain. The spatial distributions of the magnetic fields are analyzed to localize the sources of the activity within the brain, and the locations of the sources are superimposed on anatomical images, such as MRI, to provide information about both the structure and function of the brain. We will not use these measurement in our work so we will not detail them further (see *e.g.*, (132) for more details).

1.4.2 Functional imaging

Functional MRI or fMRI (13) is a functional neuroimaging procedure that use MRI technology in order to measures the brain activity by detecting changes associated with blood flow. This technique is based on the fact that cerebral blood flow and neuronal activation are both related. In addition to fMRI and EEG, functional and physiological changes within the brain may be registered also by SEEG or MEG. Application of fMRI is, however, very limited in comparison to EEG or MEG for a number of important reasons:

- Time resolution of fMRI image sequences is very low (from 1 second 100 seconds).
- Many types of mental activities, brain disorders, and malfunctions of the brain cannot be registered using fMRI since their effect on the level of oxygenated blood is low.
- The accessibility to fMRI (and currently to MEG) systems is limited and costly.
- The spatial resolution of EEG, however, is limited to the number of recording electrodes (or number of coils for MEG).

Positron emission tomography (PET) (10) and Single photon emission computed tomography (SPECT) (21) both are nuclear medicine imaging techniques which provide metabolic and functional information unlike CT and MRI. This technique produces a three-dimensional image of functional processes in the body and requires the injection of positron-emitting radionuclide (tracer) into the

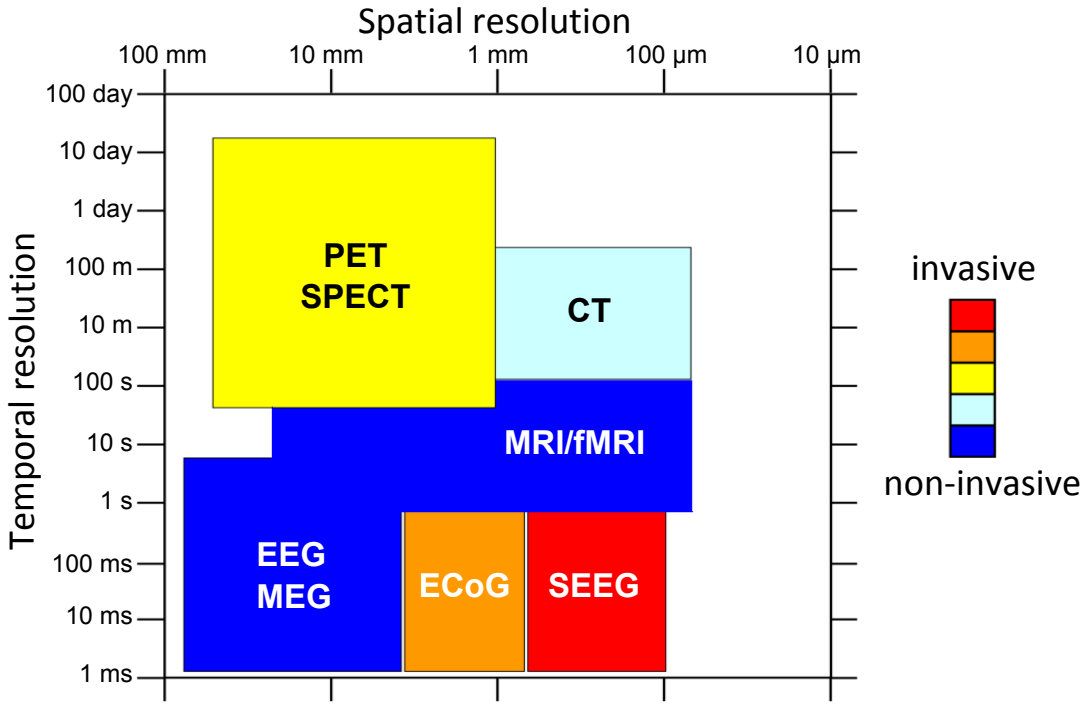

Figure 1.11: Spatial and temporal resolutions of the different brain imaging techniques (PET: Positron Emission Tomography, SPECT: Single-Photon Emission Computed Tomography, CT-scan: Computed Tomography scan, MRI: Magnetic Resonance Imaging, fMRI: functional MRI, EEG: ElectroEncephaloGraphy, MEG: MagnetoEncephaloGraphy, ECoG: ElectroCorticoGraphy, SEEG: Stereo-EEG) (4).

patient in order to detect pairs of gamma rays emitted indirectly by injected tracer.

A global overview of the systems listed above is given in figure 1.11. Nowadays as these technologies become more and more accessible, it is possible to provide a hybrid data recording system together with other imaging modalities, for example, EEG + fMRI. Such combination provides a very forms a powerful tool for the investigation of brain function as shown in (93).

1.5 Applications

1.5.1 Medicine

Both visual and automatic studies of EEG are used in the diagnosis of many cerebral electrophysiological disorders. The durations, amplitudes, forms and frequencies are thus fundamental components of the EEG signal (20). High temporal resolution (milliseconds) allows to observe variations in the

EEG patterns for certain states of the subject that indicate abnormality. Sharbrough (113) divided the nonspecific abnormalities in the EEGs into three main categories:

- widespread intermittent slow wave abnormalities, often in the delta wave range and associated with brain dysfunction;
- bilateral persistent EEG, usually associated with impaired conscious cerebral reactions;
- focal persistent EEG usually associated with focal cerebral disturbance.

The first category, a burst-type signal, is attenuated by alerting the individual and eye opening, and accentuated with eye closure, hyperventilation, or drowsiness. The second category, i.e. bilateral persistent EEG phenomenon is etiologically nonspecific and the mechanisms responsible for their generation are only partially understood. Finally as for the third category, i.e. focal persistent EEG are abnormalities that may be in the form of distortion and disappearance of normal patterns, appearance and increase of abnormal patterns, or disappearance of all patterns. Such changes are seldom seen at the cerebral cortex. With regards to the three categories of abnormal EEGs, their identification and classification requires a dynamic tool for various neurological conditions and any other available information. A precise characterization of the abnormal patterns leads to a clearer insight into some specific pathophysiologic reactions, such as epilepsy, or specific disease processes, such as subacute sclerosing panencephalitis (SSPE) or Creutzfeldt-Jakob disease (CJD) (75).

In addition to the previously mentioned abnormalities it is noteworthy to point out the different fields of medicine that, according to (108), benefit from the EEG analysis:

- monitoring alertness, coma, and brain death;
- locating areas of damage following head injury, stroke, and tumour;
- testing afferent pathways (by evoked potentials);
- monitoring cognitive engagement (alpha rhythm);
- producing biofeedback situations;
- controlling anaesthesia depth (servo anaesthesia);
- investigating epilepsy and locating seizure origin;
- testing epilepsy drug effects;

- assisting in experimental cortical excision of epileptic focus;
- monitoring the brain development;
- testing drugs for convulsive effects;
- investigating sleep disorders and physiology;
- investigating mental disorders;

1.5.2 Brain-computer interface

The simplest way to interact with a computer is by using human-computer interfaces (HCI) such as keyboard and mouse. Nevertheless, such interaction is very difficult for users who are unable to generate necessary muscular movements to use typical HCI devices. Therefore a possible solution is to develop a new interface, called brain-computer interface (BCI), in order to add this new dimension of functionality (131). In fact brain-computer interface is a method of communication based on the neural activity generated by the brain and is independent of its normal output pathways of peripheral nerves and muscles. Therefore the ultimate goal of BCI is to provide a new channel of output for the brain that requires voluntary adaptive control by the user (139).

The neural activity used in BCI can be recorded using invasive (ECoG) or noninvasive (EEG, MEG, fMRI) techniques. In the simplest noninvasive case one might be interested not in high spatial resolution scalp recordings but rather in recordings of a few electrodes that are located over a specific region where underneath local neocortical area corresponds to some specific functions (3, 9, 19, 102, 138).

Most of BCI systems require reliable muscular control such as neck, head, eyes, or other facial muscles. When only neural activity is required, BCI utilizes neural activity generated voluntarily by the user. Interfaces based on involuntary neural activity such as epileptic seizure, utilize many of the same components and principles as BCI, but are not included in this field. BCI systems, therefore, are especially useful for severely disabled, or locked-in, individuals with no reliable muscular control to interact with their surroundings. As detailed in **Figure** 1.12, the interaction with the device using BCI is enabled through a variety of intermediary functional components, control signals, and feedback loops. Intermediary functional components perform specific functions for converting intent into action. By definition, this means that the user and the device are also integral parts of a BCI system. Interaction is also made possible through feedback loops that serve to inform each component in the system of the state of one or more components (131).

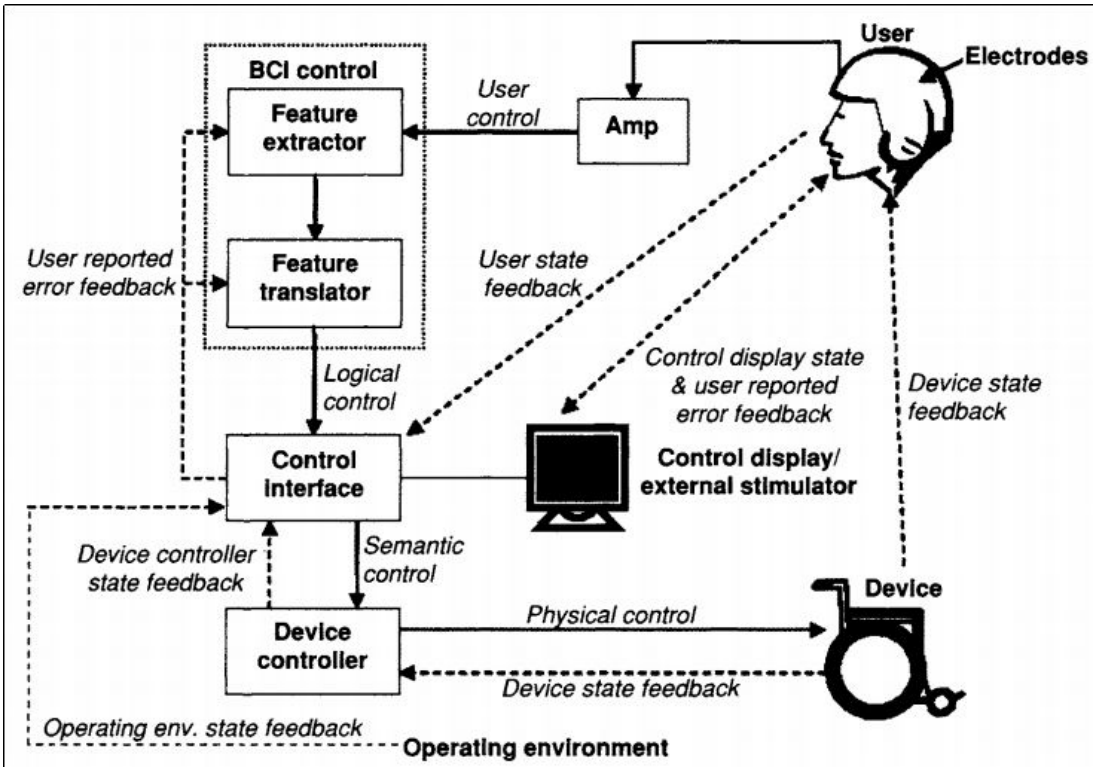

Figure 1.12: Functional components and feedback loops in a brain-computer interface. The users brain activity is measured by the electrodes and then amplified. The feature extractor transforms raw signals into relevant feature vectors which are classified into logical controls by the feature translator. The control interface converts the logical controls into semantic controls that are passed onto the device controller. Finally the device controller changes the semantic controls into physical device-specific commands that are executed by the device. The BCI system, therefore, can convert the user's intent into device action (83, 131).

1.6 Objectives of the thesis

Qualitative analysis of EEG signals gives an insight of underlying neocortical activity. Although the task is not simple due to the noise, smearing effect of skull and, as modelling is involved, model errors. Depending on application one might be interested in different statistical, spatial and temporal signal properties. In the medical context, main interests include time-frequency analysis as well as localization of the neural generators. This requires solving an inverse problem, which often in organic systems are ill-posed due to the uncertainty, noise, lack of spatial measurement resolution (only few measurements are available) and model errors.

In this matter the **first objective** of the thesis is to propose methods with low computational cost

and assuming simple models, thus without detailed anatomical information. On the other hand, we exclude completely blind methods such as blind source separation (BSS), that do not guarantee plausible source estimation neither in terms of time courses (the neural generators might be synchronized) nor in terms of mixing model, *i.e.*, resulting cortical or scalp potenrial map estimation (which is in reality smooth and dipolar). The proposed method should thus provide smooth estimation of the source scalp projections based on simple anatomical assumptions (priors) like electrode 3D locations. We will naturally come close to surface laplacians, which can be seen as methods to estimate the activity of the cortical generators (sources) situated below the measuring electrodes.

The previous framework considers a fixed number of sources (very small comparing to the multiple possible locations on the cortical surface), with fixed positions. In the second part of our work we relaxed these constraints (given number of sources at fixed positions), while still aiming to obtain a small number of generators explaining the measurements and thus the scalp maps. In this context, sparse approximations of the signal are very popular for under-determined problems (*i.e.*, when the number of possible sources is much higher that the number of sensors) where infinite number of solutions exist. Indeed, in some situations (*e.g.*, epilepsy) the sparse nature of both temporal and spatial neural activity must be taken into account. Therefore the **second objective** of the thesis is to impose spatial and temporal sparsity.

In order to achieve the objectives of the thesis one must investigate the available methods and approaches that deal with such problems. In fact, dozens of methods are available to solve under-determined inverse problem where no unique solution exists. Therefore the second chapter of this thesis is dedicated to the state of the art where we show different families of Electrical Source Imaging (ESI) techniques.

Further in the third chapter we tackle the first objective listed above and we propose a new family of methods called dipolar cortical mapping (DCM), aiming to find a balance between ESI methods based on anatomical models and methods without strong anatomical priors, such as surface Laplacians. Like some recent anatomy based spline interpolation surface Laplacians (32), our proposed method uses easily available anatomical information. We go one step further, by using this modality to parametrize a physiologically informed family of interpolating functions. The cortical potential then is estimated under each electrode by inverting a full rank model.

In the fourth chapter, we propose a novel approach for cortical source imaging, based on a an original space-time-frequency dictionary extracted from the data using wavelet techniques and a recent dictionary-based optimisation scheme called Single Best Replacement. This method adopts a

forward-backward strategy and is able to reconsider spurious decisions made in the previous iterations. The main contribution of this chapter resides in the construction of the dictionary, which is made of spatio-temporal atoms built from the fusion of a realistic BEM head model with time-frequency atoms learned from the data using a wavelet denoising approach.

Chapter 2

Brain Source Imaging

In the previous chapter we have introduced the anatomical aspects of neural generators and their modeling as equivalent dipoles. Those generators produce measurable potentials which can be recorded using EEG set-up. The aim of this work is to investigate and propose methods for explaining the EEG measurements using as less as possible anatomical information and/or generators.

In the first part of the chapter, we will focus on the general problem of the estimation of the underlying generators from the EEG recordings. The classical approach passes trough a first important aspect, which is the resolution (more or less precise) of the forward problem. This forward model yields a lead-field matrix explaining the projection of a given set of (dipolar point) sources on the electrodes. We discuss the common methodologies for the construction of such lead-fields, from simple analytical models to more elaborated numerical models based on a discretized patient-dependent model of the head.

We then consider a first family of approaches estimating the dura-potential (cortical potential distribution map) from EEG measurements with weak or absent *priors* on the mixing model, *i.e.*, independently of the resolution of any forward problem. Such methods, known as Surface Laplacians (SL) (see section 2.2), are based on second order derivatives of measured surface potential and depend only on the considered surface geometry. SL acts as a high-pass spatial filter and eliminates much of the volume conduction distortion, improving the spatial resolution and yielding a reference-independent estimate of cortical potentials (25, 79). We will discuss briefly the advantages and drawbacks of both discrete and continuous (based on interpolation), local and global, Laplacian estimates.

A second family of approaches deals with the inversion of a given forward model. As said previously, we aim to explain the measurements using as less variable as possible. When a forward model

is given, this comes to choosing a small number of generators (*i.e.*, a small number of source positions and/or orientations). The equivalent dipole fitting procedure belongs to this class, where only one to few dipoles are assumed to be active. Such approach requires strong assumptions about the number of underlying dipoles, and is based on non-linear optimization techniques that are highly sensitive to model uncertainties and initialization issues. An alternative approach consists in Electrical Source Imaging (ESI) methods, based on distributed source model, where a great number of (fixed-oriented) dipole candidates are covering the whole source space. Such inverse problem is severely ill-posed, the size of the source space being far higher than the number of data channels. We provide a brief overview of the most popular approaches to regularize this problem, before emphasizing on scanning and Matching Pursuit approaches for obtaining sparse solutions.

2.1 Forward modelling of the head medium

The human head is organized in layers, the principal ones we will consider being the scalp, the skull, the Cerebrospinal Fluid (CSF), and finally the brain itself composed of the white and the gray matters. The CSF is often ignored and a further simplification is too consider the brain as an homogeneous medium with no distinction between white and gray matters, leading to the over-simplified model of **Figure** 2.1. Depending on the available anatomical information, different geometries as well as

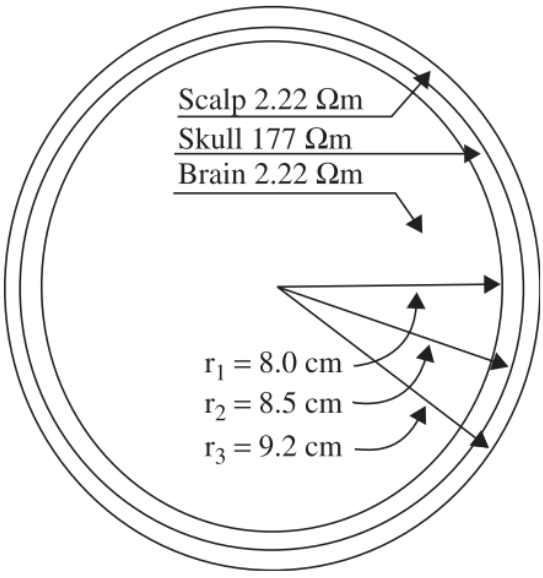

Figure 2.1: The three principal layers of the brain including their approximate resistivities and thicknesses (Ω = ohm) (108)

conductivities can be assumed, starting from Infinite Homogeneous Medium (IHM) up to realistic high resolutions Boundary or Finite Element Models (BEM or FEM), requiring MRI and CT data segmentation. Given one of these models, a so-called forward model can be built. Such model takes the form of a lead-field matrix **A** where each column corresponds to the electrical potential generated by a unit dipole placed at a given location, generally in the gray matter. In this section we give details on the computation of **A** under various hypothesis.

2.1.1 Infinite Homogeneous Medium (IHM)

The simplest model considers the electro-magnetic propagation in an unbounded medium having an homogeneous conductivity σ_{inf}. It is commonly accepted that the frequencies observed on the scalp do not exceed $100Hz$. For such low frequencies, the quasi-static approximation can be assumed, and the time derivatives in Maxwell's equations can be neglected. Under such hypothesis, the potential measured at any location r_b due to a primary current density field $\mathbf{J}_p$ can be expressed as follows (109, 120):

$$\mathbf{V}(\mathbf{r}) = \frac{1}{4\pi\sigma_{inf}} \int_{\mathscr{R}^3} \mathbf{J}_p(\mathbf{r}') \cdot \frac{\mathbf{r}-\mathbf{r}'}{||\mathbf{r}-\mathbf{r}'||^3} d\mathbf{r}' \tag{2.1}$$

where **V** vanishes with the distance. If $\mathbf{J}_p$ is reduced to a single dipole at location $\mathbf{r}_0$ with momentum **q** (see **Figure** 2.2), the potential at **r** due to this dipole writes:

$$\mathbf{V}(\mathbf{r}) = \frac{1}{4\pi\sigma_{inf}} \mathbf{q} \cdot \frac{\mathbf{r}-\mathbf{r}_0}{||\mathbf{r}-\mathbf{r}_0||^3} \tag{2.2}$$

Such model is straightforward to implement with extremely low computational cost. It provides a rough approximations when no anatomical information is available, but is obviously over-simplistic with regards to the anatomical complexity of the head and to its inhomogeneities.

2.1.2 Spherical head models

A first attempt to have a more realistic head approximation was made by Frank in (42), followed later by more efficient computation (*e.g.*, (142)), where a single sphere model for two monopole sources was proposed. Single sphere model can be viewed as an extension of infinite homogeneous model by adding a boundary interface S modeling the presence of the principal inhomogneities, namely the skull. The inner medium is assumed to be homogeneous while the outer space is assumed to be non-conducting.

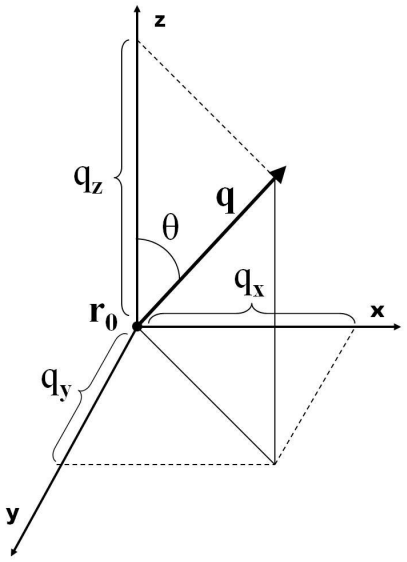

Figure 2.2: Dipole with momentum $\mathbf{q}$ at location $\mathbf{r}_0$

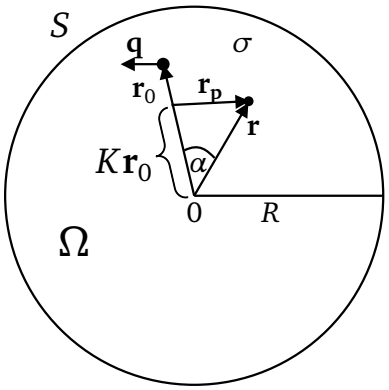

Figure 2.3: Diagram of single sphere model in order to describe the potential at point $\mathbf{r}$. Dipole is located at $\mathbf{r}_0$ with moment $\mathbf{q}$. R corresponds to the radius of spherical volume Ω with external boundary S.

$$V(\mathbf{r}) = \frac{1}{4\pi\sigma}\mathbf{q}\cdot\left\{\frac{\mathbf{r}-\mathbf{r}_0}{||\mathbf{r}-\mathbf{r}_0||^3} + \frac{\mathbf{r}-K\mathbf{r}_0}{\left(R\frac{||\mathbf{r}_p||}{||\mathbf{r}||}\right)^3} + \frac{1}{R^3\frac{||\mathbf{r}_p||}{||\mathbf{r}||}}\left[\mathbf{r} + \frac{\frac{\mathbf{r}_0\cdot\mathbf{r}}{R^2}\mathbf{r}-K\mathbf{r}_0}{\frac{||\mathbf{r}_p||}{||\mathbf{r}||}+1-\mathbf{r}_0\cdot\mathbf{r}}\right]\right\} \tag{2.3}$$

where $K = \frac{||\mathbf{r}||^2}{R^2}$. See **Figure** 2.3 for other variable notations.

If more accurate conductivity information as well as the approximate thickness of skull is available, multi-sphere model, introduced by Rush and Driscoll in (107), can be used. Between the layers, each medium is assumed homogeneous with a given conductivity (121).

Well used and fast approach proposed by Berg in (14) use three concentric spheres where resulting source dipole is approximated as a sum of three individual dipoles of different depths inside one sphere. Although one might increase the number of spheres and use more complicated computation of potentials. As an example we show an N-sphere model (see **Figure** 2.4). Munch (31) demonstrated that, using series of Legendre polynomials, it was possible to compute the potential for arbitrary points inside the outermost sphere. Let $\mathbf{n}_0$ and $\mathbf{n}_r$ be the unit vectors corresponding

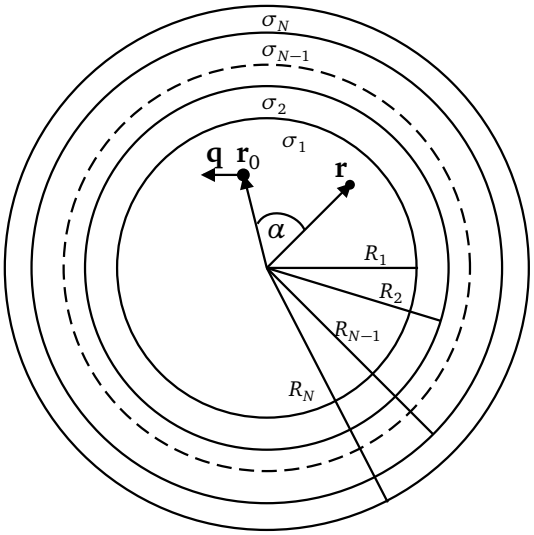

Figure 2.4: Diagram representing the concentric N-layered sphere model (multisphere) with radii $R_1 \ldots R_N$. The model consists of a measurement point $\mathbf{r}$ within a first sphere (*e.g.*, the approximation of the brain boundary) with a dipole at position $\mathbf{r}_0$ and its momentum $\mathbf{q}$.

respectively to the dipole $\mathbf{r}_0$ and the observation point (electrode) $\mathbf{r}$, with α the angle made by these two vectors. The internal potentials for any position $\mathbf{r}$ within the inner medium can be computed as:

$$V(\mathbf{r}) = \frac{1}{4\pi}\mathbf{q} \cdot \{\mathbf{n}_0 (S_1 - \cos\alpha S_0) + \mathbf{n}_r S_0\} \tag{2.4}$$

with

$$S_0 = \frac{1}{||\mathbf{r}_0||} \sum_{j=1}^{\infty} (2j+1) R_j(\mathbf{r}_0, \mathbf{r}) P_j^{'}(\cos\alpha) \tag{2.5}$$

and

$$S_1 = \sum_{j=1}^{\infty} (2j+1) R_j^{'}(\mathbf{r}_0, \mathbf{r}) P_j(\cos\alpha) \tag{2.6}$$

where P_j and $P_j^{'}$ denote respectively the Legendre polynomial and its derivative. $R(.)$ is a function of dipole and electrode positions in the N-sphere head model with different conductivities σ.

2.1.3 Realistic head models

2.1.3.1 Boundary Element Model (BEM)

As for the N-spheres models, boundary element model (BEM) assumes homogeneous medium between two layers, the main difference being that the geometry is no more assumed spherical but is now extracted from imaging modalities, MRI for anatomical tissues and CT for bone structures (**Figure** 2.5).

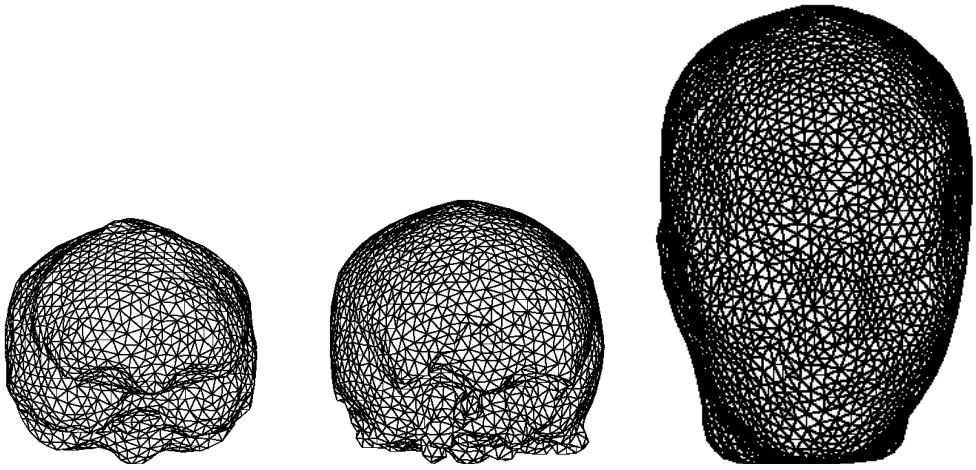

Figure 2.5: Realistic surfaces of inner skull (left), outer skull (middle) and skin (right) used to compute the BEM forward model.

The resolution of such forward problem is numerical. Geselowitz (47) derived a solution in integral form for the realistic piecewise conductor model Ω ($\Omega = \bigcup \Omega_j, j = 1,\ldots,N$) with N interfaces ($S_j, j = 1,\ldots,N$):

$$\sigma(\mathbf{r})V(\mathbf{r}) = V_{inf}(\mathbf{r}) + \sum_{j=1}^{N} \frac{\sigma_j - \sigma_{j+1}}{4\pi} \int_{S_j} V_j(\mathbf{r}') \frac{\mathbf{r}' - \mathbf{r}}{||\mathbf{r}' - \mathbf{r}||^3} \cdot \mathbf{n}(\mathbf{r}') dS_j \tag{2.7}$$

where V_{inf} is the potential in an infinite homogeneous medium with $\sigma_{inf} = 1$ and V_j is the potential on jth surface. Here, $\mathbf{r}$ is every point in Ω but not on any S_j. However, 2.7 cannot be solved because the term on the right implies the integration of the surface potential. But when $\mathbf{r}$ approaches a point on a surface S_k, equation 2.7 can be modified as (109):

$$\frac{\sigma_k + \sigma_{k+1}}{2} V_k(\mathbf{r}) = V_{inf}(\mathbf{r}) + \sum_{j=1}^{N} \frac{\sigma_j - \sigma_{j+1}}{4\pi} \int_{S_j} V_j(\mathbf{r}') \frac{\mathbf{r}' - \mathbf{r}}{||\mathbf{r}' - \mathbf{r}||^3} \cdot \mathbf{n}(\mathbf{r}') dS_j \tag{2.8}$$

where $V_k(\mathbf{r})$ is the potential at $\mathbf{r} \in S_k$. Calculating $V_k(\mathbf{r})$ for each k, we combine 2.8 and 2.7 to get $V(\mathbf{r})$ for $\mathbf{r} \in \Omega$. Unfortunately, for realistic models, 2.8 and thus 2.7 cannot be solved directly (because of the surface integration) and some approximation (discretization) of the surface function needs to be provided for a numerical solution of V. See for example (70) for further details about solving forward problems in the context of EEG.

A widely used method to compute the forward model (lead-field matrix) is the Isolate Problem Approach (IPA) (also called Isolated Skull Approach), proposed by Hamalainen and Sarvas in (62) for 3-layer models. A generalized version of the N-layer model was shown in (84) and tested in (45).

2.1.3.2 Finite Element Model (FEM)

Finite Element Method (FEM) is considered to be the most advanced method for the calculation of the forward problem. Compared to BEM, FEM discretizes the head volume Ω in elementary (volumic) elements (usually at the scale of the voxel) and assigns a conductivity for each of them. In this way, FEM is able to handle realistic geometries including inhomogeneous and anisotropic tissue properties (30, 59, 64). For detailed explanation please see (132) and (70). Such models are difficult

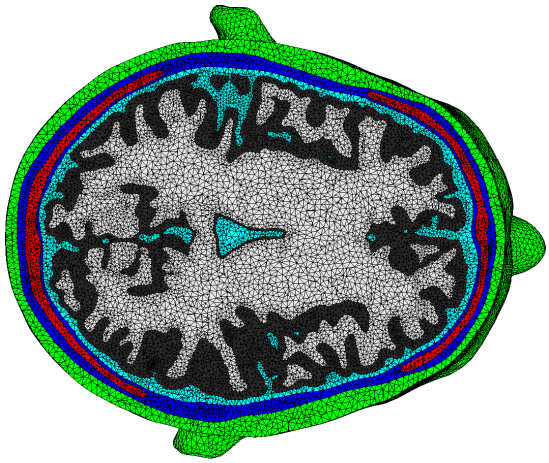

Figure 2.6: Segmented realistic anatomical tissues used to compute the FEM forward model. Image taken from (University of Münster web page). Each color represents different anatomycal tissue with its particular conductivity.

to construct and come with a huge computational burden. As shown in chapter 5 of (70) and in (132), the modeling error between both BEM and FEM is small already when inner anatomical structures in BEM are approximated with one layer, at least when using current approximations

for the FEM parameters (constant scalars conductivities by layer). The error becomes negligible when more layers are introduced, while the computation burden is much lower for the BEM, which highlights its advantage over FEM.

2.2 Surface Laplacians

2.2.1 Principle

Despite the high temporal resolution in milliseconds of EEG recordings, such signals are very difficult to analyze due to several drawbacks or shortcomings. First drawback is related to the distance between sources and sensors, thus the source mixing phenomenon, mainly due to the smearing effect of the skull (its poor conductivity). Second, the quality of EEG depends on the spatial sampling (number of electrodes). Too low number of electrodes may lead to an under-sampling of the scalp surface, and some high spatial frequencies might be missed in the source space. Last (third) but not the least important drawback is that EEG recordings strongly depends on the distortion of reference electrode (40).

Estimation using Surface Laplacians (SL) yields following advantages: they aim to eliminate the mixing due to the smearing effect of the skull acting as a *sharpening* or a high-pass filter. In addition they eliminate the effect of reference electrode. It is noteworthy that SL are able to achieve previously listed advantages without any information about conductivities, thus without forward modeling. The disadvantage is that it only estimates cortical surface sources, but on the other hand these cortical potentials are the main contributors to scalp EEG as they are close enough to be detectable by the surface electrodes. Indeed, it is the distance between the cortical generators and the corresponding surface electrode which determines the depth and "visibility" of the active sources (48, 71, 79, 94). An example of Surface Laplacian is illustrated **Figure** 2.7.

The main idea behind Surface Laplacians is simple. The well known Ohm's law shows a relation between the current density and the applied electric field $\mathbf{E}$ (which is the spatial gradient of the potential V):

$$\mathbf{J} = \sigma \mathbf{E} = -\sigma \nabla V \tag{2.9}$$

with σ the electrical conductivity (being a clue that SL assumes homogeneous and isotropic medium).

In the EEG context, several hypothesis are made when adopting the previous relation. First, it is assumed that, in the brain regions with dense source activities, as it is the case in the cortical layer, the direction of the current depends on the cortical geometry determining the source moment (orientation). As the cortical surface is very close to the inner skull surface, the potentials of sources

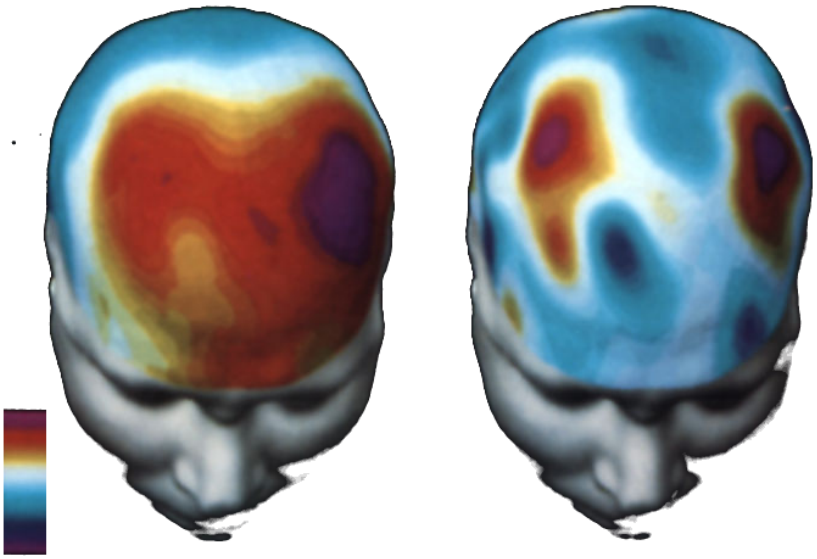

Figure 2.7: Interpolated scalp recordings (left) and estimated cortical potentials (right) (48). Colors represent the potential values (red - positive, blue - negative). Cortical potentials forms sharp sources (red) and sinks (blue) that are greatly blurred due to the smearing effect of the skull. Besides this is the main objective of the SL - to remove the distortion of the skull and estimate the durapotentials.

oriented normal to the skull propagates through the skull into the scalp and spreads tangentially near the scalp boundary due to the air isolation. This leads to idea that different surface regions of the skull behave as skull "sources" and "sinks" as the result of physiological source activities within the brain (79).

Thus, when viewed as a two-dimensional function of space in the local tangent plane to the scalp surface, the scalp current density is seen to diverge from a point. Standard considerations in vector calculus shows that, when applied to a vector function of space, the divergence operator equals zero at most locations, but different from zero at locations where the function is spreading radially in the tangent plane (6, 46). Those "sources" and "sinks" for scalp current on two dimensional scalp surface S can be determined by evaluating the change in current density $\mathbf{J}_S$ starting from equation (2.9). The divergence of current density along the scalp is then equivalent to the surface Laplacian ∇_S^2 of the scalp potential V_S:

$$\nabla_S \cdot \mathbf{J}_S = \nabla_S \cdot \sigma_S \nabla_S V_S = \sigma_S \nabla_S^2 V_S \tag{2.10}$$

where σ_S is the conductivity of the scalp. Note that the gradient operator ∇_S is the derivative along the scalp surface S, expressed in the surface coordinates of 2-dimensional surface, that assumes the

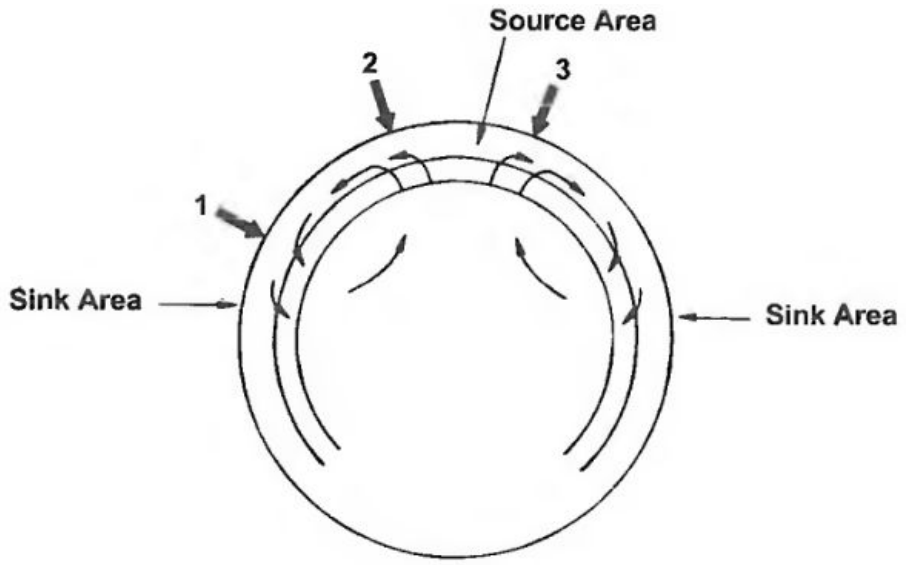

Figure 2.8: Schematic view of cortical dipole layer sources and volume-conducted currents. Scalp "source" is the scalp region into which current is injected by brain current sources and a scalp "sink" as corresponding scalp region where current is flowing back into the skull (79).

local geometry of the scalp.

As explained in (24), the divergence can be also interpreted as a local measure of the difference between how much field (technically, its flux) gets into an infinitesimal volume surrounding the point where the divergence is computed and how much of this field gets out; if the divergence is zero, the same amount of field that gets into the infinitesimal volume also gets out. If the divergence is negative, the amount of field getting in is more than getting out (sink); and if the divergence is positive, more field gets out than comes into the infinitesimal volume (source).

Surface Laplacians (SL) act as a spatial filter. It increases the topographical specificity and filters out spatially broad features (shared among electrodes). It highlights local spatial features that are present in the data but may be difficult to observe when summed with large-amplitude low-spatial bandpass filter. Further we will discuss two different estimates. First type of SL estimates (local and discrete) deal with the raw EEG recordings (operates only with potential values at the position of the electrodes) and the resulting cortical potential is estimated under each electrode. Such estimate is very easy to implement but is dependent on the distances between electrodes and suffers from border effects. Second, more elaborated techniques, global and continuous, are based on a continuous scalp potential map derived from surface interpolation of the electrode potentials. The interpolation can

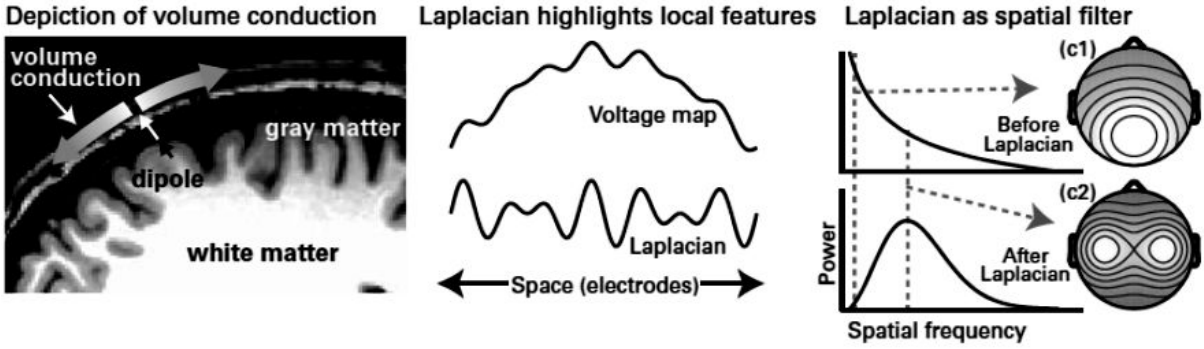

Figure 2.9: Conceptual overview of the motivations for and consequences of the surface Laplacian applied to EEG data (29). On the left is illustrated volume conduction where electrical fields spread tangentially at the boundary between the skull and the scalp. Middle, shows how low-spatial-frequency components in scalp EEG(top) are filtered out in the surface Laplacian (bottom). In the panel on the right using power plots is illustrated the ability of SL to work as a bandpass filter.

be done using either spherical, thin-plate or different splines assuming planar, spherical or realistic geometry. Moreover, these techniques deal better with border electrodes.

2.2.2 Local SL estimates

In the simplest case where 2-D planar surface with spatial coordinates $\{x, y\}$ for any points $\mathbf{r}$ is considered, Hjorth in (68) defined the surface Laplacian operator as:

$$L_{\mathbf{r}} = \nabla^2_{\mathbf{r}}(V_{\mathbf{r}}) = \frac{\partial^2 V_{\mathbf{r}}}{\partial x^2} + \frac{\partial^2 V_{\mathbf{r}}}{\partial y^2} \tag{2.11}$$

In his paper Hjorth showed that the magnitude and the sign of radial current can be determined by means of the Laplace operator as:

$$I_{\mathbf{r}} = -\frac{1}{\xi}\nabla^2_{\mathbf{r}}(V_{\mathbf{r}}) \tag{2.12}$$

where ξ is a constant having the dimension of resistance and being related to the conductivity of the actual medium. The negative sign indicates that the current is assumed to be directed outwards from the interior of the volume. The current may also be represented as a voltage, having a direction to the surface and acting over a resistance of value I.

$$V_{source} = I_{\mathbf{r}}\xi = -\left(\frac{\partial^2}{\partial x^2} + \frac{\partial^2}{\partial y^2}\right)V_{\mathbf{r}} \tag{2.13}$$

Assuming equal distances between scalp electrodes (uniformly distributed along scalp surface projected on plane) in both directions and assigning unity to these distances, the operator simplifies

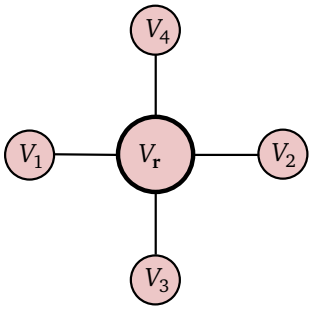

Figure 2.10: Hjorth Laplacian montage. Four neighbouring electrodes located in equal distances from the center electrode.

as the sum of the second order differences in both directions:

$$V_{source} = -(d_x^2 + d_y^2)V_{\mathbf{r}} \tag{2.14}$$

Practically, defining the potential V_0 as the potential at center electrode, and V_1, V_2, V_3 and V_4 the surrounding potentials on the surface (see **Figure** 2.10), these derivatives can be determined as $d_x^2(V_{\mathbf{r}}) = (V_1 - V_0) - (V_3 - V_0)$ and $d_y^2(V_{\mathbf{r}}) = (V_2 - V_0) - (V_4 - V_0)$. The final result yields

$$V_{source} = (V_0 - V_1) - (V_0 - V_3) + (V_0 - V_2) - (V_0 - V_4) \tag{2.15}$$

This SL estimate was first proposed in (68) and later exploited in (46, 125). Hjorth montage is simple nearest-neighbour Laplacian method that estimates directly the SL at selected sites using only the sampled electrical potential values of V, *i.e.*, the potential values at electrodes.

In addition to Hjorth Laplacian estimate, as proposed in (127), calculation of the average gradient for all electrode sites results in a more spatially confined distribution of activity, as it produces the measured spread in potential over the scalp due to lateral current flow. Let V_j, $j = 1, \cdots, n$ be the potential of the n neighbouring electrodes and d_j the distance between the j-th neighbouring electrode and the electrode on which the Laplacian is estimated, the SL is computed on a planar scalp model by:

$$\nabla^2 V \approx V_0 - \frac{\sum_{j=1}^{n} \frac{1}{d_j} V_j}{\sum_{j=1}^{n} \frac{1}{d_j}} \tag{2.16}$$

where V is the potential at the centre electrode. Babiloni in (8) propose to use $n = 10$ in order to take into account 10 neighbouring electrodes.

It is noteworthy that somehow parallel developments were done in neural micro-scale measurements (*i.e.*, for estimating current sources and sinks at the neurone scale, see *e.g.*, (88, 101)). In this

setup, measurements are often done by linearly disposed micro-electrodes, and the so-called current source density (CSD) analysis aims to give access to the current sinks and sources in the extracellular space. These sources and sinks in fact are the local generators of the field potentials, as well as of the action potentials (88). At this microscopic scale, the profiles of field potentials are obtained by measurements at discrete equidistant locations and the current sources (CSD estimates) are simply computed as the second spatial derivative calculated according to a finite difference equation perfectly similar to (2.15), but applied along the electrode axis. It is also interesting to note that more recent developments (77, 78, 101) propose an alternative approach to discrete CSD (strictly equivalent to the surface laplacian applied to the linear case at a microscopic scale), which consists in inverting a forward problem, usually assuming simple forward modeling (infinite homogeneous medium, although more complicated source models). In this thesis we will not focus on the microscopic scale, but we somehow explore the two perspectives described here (laplacian and inverse modeling) in parallel at the macroscopic EEG scale (see chapter 3).

The advantage of local (discrete) SL estimate is its ease of implementation and fast computation. However, this montage do not take into account the complex head geometry. Also, the border effects should be considered, as the border electrode sites lack the neighbourhood information needed for solving the discrete laplacian. The loss of information also increases proportionally with the spatial sampling (7).

In order allow the construction of more precise SL, one might use interpolated surfaces. Further in this chapter we will derive them for spherical geometry, where the expression for the surface Laplacian can be written as derivatives in the corresponding system coordinate(76). In the same manner the surface Laplacian can also be computed for the arbitrary surface geometry, for instance a realistic scalp geometry derived from MRI images as shown in (7, 32) by making use of local surface normals and electrode positions.

2.2.3 Global SL estimate

Nowadays, as high resolution EEG (HR EEG) allows the construction of continuous surface. In such context one might use spline interpolation function to interpolate both surface and potentials, providing the method for global estimate. Such methods depend on two main factors (125): the geometry and the interpolating function. Global SL estimate can be evaluated in two main steps: the first one interpolates the recorded scalp potential values $\mathbf{V}$ using some spline/radial basis functions in order to obtain a continuous function $V(\mathbf{r})$ for all the points on the head surface, while the second one applies a Laplacian operator similar to the one in (2.11), but adapted to the considered geometry. Classical

interpolation solutions vary from spherical splines to thin-plate RBFs, while derivation assumes a given geometry of the head model: spherical (8, 100), ellipsoidal (76) or realistic (7, 32).

2.2.3.1 Spherical head model

Perrin in (100) shows SL estimate using spherical splines on spherical surface. In order to project electrodes from the general head onto a sphere, Perrin uses the properties of the 10-20 system by placing the electrodes using the inter-distance electrodes given by this particular set-up.

If $\mathbf{r}$ is a point over the scalp model surface, $\mathbf{r}_i$ the i-th electrode coordinates on which the potential $v_i \in \mathbf{V}$ is recorded, and N the total number of electrodes, the computation of the spherical spline which interpolates V_i at the coordinate $\mathbf{r}_i$ writes:

$$V(\mathbf{r}) = c_0 + \sum_{i=1}^{N} c_i g(\cos(\mathbf{r}, \mathbf{r}_i)) \tag{2.17}$$

where the c_i is the solution of

$$\begin{cases} (\mathbf{GC} + \mathbf{T}c_0) = \mathbf{V} \\ \mathbf{T}^t\mathbf{C} = 0 \end{cases} \tag{2.18}$$

with c_0 to be defined with:

$$\begin{aligned} \mathbf{T}^t &= [1, 1, \cdots, 1] \\ \mathbf{C}^t &= [c_1, c_2, \cdots, c_n] \\ \mathbf{V}^t &= [V_1, V_2, \cdots, v_n] \end{aligned} \tag{2.19}$$

The ^{t} apex here indicates matrix transposition. The $\mathbf{G}$ array has its (i, j) element defined as

$$g_{ij} = g[\cos(\mathbf{r}_i, \mathbf{r}_j)] \tag{2.20}$$

with $\cos(\mathbf{r}_i, \mathbf{r}_j)$ as the cosine between the electrode positions $\mathbf{r}_i$ and $\mathbf{r}_j$. The $g(.)$ function is defined as follows:

$$g(x) = \frac{1}{4\pi} \sum_{n=1}^{\infty} \frac{2n+1}{n^m(n+1)^m} P_n(x) \tag{2.21}$$

where $P_n(x)$ are the usual Legendre polynomials, and m the spline order (equal to 4 in the original paper (100)).

Finally, to estimate the current density, the classical property showing that the 2-dimensional spherical Laplacian of the Legendre polynomials is a multiple of the same Legendre polynomial turns out to be very useful:

$$\triangle P_n = -(2n+1)P_n \tag{2.22}$$

Then, the expression of the current density at a point $\mathbf{r}$, noted $C(\mathbf{r})$, is proportional to minus the 2-dimensional spherical Laplacian of the potential:

$$C(\mathbf{r}) = \sum_{i=1}^{n} c_i h(\cos(\mathbf{r}, \mathbf{r}_i)) \tag{2.23}$$

where the interpolating function $h(.)$ is obtained with by injecting equation (2.22) into (2.21):

$$h(x) = -\frac{1}{4\pi} \sum_{n=1}^{\infty} \frac{(2n+1)^2}{n^m (n+1)^m} P_n(x) \tag{2.24}$$

More elaborated SL estimates were proposed, for example considering an elliptical geometry for the head (76). This development can be considered as a transition between spherical and realistic SL, with numerical geometry derived from imaging modalities. We will focus next directly on the realistic geometry laplacians, such as proposed by (7, 32).

2.2.3.2 Realistic head model

The realistic Laplacian method developed in (7, 8) is based on the tensorial formulation of the SL on a generic 3-D surface Ω at 3-D points $\mathbf{r}_{x,y,z}$. In a very similar manner as for all global methods, the first step is an interpolation that must be computed for the chosen geometry. As usual, spline functions are used to interpolate the potential values $V(\mathbf{r})$ at any point of the head surface frome the measured values at the electrode positions $V_i = V(\mathbf{r}_i)$. Babiloni in (7) showed that such SL estimate is subject dependent due to the uniqueness of each person head geometry. Later, some improvements were made by He in (65). A new realistic geometry spline Laplacian estimation technique is developed for high-resolution EEG imaging and tested using both a 3-concentric-sphere head model and a realistic head model.

Such formulation allows the calculation of the SL of the potential using a non-orthogonal curvilinear coordinate system on generic surface Ω. Thus $x = u$, $y = v$ and $z = f(u, v)$ is a curvilinear coordinate system on Ω, and $f(u, v)$ a function whose second order partial derivatives exist and are continuous. Then if $f(u, v)$ is a mathematical model of the scalp surface, the SL of the interpolated potential function $V(u, v)$ on this model is defined by:

$$\nabla^2 V(u,v) = \frac{1}{\sqrt{g}} \left(\frac{\partial}{\partial u}(\sqrt{g}) \left(g^{11} \frac{\partial V}{\partial u} + g^{12} \frac{\partial V}{\partial v} \right) \frac{\partial}{\partial v}(\sqrt{g}) \left(g^{21} \frac{\partial V}{\partial u} + g^{22} \frac{\partial V}{\partial v} \right) \right) \tag{2.25}$$

where

$$\begin{aligned} g &= 1+\left(\frac{\partial f}{\partial u}\right)^2+\left(\frac{\partial f}{\partial v}\right)^2 \\ g^{11} &= \frac{1+\left(\frac{\partial f}{\partial u}\right)^2}{g} \\ g^{12} = g^{21} &= \frac{-\frac{\partial f}{\partial u}\frac{\partial f}{\partial v}}{g} \\ g^{22} &= \frac{1+\left(\frac{\partial f}{\partial v}\right)^2}{g} \end{aligned} \tag{2.26}$$

where the continuous potential function $V(u,v)$ is computed with Duchon's 3D splines, also known as thin plate splines (34).

SSL Based on realistic geometry: a numerical approach

Deng in his recent paper (32) proposes a new SL estimation method for realistic scalp geometry which is based on two main steps. First, continuous potential distribution function $V(\mathbf{r})$ is computed from the discrete measurements (EEG electrodes) using a 3-D polyharmonic spline interpolation scheme which, in fact, is the same principle used for spherical spline Laplacian (79). In the second step, the SL operator ∇_S^2 is constructed from the Laplace operator ∇^2 defined on the underlying surface, which takes the form of the trace of the function's Hessian:

$$\nabla^2 V = tr[H(V)] = tr[\nabla\nabla V] \tag{2.27}$$

The operator is restricted to the surface tangent plane by removing the surface normal component from the gradient of the function $V(\mathbf{r})$. At every estimation position $\mathbf{r}$ on the surface, the surface normal projection $n^T n$ is removed, the remaining quantity $(I-n^T n)$ thus gives the projection onto the tangent plane at $\mathbf{r}$. On most surfaces, the quantity $(I-n^T n)$ is also the function of $\mathbf{r}$ and its gradient reflects the impact of local geometry on the estimation of SL. Also to simplify the visualization and source analysis Deng in (32) defines SL to be the negative of the resulting operator:

$$\nabla_S^2 V = -tr[\nabla(I-n^T n)\nabla V] = -tr(\nabla\nabla V)+tr[\nabla(n^T n)\nabla V] \tag{2.28}$$

The second term on the right-hand side may be further expanded as:

$$tr[\nabla(n^T n)\nabla V] = n(\nabla\nabla V)n^T + n[tr(\nabla n)]\nabla V + (\nabla V)^T(\nabla n)n^T \tag{2.29}$$

These three expanded terms capture different degrees of variation of local geometry. The first term uses only the information of the surface normals n. The second term involves the trace of the curvature tensor ∇n, whereas the last term requires the computation of Jacobian matrix of surface normals. If only the diagonal elements of Jacobian matrix are left and all others are set to 0, the operator reduces to a planar approximation of the surface. On surfaces given by a triangular mesh, the unit surface normal n and its Jacobian ∇n must be computed by means of discrete differential geometry (for details see (32)). Such SL estimate is indeed interesting for smooth discrete surfaces (triangulated meshes) and, as this method utilize realistic geometry, is strictly patient dependent. The biggest advantage of this SL estimate is that there is no need to construct a parametric surface, which is a very complicated task.

Till now we briefly discussed a very general family of source imaging modalities that depends only on the geometry of the interpolated surface and estimates the sources under assumption that they are radially oriented to the skull surface. Further we will discuss source imaging techniques that are based on realistic forward models, where some spatial assumptions about sources as well as anatomical structures are made. The use of such models will bring enhanced spatial precision to the inverse problem, in order to localize those neural generators that produce the measured scalp potentials. In the last sections, we will then focus on "economy size" methods, *i.e.*, those which favor a reduced number of active sources.

2.3 Electrical Source Imaging (ESI)

If anatomical information is available, one might construct patient-dependent anatomical models and use ESI methods for the inversion. For the most general models, the dipole orientations are let free and the estimation of both amplitudes and orientations is required. However, since primary sources are widely believed to be restricted to the gray matter, it is possible to significantly reduce the source space to the cortical area from the segmentation of the MR image of the subject. Moreover, the sources are widely believed to be orthogonal to the cortical mantle, thus fixing the orientations of the dipoles and yielding a linear problem where only the amplitudes have to be estimated.

Considering a fixed orientation, one can assume a standard linear forward model where scalp recordings $\mathbf{V}$ can be expressed as a linear combination of dipole amplitudes $\mathbf{S}$ and propagation coefficients or gains $\mathbf{A}$ such that:

$$\mathbf{V} = \mathbf{AS} + \varepsilon \tag{2.30}$$

where $\mathbf{A}$ ($N \times M, N \ll M$) is known as lead-field or gain matrix, and ε denotes the spatio-temporal noise that arises from neural background activity or external artifacts. The number of possible source locations M is much bigger than the number of electrodes N, yielding an underdetermined mixing system that does not have a unique solution. The propagation coefficients embedded in matrix $\mathbf{A}$ depend on the geometry of the head (distances and angles between the cortical surface mesh points, *i.e.*, sources, and electrodes placed on the scalp) and on the electrical properties of the head tissues (skull, skin, ...).

In the following, we will first revise some classical approaches for solving the inverse problem, *i.e.*, estimate $\mathbf{S}$ from eq. (2.30). Since the solution space is far wider than that of the measurements, the problem is ill-posed and constraints need to be imposed to reduce the solution space. The literature for EEG source imaging is very abundant which in fact induced the development huge variety of methods in the last two decades.

We continue with a particular family of methods constraining the sparsity of the solution, *i.e.*, looking for a minimum number of sources explaining the measurements $\mathbf{V}$ (subsection 2.3.1). First we discuss scanning approaches (subsection 2.3.2), known to yield sparser solutions, and we start with the sparsest possible approach, namely the equivalent dipole fitting (subsection 2.3.3). In the following (section 2.3.4), we present an intermediate class of so-called dictionary based methods, the most famous being the matching pursuit (subsection 2.3.4.2). It is this latter type of algorithms that we use and develop in the fourth chapter of this thesis.

2.3.1 Distributed source models

The distributed source model consists in placing dipole candidates on each vertex of a predefined volumetric grid, restricted or not to the gray matter and having, in most of the cases, fixed orientations orthogonal to the cortical surface. The localization of activated brain sources implies the inversion of high-dimensional inverse problem with an infinite number of solutions.

2.3.1.1 Classical MNE

In the absence of noise, a general solution is given by pseudo-inverting $\mathbf{A}$ in equation (2.30):

$$\hat{\mathbf{S}} = \mathbf{A}^{+}\mathbf{V} \tag{2.31}$$

where $\mathbf{A}^{+} = \mathbf{W}^{T}\mathbf{W}\mathbf{A}^{T}(\mathbf{A}\mathbf{W}^{T}\mathbf{W}\mathbf{A}^{T})^{-1}$ is a pseudo-inverse of $\mathbf{A}$. There are an infinity of exact solutions parametrized by the weighting matrix $\mathbf{W}$, and dozens of source estimation methods with different definition of $\mathbf{W}$ can be found in the literature. The simplest solution, yet adapted for superficial

sources such as the cortical ones, is to simply consider the minimum norm solution obtained by taking $\mathbf{W}$ as the identity matrix: $\mathbf{A}^{+} = \mathbf{A}^{T}(\mathbf{A}\mathbf{A}^{T})^{-1}$.

Without weighting the lead-field matrix but in the presence of noise, Stenroos in (119) evaluates the performance of $L2$-norm (MN) estimator (43, 61) which is a standard way to obtain a unique solution:

$$\mathbf{T}_{MNE} = \mathbf{A}^{T}(\mathbf{A}\mathbf{A}^{T} + \lambda\mathbf{C})^{-1} \tag{2.32}$$

where $\mathbf{C}$ is the covariance matrix of the channel noise ε in (2.30). λ is the regularization parameter that sets the balance between reproduction of measured data and suppression of noise (53, 58, 104). If the covariance is not known, one might simplify the equation (2.33) by assuming $\mathbf{C}_N = \mathbf{I}$.

The Weighted Minimum Norm algorithm takes into account the noise and compensates for the tendency of MNEs to favour weak and surface sources, through the introduction of a particular weighting matrix $\mathbf{W}$:

$$\mathbf{T}_{WMN} = \mathbf{W}^{T}\mathbf{W}\mathbf{A}^{T}(\mathbf{A}\mathbf{W}^{T}\mathbf{W}\mathbf{A}^{T} + \lambda\mathbf{C})^{-1} \tag{2.33}$$

$\mathbf{W}$ can take different forms by integrating various *priors*, the simplest one being based on the norm of the columns of $\mathbf{A}$.

2.3.1.2 LORETA

A particular version of the WMN algorithm is called as Low resolution brain electromagnetic tomography (LORETA) (98) which is based on the assumption that the activities of neighboring neuronal sources are correlated and synchronized. The estimation matrix is computed as follows:

$$\mathbf{T}_{LORETA} = \mathbf{W}^{T}\mathbf{L}^{T}\mathbf{L}\mathbf{W}\mathbf{A}^{T}(\mathbf{A}\mathbf{W}^{T}\mathbf{L}^{T}\mathbf{L}\mathbf{W}\mathbf{A}^{T})^{-1} \tag{2.34}$$

The Laplacian operator is implemented in matrix $\mathbf{L}$, favoring smooth spatial distribution of the source amplitudes. Thus the 3D inverse solution corresponds to the "smoothest" current density capable of explaining the measured data. In this manner, LORETA generally provides rather blurred (or "over-smoothed") solutions. Different flavours of LORETA were proposed since (98) (sLORETA, eLORETA), with in principle better localization performances (97).

2.3.1.3 FOCUSS

Much sparser results are provided by FOCal Undeterminded System Solution (FOCUSS), which is a recursive linear estimation procedure, based on a weighted pseudo-inverse solution (52). The weights at each step are derived from the solution of the previous iterative step. Starting from some

initial estimate, the algorithm converges to a source distribution in which the number of parameters required to describe the source currents does not exceed the number of measurements. The algorithm is initialized using a classical weighted MNE pseudo-inverse, using any first initial guess for $\mathbf{W}$ (commonly the identity matrix). $\mathbf{W}$ is then iteratively re-estimated at each step from the covariance matrix of the current estimate $\hat{\mathbf{S}}$, until a given criteria e.g., a given number of iterations or the convergence of $\hat{\mathbf{S}}$. FOCUSS provides solutions that represent compact but somewhat arbitrarily shaped areas of activation in the head. This approach does indeed produce sparse sources, but can be highly unstable with noisy data.

2.3.2 Scanning approaches

Scanning approaches do not try to estimate source activations simultaneously in all possible locations, but they rather scan the solution space and choose the sources that explain best the data. As such, the ill-conditioned pseudo-inversion due to a number of measurements much smaller that the number of possible sources is avoided. Moreover, they can even benefit from further reduction of the source space by some preprocessing, as it will be explained.

2.3.2.1 Pre-processing: Source-space estimation

In order to enforce sparsity, several inversion methods rely on the estimation of the source space (*i.e.*, the minimal number of orthogonal signals necessary to reconstruct $\mathbf{S}$) which is a common problem appearing in noisy linear mixture models. Principal Component Analysis (PCA) is often used to solve this problem: indeed, the first principal components of $\mathbf{V}$ (corresponding to the greatest eigenvalues of the covariance matrix of $\mathbf{V}$) constitute a basis of the signal space and capture the essential structure of the data, allowing the reconstruction of a denoised approximate version of $\mathbf{V}$.

The size of the signal space can be evaluated using simple empirical threshold. For example, we can decide that the number of most significant components (corresponding eigenvalues) from the PCA decomposition corresponds to the number of eigenvalues whose cumulative power (2.35) reaches a given percentage (*e.g.*, 95%) of the data power (2.36).

$$P_c(p) = \frac{\sum_{i=1}^{p} l_i}{\sum_{j=1}^{N} l_j} \tag{2.35}$$

where $l_1 > l_2 > l_p$ are eigenvalues.

$$k = \arg P_c > 0.95 \tag{2.36}$$

The advantage is that this threshold does not have any priors on the source type and spatial/temporal characteristics. Although the drawback of such approach is that the noise level is fixed as the remaining portion of the signal variance, resulting in a wrong estimation of the number of sources. For those methods whose performance highly depends on the correct estimation of the source/noise space this step might be very harmful.

A more elaborated source space estimation is the classical MDL (minimum description length) rule (see for example of classical MDL (28, 106, 137)):

$$MDL(k) = -\log\left(\frac{\prod_{i=k+1}^{p} l_i^{\frac{1}{p-k}}}{\frac{1}{p-k}\sum_{i=k+1}^{p} l_i}\right)^{\frac{p-k}{N}} + \frac{1}{2}k(2p-k)\log N \tag{2.37}$$

where $l_1 > l_2 \cdots > l_p$ are eigenvalues. The number of signals is determined as a value of $k \in \{0, 1, \cdots, p-1\}$ for which the MDL is minimized. MDL is very accurate and stable if the noise can indeed be modelled as white and Gaussian.

2.3.2.2 Beamforming

Beamformer originated from radar and sonar signal processing but later was adapted in a wide range of fields starting from astronomy to biomedical signal processing. The basis of this method is to apply spatial filterings of the data in order to keep only the signals of interest and discard those originated elsewhere (11, 86, 133).

Let $\mathbf{r}_q$ be the location of the dipole that beamformer is monitoring. Assume, as previously, that the orientations of the dipoles are known[1]. The output of the beamformer is the amplitude of the source situated at $\mathbf{r}_q$:

$$s_q(t) = \mathbf{w}_q^T \mathbf{V}$$

where the spatial filter $\mathbf{w}$ is designed to pass with unitary gain the source of interest s_q and to zero sources situated at different locations (and assumed in principle decorrelated with the source of interest) (11). A popular version of beamformer is the Linearly constrained minimum variance (LCMV). The zeroing of the other sources is achieved by simply minimizing the output power of the beamformer subject to a unity gain constraint at the desired location $\mathbf{r}_q$, thus:

$$\min_{\mathbf{w}^T} E[s^2] \text{ subject to } \mathbf{w}^T \mathbf{A}(\mathbf{r}_q) = 1 \tag{2.38}$$

[1]If the orientations of the dipole is not known, one must construct three spatial filters for each of the Cartesian axis $\{\Theta_x, \Theta_y, \Theta_z\}$.

where $\mathbf{A}(\mathbf{r}_q)$ is the column of the lead-field matrix corresponding to the scanned location. Solving (2.38) using method of Lagrange multipliers yields following solution:

$$\mathbf{w} = [\mathbf{A}(\mathbf{r}_q)^T \mathbf{C}_\mathbf{V}^{-1} \mathbf{A}(\mathbf{r}_q)] \mathbf{A}(\mathbf{r}_q)^T \mathbf{C}_\mathbf{V}^{-1}. \tag{2.39}$$

where $\mathbf{C}_\mathbf{V}$ is the covariance matrix of the measurements $E[\mathbf{V}\mathbf{V}^T]$.

Applying this filter to each of the snapshot vectors $\mathbf{V}(t), t = 1, \cdots, T$ in the data matrix $\mathbf{V}$, an estimate of dipole moment for source $\mathbf{r}_q$ is produced. In the same manner, using equation (2.38), such estimates can be computed for all dipole locations $\mathbf{r}_q$.

Although in the context of brain source imaging the performance of LCVM is limited due to the synchronized nature of neural generators. Correlations between sources will result in partial signal cancellation.

2.3.2.3 MUSIC and RAP-MUSIC

The Multiple Signal Classification (MUSIC) is undoubtedly the most popular parametric scanning method. It was initially developed for array signal processing (112), and later adapted for the EEG/MEG source localization (92).

The basis of MUSIC is to scan a single dipole through a grid confined to a three-dimensional (3-D) head or source volume. At each vertex (grid point), the forward model for a dipole at this location is projected on a signal subspace estimated from the E/MEG data. MUSIC starts with covariance estimate of the data thus the scatter matrix $\mathbf{C}_\mathbf{V} = \mathbf{V}\mathbf{V}^T$. The rank k is computed in order to estimate the number of sources (techniques as described in subsection 2.3.2.1 can be used), thus to extract the signal space $\mathbf{V}_S$. Further using forward model $\mathbf{A}$, MUSIC scans for the best location by computing the subspace correlations:

$$\{c_1, c_2, \cdots, c_M\} = \text{sub corr}\{\mathbf{A}, \mathbf{V}_S\} \tag{2.40}$$

where $\mathbf{V}_S$ are the source subspace. $c_i,\ i = 1, \cdots, M$ corresponds to the subspace correlation values (using the subspace correlation sub corr as described in (90)) where the maximum value corresponds to the selected source location (90, 92). MUSIC is based on the assumptions that the data are produced by a set of linearly independent dipolar sources and that the data are corrupted by additive spatially white noise. If two dipoles are synchronized, the initial estimates of the source dimension might be degraded, impacting significantly the results.

A popular extension of MUSIC, The RAP-MUSIC (91) algorithm, overcomes the synchronized-sources problem by recursively building a gain matrix $\mathbf{A}_H$ from the already identified source columns.

After projecting both the source space and the initial gain matrix into the orthogonal complement of $\mathbf{A}_H$, these two residuals are confronted using the usual MUSIC sub-correlation metric, and the next sources is identified (91).

2.3.3 Equivalent Current Dipole

The sparsest possible solution was one of the first attempts to solve the source localization problem in EEG. Scherg in (111) highlights that it is not possible to derive from the scalp potential the activity of each single neuron, or even to separate the activities of different cortical layers. Instead one might expect to separate the activity of some distinct brain areas, leading to decomposed scalp measurement with limited number of sources. This follows the assumption that the brain activity is both focal and sparse. This assumption is at the core of Equivalent Current Dipole (ECD) methods and are known to provide accurate localization in situations of highly focal activations, for example during somatosensory stimulation or epileptic discharges (73, 86).

ECD fits a small given number of dipoles N (usually one or two) on the measurements. For each dipole i, its position $\mathbf{r}_i = \{x, y, z\}$, orientation $\Theta_i = \{\alpha_i, \beta_i\}$, and strength $\mathbf{s}_i$ are to be estimated. The equation 2.30 can be rewritten as:

$$\mathbf{V} = A(\{\mathbf{r}_i, \Theta_i\})\mathbf{S}^T + \varepsilon \tag{2.41}$$

where ε denotes spatio-temporal noise matrix. The goal is to estimate the set $\{\mathbf{r}_i, \Theta_i\}$ and the time-varying amplitudes $\mathbf{S} = \{\mathbf{s}_1 \cdots \mathbf{s}_N\}$ that best describe the data. The common way to solve this fitting problem is to minimize the square distance between the data and the dipole projections:

$$J_{LS}(\{\mathbf{r}_i, \Theta_i\}, \mathbf{S}) = ||\mathbf{V} - A(\{\mathbf{r}_i, \Theta_i\})\mathbf{S}^T||_F^2 \tag{2.42}$$

The estimation of the position of the dipole makes this optimization problem non linear, and can be solved iteratively using constrained gradient descent or constrained optimization techniques.

The main drawbacks of this approach is that it needs a strong *prior* on the number of sources, while the complexity of the problem grows exponentially with this number. Another sensitive issue is the initialization of the algorithm, where multi-start procedure are often applied while not guarantying the algorithm to converge to the global minima. This approach remains popular when one to two strong sources have to be estimated (*e.g.*, for localizing focal epileptic sources (73)), but is not relevant when more sources have to be estimated.

2.3.4 Dictionary based sparse approximation

2.3.4.1 Background

Sparse signal decomposition of $\mathbf{V}_t$ requires finding a limited number of elements from the dictionary $\mathbf{A}$ (*i.e.*, a limited number of columns of the lead-field matrix and thus a limited number of locations) such that their weighted sum best describes the observation data $\mathbf{V}_t$. The popularity of sparse approximation algorithms relies on their ability to provide efficient sparse approximations of a signal for severely under-determined problems (114).

In spatial domain, sparse signal approximation of some arbitrary chosen data vector $\mathbf{V}_t$ (one time instance of multichannel data) can be formulated as the minimization of the penalized least-square cost function:

$$\min_{\mathbf{S}_t} J(\mathbf{S}_t, \lambda) = ||\mathbf{V}_t - \mathbf{A}\mathbf{S}_t||_2^2 + \lambda||\mathbf{S}_t||_0 \tag{2.43}$$

where the l_0 pseudo-norm of the weight column vector $\mathbf{S}_t$, defined as the number of its non-zero entries, is lower than a given number $k \ll M$. In fact by this equation we are trying to find a sparse representation of the data (parametrized by the sparsity *i.e.*, penalty parameter λ) meaning that only a few sources are active at a time. The l_0 norm is a natural measure of sparsity but it leads to NP-complete optimization problem. This means that all possible combinations of the dictionary elements should be considered and yields computationally expensive exhaustive search algorithms.

Due to the complexity of l_0 optimization, some researchers tend to relax the l_0 constraint in order to solve optimization problem under l_p norm with $p \leq 1$ as for example showed in (56). When minimization of l_1 norm is chosen, least absolute shrinkage and selection operator (LASSO) can be used to minimize the residual sum of squares, subject to the sum of the absolute value of the coefficients being less than a (given) constant. Because of the nature of this constraint, it tends to be stable and produce some coefficients that are exactly 0. Therefore LASSO give interpretable models like subset selection as shown and explained in (128). On the other hand, a constraint under l_1 does not guarantee the sparsity as it is in l_0 case. This is an essential aspect especially for sparse localization problems where few as possible sources should explain the data and correspond with some error to the true location of activated cortical region. This is an extremely difficult task especially when dictionary elements are highly correlated as it is for the case of lead-field matrix.

2.3.4.2 Matching Pursuit

Greedy iterative approach such as Matching Pursuit (MP) provide the easiest way to find an approximate solution of the original l_0 pseudo-norm problem by finding g dictionary elements and their

corresponding weighting coefficients, *i.e.*, non zero elements of $\mathbf{S}_t$ in (2.43). The approximation of the observation $\mathbf{V}_t$ found by MP can be written as the following linear expansion (35, 36, 50):

$$\mathbf{V}_t = \sum_{i=1}^{m-1} \langle R^i \mathbf{V}_t, \mathbf{a}_i \rangle \mathbf{a}_i + R^m \mathbf{V}_t \tag{2.44}$$

with $\mathbf{a}_i$ the i-th column of the lead-field matrix $\mathbf{A}$. $R^i\mathbf{V}_t$ denotes the i^{th}-order residual of $\mathbf{V}_t$, and $\langle R^i \mathbf{V}_t, \mathbf{a}_i \rangle$ denotes the inner product determining the weight of the i^{th} atom (in our case - dipole). The MP algorithm is an iterative greedy algorithm that selects at each step the column of $\mathbf{A}$ which shares the highest correlation with the current residuals $\mathbf{r}_m = \mathbf{R}^m \mathbf{V}_t$. This column is then added into the set of selected columns Q, called support. The principle is summed up in the **Algorithm** 1.

Algorithm 1 Matching Pursuit

1: **procedure** MP($\mathbf{A}, \mathbf{V}_t$)
2: Initialize the residual $\mathbf{r}_0 = \mathbf{V}_t$ and initialize the support $Q = \emptyset$. Iteration counter $m = 1$;
3: Find the most correlated dictionary atom $\mathbf{a}$ with index q_n by maximizing following expression: $b_n = \max_q |\mathbf{a}_q^T \mathbf{r}_{m-1}|$ with b_n the weight of the most correlated atom. Update support $Q = Q \cup \{q_n\}$;
4: Update residual $\mathbf{r}_m = \mathbf{r}_{m-1} - b_n \mathbf{a}_{q_n}$. Increase counter $m = m + 1$;
5: If stopping condition is reached, stop MP. Else, go to line 3.
6: **end procedure**

Matching pursuit suffers from the drawback that a particular atom can be picked multiple times. Although MP provides extremely flexible signal representation since the choice of the dictionary is not limited.

2.3.4.3 Orthogonal Matching Pursuit (OMP)

OMP (23, 99, 130) is a popular extension of MP, where at each step all the already extracted weights $\mathbf{b}_m = \{\mathbf{b}_n\}$ are re-estimated by re-projecting the measurements on the linear subspace spanned by the current support Q. The residual is then updated by extracting this projection to the original data $\mathbf{V}_t$. Compared with other alternative methods, a major advantage of the OMP is its simplicity and fast implementation. Note that the residuals after each step in the OMP algorithm are orthogonal to all the selected columns of $\mathbf{a}$, so no column is selected twice and the set of selected columns grows at each step. The general structure of the OMP algorithm is given in the **Algorithm** 2.

This algorithm is a stepwise forward selection algorithm and is easy to implement. A key component of OMP is the stopping rule which depends on the noise structure. In the noiseless case, the

Algorithm 2 Orthogonal Matching Pursuit

1: **procedure** OMP($\mathbf{A}, \mathbf{V}_t$)
2: Initialize the residual $\mathbf{r}_0 = \mathbf{V}_t$ and initialize the support (set of selected variable) $Q = \emptyset$. Iteration counter $m = 1$;
3: Find the most correlating dictionary item $\mathbf{a}$ with index q_n: $\underset{q}{\operatorname{argmax}}|\mathbf{a}_q^T \mathbf{r}_{m-1}|$. Update support $Q = Q \cup \{q_n\}$. Update the current weights $\mathbf{b}_m = \mathbf{A}_Q^+ \mathbf{V}_t$.;
4: Find the most correlating dictionary item $\mathbf{a}$ with index q_n: $\underset{q}{\operatorname{argmax}}|\mathbf{a}_q^T \mathbf{r}_{m-1}|$. Update support $Q = Q \cup \{q_n\}$. Update the current weights $\mathbf{b}_m = \mathbf{A}_Q^+ \mathbf{V}_t$.;
5: Let $P_m = \mathbf{A}_Q(\mathbf{A}_Q^T \mathbf{A}_Q)^{-1}\mathbf{A}_Q^T$ denote the projection onto the linear space spanned by the elements of $\mathbf{A}_Q$. Update residual $\mathbf{r}_m = (I - P_m)\mathbf{V}_t$;
6: If stopping condition is achieved, stop the OMP. If not, go to line 3.
7: **end procedure**

natural stopping rule is when signal $\mathbf{V}_t$ is reconstructed perfectly, thus residual $r_m = 0$ (23, 129, 130). In other case one might estimate the signal and noise power and stop the OMP when only noise is present in residual.

2.3.4.4 Orthogonal Least Squares

A more effective and also more computationally expensive method is Orthogonal Least Squares (OLS). In each iteration step, a least squares problem is solved instead of simple product calculation as it is in the standard MP case. Basically, the orthogonal algorithm was developed as an approach to combine parameter estimation and model structure detections. The principal idea of the algorithm is to decouple the candidate terms by introducing an orthogonal transform so that selected terms will not be affected when a new term is introduced. For most system representations, the orthogonal decomposition approach of the regressor matrix avoids possible ill-conditioning and presents more accurate results. The forward OLS algorithm is based on classical Gram-Schmidt method (141).

When applied on sparse signal representation, the general structure of OLS is the same as that of OMP. The difference is that at each iteration, OLS solves a large number of least-square problems ($M-k$, where k is the size of the current active set), while OMP only performs the $M-k$ inner products between the current residual and each of the remaining candidate columns $\mathbf{a}_n$. The OLS procedure involves two steps, the first involves finding the most correlated atom from the dictionary, and the second involves a dictionary decorrelation step where the atoms that were not selected are decorrelated from previously chosen atoms (27, 114). One of the simplest version of OLS (**Algorithm** 3) is

shown by Blumensath and Kaur (18, 72) where at each step the chosen atom is the one minimizing the most the residual norm. Such algorithm is very easy to implement but the computational burden is significantly increased for large dictionaries.

Algorithm 3 Orthogonal Least Squares

1: **procedure** $\text{OLS}_1(\mathbf{A}, \mathbf{V}_t)$
2: Counter $m = 1$, residual $\mathbf{r}_0 = \mathbf{V}_t$, reconstructed data $\hat{\mathbf{y}}_0 = 0$, dictionary index set $Q_0 = \emptyset$
3: $q_{min} = \underset{q, Q_m^q = Q_{m-1} \cup q}{\arg\min} \; ||\mathbf{V}_t - \mathbf{A}_{Q_m^q} \mathbf{A}^+_{Q_m^q} \mathbf{V}_t||$
4: $Q_m = Q_{m-1} \cup q_{min}$
5: $\hat{\mathbf{y}}_m = \mathbf{A}_{Q_i} \mathbf{A}^+_{Q_i} \mathbf{V}_t$
6: $\mathbf{r}_m = \mathbf{V}_t - \hat{\mathbf{y}}_m$
7: If stopping condition is achieved, stop the OMP. If not, go to line 3.
8: **end procedure**

Another version of OLS has been developed by Gowreesunker (55). As done in the classical MP algorithms, the atom chosen at each step is the one maximizing its inner product with the residual. The current dictionary is then projected in the orthogonal space with respect to this atom, thus its contribution is suppressed from the updated dictionary. Faster implementation can be reached based on QR factorization (27) or modified Gram-Schmidt procedure (51). Nevertheless, for highly correlated dictionaries OLS together with OMP does not guarantee to find an optimal solution (114).

2.3.4.5 Forward-Backward extensions

An improved way to solve the equation (2.43) is to use forward-backward greedy algorithms. The advantage of these approaches is their ability to eliminate the errors made in previous iterations. An example of such approach appears in (143), where a forward-backward OMP extension is proposed to identify basis functions with non-zero coefficients and reconstruct the target function from noisy observations. However, this approach is efficient only if the basis functions are nearly or completely orthogonal, whereas in our case the data are noisy and dictionary elements may be highly correlated.

Further in this chapter we explain two other forward-backward optimization schemes which proved to be very robust and accurate for correlated dictionary elements and noisy measurements.

Sparse approximation using SDMP

A rather specific algorithm was developed for EEG applications, as in our case. The Source Deflation Matching Pursuit (SDMP) algorithm, as presented in (140), is based on the observation that

estimating the contribution of a given source is much easier when the contributions of all the other sources have been eliminated. The method start by initializing a set of eligible source positions using a classical MP or OMP algorithm. From this initialization, each of the selected source positions p in Q are iteratively reconsidered, and possibly taken out from Q if another source position within the set of unselected elements yields a higher decrease of the residual. This is done by suppressing from both the data and the lead-field the contributions of the atom in Q, at the exception of the current re-evaluated position p. An overview of the SDMP is given as the **Algorithm** 4, where we define the matrix projector and its orthogonal version as:

$$\mathbf{P}_{\mathbf{A}} = \mathbf{A}[\mathbf{A}^T\mathbf{A}]^{-1}\mathbf{A}^T \tag{2.45}$$

$$\mathbf{P}_{\mathbf{A}}^{\perp} = \mathbf{I} - \mathbf{P}_{\mathbf{A}} \tag{2.46}$$

Algorithm 4 SDMP

1: **procedure** SDMP($\mathbf{A}, \mathbf{V}_t, Q_{init}$)
2: Initialize $Q = Q_{init}$. Let N_s be the cardinality of Q_{init}.
3: **for** $p = 1$ to N_s **do**
4: $\mathbf{A}_{Q\setminus p} = [\mathbf{a}_{Q_1} \cdots \mathbf{a}_{Q_{p-1}} \mathbf{a}_{Q_{p+1}} \cdots \mathbf{a}_{Q_{N_s}}]$
5: $\mathbf{a}_{Q,n}^{\setminus p} = \mathbf{P}^{\perp}_{\mathbf{A}_{Q\setminus p}} \mathbf{a}_n$
6: $\mathbf{V}^{\setminus p} = \mathbf{P}^{\perp}_{\mathbf{A}_{Q\setminus p}} \mathbf{V}$
7: $q_{Q\setminus p} = \underset{q_n}{\operatorname{argmax}} ||\mathbf{P}_{\mathbf{a}_{Q,n}^{\setminus p}} \mathbf{V}^{\setminus p}||_F^2$, for $n \in \{1, \cdots, M\} \setminus Q$
8: $Q = \{q_1, \cdots, q_{p-1}, q_{Q\setminus p}, q_{p+1}, \cdots, q_{N_s}\}$
9: **end for**
10: If stopping condition is achieved, stop the SDMP. If not, go to line 3.
11: **end procedure**

Wu *et al.* (140) propose a further refinement of the algorithm by reconsidering the orientation of the dipoles during the optimization procedure. It consists in replacing the selection of the source index (line 6 of the **Algorithm** 4) by the maximization of a MUSIC criterion. This version is called the SDMUSIC (Source Deflated MUSIC) algorithm. In this thesis we only consider fixed orientation of the dipoles orthogonal to the cortical surface, and we do not face this dipole orientation/moment estimation problem.

Approximation using SBR

A more classical forward-backward scheme was recently proposed by (114). The Single Best Replacement (SBR) algorithm is able to deal with correlated dictionary elements and is rather robust

to noise. SBR is an Ordinary Least Squares (OLS) forward-backward extension based on successive updates of the sparse signal support (dictionary element indices) by one element: at each step, the support Q is updated either by inserting a new element or removing an existing element. The forward-backward rule shown in equation (2.47) ensures that only the best columns of $\mathbf{A}$ weighted by $\mathbf{S}_t$ are chosen.

$$Q \bullet i = \begin{cases} Q \cup \{i\} & \text{if} \quad i \notin Q \\ Q \setminus \{i\} & \text{otherwise} \end{cases} \tag{2.47}$$

This leads to the construction of an *active set* $\mathbf{A}_Q$, where Q contains the selected column indexes (active source locations). Basically SBR is designed to solve discrete NP-complete problem and, in fact, is a deterministic descent algorithm that minimizes J from (2.43) with a fixed parameter λ. At each step, the support Q is updated (insert "$\cup$" a new element with index i inside the support or remove "$\setminus$" an existing support element) (114, 115). The forward-backward rule shown in equation (2.47) ensures that only the best columns of $\mathbf{A}$ weighted by $\mathbf{S}_t$ are chosen.

$$l \in \arg\min_{i \in \{1,\ldots,n\}} J_{Q \bullet i}(\mathbf{S}_t, \lambda) \tag{2.48}$$

Then if $J_{Q \bullet l}(\lambda) < J_Q(\lambda)$, the subset Q is updated with the new element $Q = Q \bullet l$. Finally the SBR stops when no replacement decreases the cost function or some predefined stopping condition is met, e.g. the residual is significantly small or the maximum size of subset is reached. If $\lambda > 0$, SBR stops after a finite number of iterations. The summary of SBR in pseudo-code format is provided in **Algorithm 5**. For more detailed information see (114) and (115).

Algorithm 5 Single Best Replacement

```
1:  procedure SBR(A, V_t, λ, Q_init)
2:      Initialize Q = Q_init
3:      STOP = FALSE
4:      do
5:          Compute l from equation (2.48) using equation (2.47)
6:          if J_{Q•i} < J_Q then
7:              Q = Q • i
8:          else
9:              STOP = TRUE
10:         end if
11:     while STOP ~= TRUE
12: end procedure
```

2.4 Conclusions

We have seen that when no or few anatomical information are available, an image of the cortex can still be obtain by applying SL methods. SL eliminates much of the volume conduction distortion and yields to a reference-independent estimate of cortical potentials, and thus can be interpreted as a general form of brain imaging modality. We explore similar cortical source estimator in the Chapter 3, and we emphasize how such interpolation scheme can be linked to basic MNE solution.

To improve the estimation and extract more valuable information from the EEG data, one might consider more elaborated head model such as BEM or FEM and use regularized optimization schemes to solve the inverse problem. Different inverse solvers exists that are able to find some compromise using given head model and measured data by performing data fitting on the some chosen subspace of dipoles. The sparsity constraint is of great interest due to spatially and temporally sparse nature of the cortical activity, such approach will be further explored in the Chapter 4 based on the forward-backward MP schemes presented in this chapter.

Chapter 3

Dipolar Cortical Mapping

Most of the recent developments for brain source localization have been focused on the inversion of sophisticated forward model, requiring numerous and precise information (*e.g.*, segmented imaging modalities, medium conductivities, *etc.*,), and yielding more and more complex methodologies as well as computational cost. The motivation of this chapter is to reconsider the problem of cortical source imaging (a restricted but less controversial source localization problem) using as less information as possible in addition to the electrical activities provided through the EEG scalp measurements. Our developments have been focused on methods that rely on basic but realistic geometrical and physiological considerations.

Such philosophy inevitably makes reference to the origin of the discipline and to the Hjorth's Laplacian montage, providing rough estimates of the underlying scalp activities and relying only on physical properties of the electrical current propagation through the skull. This methodology is at the root of a large family of interpolation-based Surface Laplacian (SL) methods, rooted on the assumption that the scalp map is made of a linear mixing of smooth basis functions produced by the underlying sources. Another way of estimating such potentials are provided by the classical model of dipolar sources linearly projected on the scalp map using a lead-field matrix (projection coefficients or gain computed by a forward model). Such Electrical Source Imaging (ESI) approaches based on regularized minimum-norm estimates has also proven to provide reliable estimates of the cortical activity. While both of these families of approach constitute two well separated pieces of an abundant bibliography on this subject (7, 11, 25, 32, 54, 86), they share high similarities not yet clearly pointed out by the current literature. In this chapter, we propose basic cortical imaging methodologies inspired by both of these two families, and we take this opportunity to emphasize the strong links between them.

3.1 Dipolar interpolating functions and DCM

The aim of this chapter is to propose a family of methods able to estimate the cortical sources while integrating as less as possible plausible physiological constraints. The basic idea is to reconstruct the scalp EEG measurements as a sum of spatially smooth functions. In this sense, our method is close to the family of Surface Laplacian (SL) methods. Unlike SL, we do not propose to choose, somehow arbitrarily, an interpolating function of the potentials recorded on the scalp surface and to derive it twice, but rather to choose a physiologically founded approximation of the interpolation. In other words, we want to write the potentials on the surface as a sum:

$$v(\mathbf{r}) = \sum_{k=1}^{M} s_k h(\mathbf{r}, \theta) \tag{3.1}$$

where $v(\mathbf{r})$ is the potential at position $\mathbf{r}$, $h(\mathbf{r}, \theta)$ is the interpolating function depending on some parameters θ, and s_k are the weights.

First assumption we make about the underlaying brain sources that produce the potentials measured using EEG. They are assumed to be dipolar, placed on the cortical surface, orthogonal to the skull surface. This assumption allows us to use a particular family of functions describing the potentials on the head surface, having different parameters. Because of the restrictions stated above (orthogonality to the skull, placement on the cortical mantel), the remaining degrees of freedom (an thus parameters of the interpolating functions) are their positions on the cortex and their amplitudes. In the following, we derive two approximations of the head geometry, yielding two different parametrized functions describing the projection of the dipoles on the scalp.

A very important aspect of interpolation problem is the number of the terms M in the interpolation sum (3.1) called also as a spatial resolution. In this chapter, we assume, as for SL, that M is equal to the number of electrodes. With such methodology in mind, we discuss the analogy with SL solutions and ESI approaches, emphasizing the links between these two well-known but apparently disconnected methodologies.

3.1.1 The dipolar projection

Let's s_k be the amplitude of a dipole k, placed in the superficial cortical layer and normal to the surface of the skull. Following basic electromagnetic propagation rule in an homogeneous medium, we assume that the potential generated by this dipole decreases with the squared of the distance, and is proportional to the cosine of the angle formed by the dipole orientation and the dipole to measuring point direction.

Let's consider an electrode e_j on the head surface, as illustrated on **Figure** 3.1. The potential generated by the dipole k of amplitude s_k on the electrode e_j then writes:

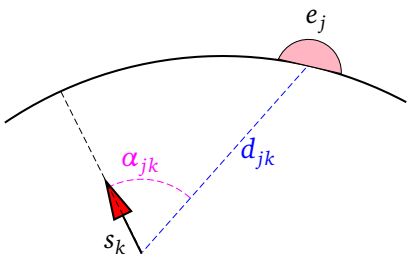

Figure 3.1: Geometrical approximation of the dipole-electrodes configuration. The potential recorded at electrode e_j is produced by dipole with index k and its corresponding amplitude s_k.

$$v_{jk} = \frac{s_k \cos \alpha_{jk}}{C {d_{jk}}^2} \tag{3.2}$$

where α_{jk} is the angle between the direction of the dipole k and the direction from the origin of the dipole to the electrode e_j, and d_{jk} the distance between the position of the dipole k and the electrode j. C corresponds to some proportionality constant linked to the electromagnetic conductivity of the head volume. In this chapter, we will focus on the estimation of the cortical map morphology and ignore the amplitude information, thus we will simply discard the influence of C by setting $C = 1$. Once correct tissue conductivity information is estimated, one might tune C to provide an estimation of the amplitudes.

Considering two simple approximations of the scalp surface geometry, planar and spherical, we derive from 3.2 two different radial basis functions (RBFs) that we use to interpolate the measurements. In this way we impose the scalp map to be reconstructed as the sum of smooth and dipolar projections, thus calling it a Dipolar Cortical Mapping (DCM) of the scalp.

3.1.2 Planar approximation

The simplest geometrical approximation is the planar case, proposed in (74). The scalp surface is assumed to be a plane from the point of view of the dipole k, and the cortical surface is assumed to be parallel to this plan. Thus both planes are parallel to each other and orthogonal to the direction of the dipole (see **Figure** 3.2). In this model we assume the presence of an electrode e_k on the scalp surface above the dipole, with d_{kk} the depth of the dipole. The potential on this electrode due to the

dipole k then writes:

$$v_{kk} = \frac{s_k}{d_{kk}^2} \tag{3.3}$$

Given an electrode e_j on this planar scalp surface, within distance x_{jk} from the electrode e_k, the

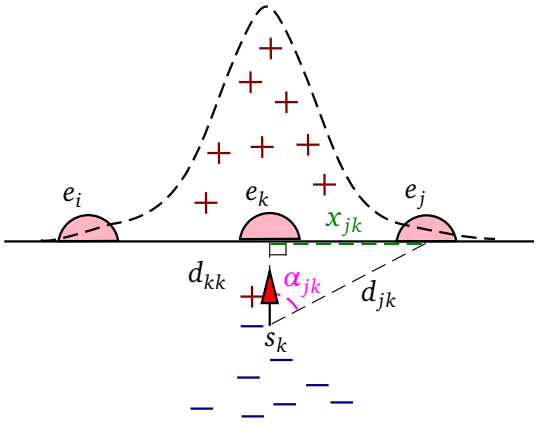

Figure 3.2: Planar geometrical representation of scalp electrical potential distribution (dashed line). Both + and − denotes the positive and negative electrical potential.

equation 3.2 reads:

$$v(x_{jk}) = s_k \frac{d_{kk}}{(x_{jk}^2 + d_{kk}^2)^{\frac{3}{2}}} = s_k \frac{\frac{1}{d_{kk}^2}}{\left(\frac{x_{jk}^2}{d_{kk}^2} + 1\right)^{\frac{3}{2}}} \tag{3.4}$$

In other words, the potential $v(x)$ for given depth of the dipole d_{kk} and its amplitude s_k, at any point on the plane can be expressed using only the euclidean distance x from this point to the electrode e_k:

$$v(x) = s_k h_p(x)$$

$$h_p(x) = \frac{\frac{1}{d_{kk}^2}}{\left(\frac{x^2}{d_{kk}^2} + 1\right)^{\frac{3}{2}}}$$

$h_p(.)$ is a RBF parametrized by the depth of the dipole d_{kk}. Several shapes of this function are given **Figure** 3.4, with various depth parameters. Those distribution functions are smooth, peaky when the dipole is close to the head surface and more flat when it is deeper.

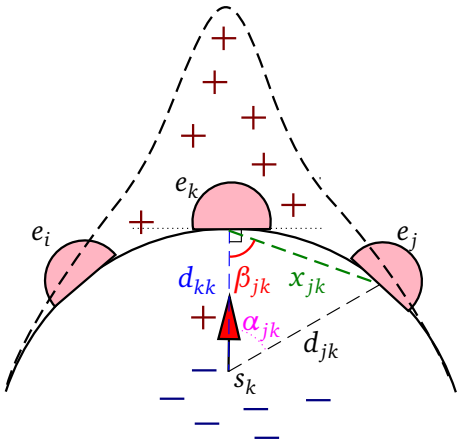

Figure 3.3: Spherical geometrical representation of scalp electrical potential distribution (dashed line). Both + and - denotes the positive and negative electrical potential.

3.1.3 Spherical approximation

A more elaborated approximation of the head surface is to model the head as a sphere, thus placing the electrodes on a spherical surface as it can be seen in **Figure** 3.3. The underlying cortical surface is also assumed to be a concentric sphere with smaller radius, and the dipole k is still pointing to the electrode e_k, perpendicularly to the scalp surface. The distribution function is computed by the same rule as in **equation** (3.2), now taking into account this spherical geometry. From simple trigonometric law, we can identify the following relations in the triangle formed by e_k, e_j and the dipole position:

$$d_{jk}^2 = d_{kk}^2 + x_{jk}^2 - 2d_{kk}x_{jk}\cos(\beta_{jk}) \tag{3.5}$$

$$x_{jk}^2 = d_{kk}^2 + d_{jk}^2 - 2d_{kk}d_{jk}\cos(\alpha_{jk}) \tag{3.6}$$

with β_{jk} the angle between x_{jk} and d_{kk}. Identifying the isosceles triangle formed by e_k, e_j and the center of the sphere, it comes that $\cos(\beta_{jk}) = \frac{x_{jk}}{2r}$. Thus using **equation** (3.6), the distance d_{jk} can be expressed as a function of the depth of the dipole d_{kk}, the inter-electrode distance x_{jk}, and the radius of the sphere r:

$$d_{jk} = \sqrt{d_{kk}^2 + x_{jk}^2(1 - \frac{d_{kk}}{r})}$$

From this expression and the second trigonometric rule above (**equation** (3.6)), we get the following expression for $\cos(\alpha_{jk})$:

$$\cos(\alpha_{jk}) = \frac{2rd_{kk} - x_{jk}^2}{2r\sqrt{d_{kk}^2 + x_{jk}^2(1 - \frac{d_{kk}}{r})}}$$

Using these two last expressions within **equation** (3.2) yields to the spherical DCM_S function, parametrized by the depth of the dipole and the radius of the sphere:

$$v(x_{jk}) = s_k \frac{2rd_{kk} - x_{jk}^2}{2r(d_{kk}^2 + x_{jk}^2(1 - \frac{d_{kk}}{r}))^{\frac{3}{2}}} \tag{3.7}$$

As for the planar approximation, we can express the potential due to the dipole k at any point on the surface given its distance x with the electrode e_k, using following radial basis function (RBF):

$$h_s(x) = \frac{2rd_{kk} - x^2}{2r(d_{kk}^2 + x^2(1 - \frac{d_{kk}}{r}))^{\frac{3}{2}}}$$

parametrized by the depth of the dipole and the radius of the sphere.

As shown in **Figure** 3.4, each approximation gives a different potential distribution function and, thus, a different surface pattern. h_s appears to provide more dipolar distribution which is assumed to be more realistic and thus better performances are expected with regard to the planar approximation. As can be observed on **Figure** 3.4, the potential distribution differs with the depth of the dipole. In fact, as closer the dipoles are placed to the cortical surface, as smaller impact on the neighbouring electrode sites. Deeper placed dipoles shows more flat distribution, and therefore affects more electrodes. As shown by the residual error between both RBFs (**Figure** 3.4c), the difference between both potential distributions increases with the depth of the dipole.

3.1.4 Multiple dipoles case

Up to now, we have dealt with the potentials generated by a unique dipole of amplitude s_k below the sensor k. Assuming that in the same manner as SL, we aim to estimate the cortical activity below each scalp electrode, therefore we must consider one dipole per electrode.

Let M be the number of dipoles and electrodes. Under the same hypothesis on the depth and the orientation, the potential at a given electrode e_j will write as the sum of the potentials generated by the $k = 1..M$ dipoles, which writes as a sum of weighted basis functions $h(x)$:

$$v_j = \sum_{k=1}^{M} v(x_{jk}) = \sum_{k=1}^{M} h(x_{jk}) s_k \tag{3.8}$$

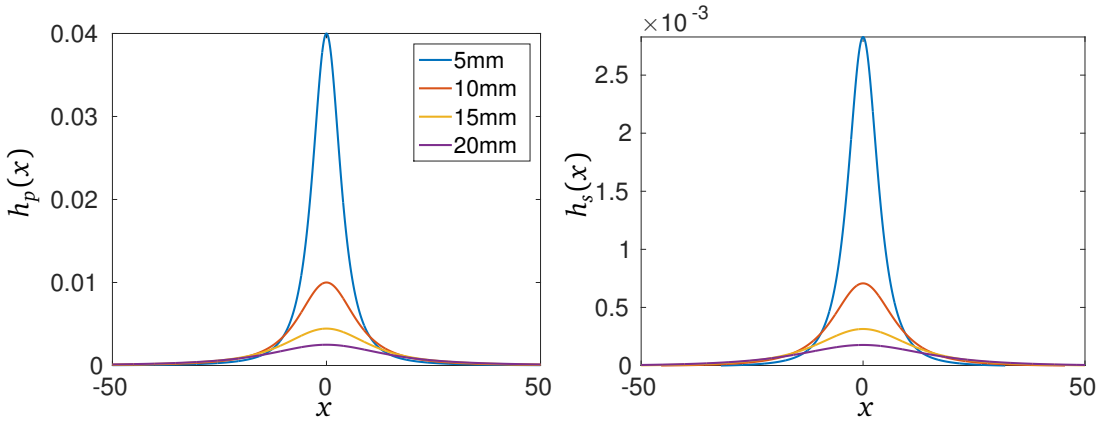

(a) Planar approximation **(b)** Spherical approximation

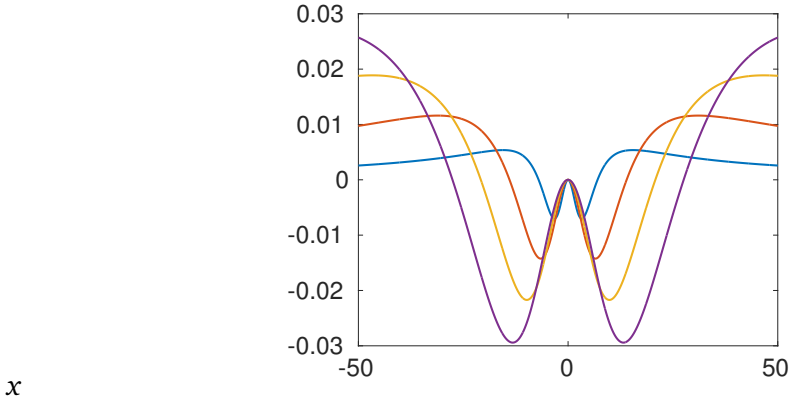

(c) ERROR computed as: $\frac{h_p}{\max|h_p|} - \frac{h_s}{\max|h_s|}$

Figure 3.4: Potential variation on the scalp as a function of the distance x to the electrode pointed e_k by the dipole k and for four different dipole depths d_{kk} computed using planar **(a)** and spherical **(b)** approximations. Finally residual errors **(c)** are given for each depth.

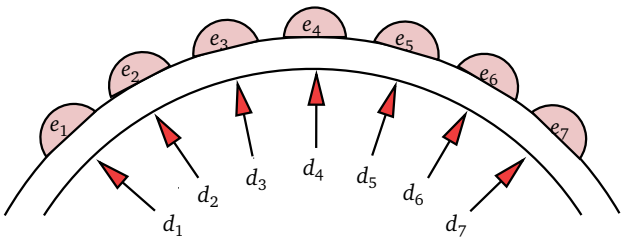

Figure 3.5: Placement of dipoles with respect to the sensor locations. All dipoles are below the sensors at a given depth, and radial to the surface.

When considering all electrodes, (3.8) can be written in matrix form as:

$$\mathbf{v} = \mathbf{H}\mathbf{s} \tag{3.9}$$

where $\mathbf{v}$ is the measured EEG data, the column k of the matrix $\mathbf{H}$ contains the projection coefficients of the dipole k as evaluated by the RBF corresponding to a planar ($h_p(.)$) or spherical ($h_s(.)$) approximation of the head geometry, and the vector $\mathbf{s}$ contains the weights of these different interpolating functions, proportional to the amplitudes of the dipoles we want to estimate. Estimating the cortical potentials corresponds then to the weights vector $\mathbf{s}$ estimation and is obtained by simple full-rank matrix inversion:

$$\hat{\mathbf{s}} = \mathbf{H}^{-1}\mathbf{v} \tag{3.10}$$

Such inversion provides an interpolation of the scalp map using parametrized shapes reflecting the projection of each of the M considered dipoles on the electrodes. The weight attributed to each dipolar function corresponds to the relative amplitude of the corresponding dipole. On might finally interpolate over these estimated relative amplitudes to provide an activation map of the cortical surface. Further in next section we will describe the equivalence between our estimate, Surface Laplacians and Electric Source Imaging (ESI).

3.1.5 Analogy with SL and ESI

Although relying on purely geometrical considerations, we can identify noteworthy parallels between our DCM approach and classic methods for cortical mapping (section 2.3).

The analogy to surface Laplacians can first be visualized by comparing the transform matrix $\mathbf{H}^{-1}$ applied to the measured potentials $\mathbf{v}$ with the simple Hjorth (see section 2.2.2) discrete Laplacian montage from the measured EEG (see **Figure** 3.6). Indeed, as in the case of the Hjorth's Laplacian, the elements of inverted matrix $\mathbf{H}^{-1}$ correspond to the weights given to the electrodes. In the basic Laplacian the weights are unitary on the diagonal, $-1/4$ on the neighbouring electrodes and 0 elsewhere. For the DCM the weights vary on the diagonal, because of the depth d_{kk} of the dipole, and on the off-diagonal with respect to the distance between the electrodes.

Furthermore, both of the RBFs $h_p(x)$ and $h_s(x)$ define families of parametrized basis functions, similar to the RBFs used in the surface Laplacian approaches. In particular, it is interesting to notice that the planar approximation (3.4) of the DCM corresponds to the second order derivative on a plane of a multi-quadric spline defined in **equation** (3.11).

$$\phi(r) = \sqrt{1 + \frac{r^2}{\sigma^2}} \tag{3.11}$$

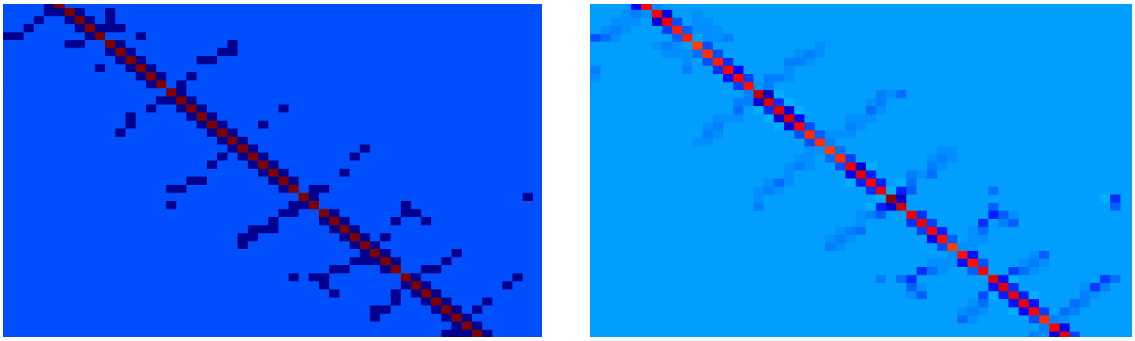

(a) Hjorth Laplacian **(b)** DCM_P

Figure 3.6: The transform matrices corresponing to the Hjorth's Laplacian (left) and DCM planar case(right)

the second order derivative of this function follows as:

$$\phi(r)'' = \frac{\sigma}{(\sigma^2 + r^2)^{\frac{3}{2}}} \tag{3.12}$$

One might notice the equivalence between both **equation** (3.12) and (3.4). The difference between both approaches resides in the way the interpolation are operated. In the case of the SL approaches, the scalp map is first interpolated by an RBF (*e.g.*, this of **equation** 3.11). The second derivative of this interpolated scalp map is taken as an estimate of the cortical map, thus being a weighted sum of the second derivative of the considered RBF (given by **equation** 3.12 in our example). In the DCM case, the scalp map is directly interpolated by the RBF to produce point estimates of the underlying cortical dipolar activations.

On the other hand, one can also notice that the general (3.2) rule correspond to an infinite homogeneous and isotropic propagation medium, for which the conductivity information was discarded (fixing $C = 1$), as we are only interested in the morphology of the cortical map. Indeed, considering $C = 4\pi\sigma$, with σ the estimated conductivity, we get the equation for the electro-magnetic propagation of a dipole in an infinite homogeneous environment (**equation** 2.2). Within this frame, our initial interpolation problem using smooth physiologically founded functions has turned into a full-rank inversion of a infinite homogeneous forward model (3.10).

It is noteworthy that replacing Laplacian estimations of the current sources with inverse models was already proposed for brain source estimation, but only at a microscopic scale. Indeed, classical current source density methods (CSD) (88) were the microelectrode linear equivalent of Hjorth Laplacian montages on the scalp surface, and they were developed into so-called inverse CSD since

2006 (78, 101). The approach presented in this chapter follows the same path, except for source modeling (a point dipole source in our case, a surface monopole in iCSD).

Also it should be highlighted that if cortical source activity can be estimated by full-rank inversion of a matrix constructed from physiologically founded RBF, one might even choose more realistic RBFs, derived directly from imaging based head-modeling (BEM or FEM in sections 2.1.3.1 and 2.1.3.2). Although the analytical expressions for the corresponding DCM_{BEM} or DCM_{FEM} cannot be given as in (3.4) or (3.7), the **H** matrix can still be constructed numerically and thus the interpolation can be obtained.

3.2 Simulation and results

The aim of this section is to compare the performances of the proposed DCM methods with both surface Laplacians and ESI minimum norm inverse solutions using realistic head model.

3.2.1 Simulation set-up

A three layer Boundary Element Model (BEM) of the head was extracted from anatomical MRI using *Brainstorm* (123), yielding a mesh where each layer consists of 1922 points. The electrodes were simulated as a *BioSemi* sensor cap of either 64 or 128 electrodes. This is done in order to achieve good scalp potential interpolation that depend on the electrode spatial distribution on the scalp. In fact the electrodes should be spaced and placed as uniform and dense as possible to avoid any interpolation errors.

For source generation, we assumed randomly placed patches of synchronized dipoles placed 5mm below the inner skull layer (approximated as a cortical surface), which roughly corresponds to the upper half of the brain mesh (1309 dipoles to avoid border effects), oriented radially to the cortical surface and having random but synchronized amplitudes. Those dipoles produce potentials on the cortical surface and are simulated as follows. One or three random locations 5mm below the inner skull surface are chosen. These locations corresponds to the center of the patch. Then for each patch its size or neighbourhood is chosen varying randomly between 20 and 120 mesh points, corresponding roughly to 2.5 to 20cm^2. Finally randomly generated (positive or negative) and synchronized amplitudes are assigned to each patch thus potentials **v** on the electrodes, as well as the simulated cortical map (potentials on the inner skull that are used as a ground truth) were generated by the forward solution through Helsinki BEM library (120). One might argue to use simple dipoles located in different depths in order to produce smooth patches on the cortical surface

but our proposed set-up allows the patches to overlap and thus form spatially complex active regions. In this way we ensure additional difficulty for smooth interpolation functions used for SL and DCM.

We considered both the case of one active patch per time instant and the most complex case of 3 multiple simultaneous activations. We consider a so-called free noise case with SNR of 100dB, and we also considered two noise levels perturbing the electrodes $\mathbf{v}$ by adding white Gaussian noise with signal to noise ratios (SNR) of 20dB and 10dB.

To estimate the surface Laplacians we use SSL MATLAB toolbox, which provides two estimates: a spherical approximation based on New Orleans Spline Laplacians (79) and a realistic case taken from (32) and explained in the Chapter 2 of this thesis (see section 2.2.3.2).

DCM were carried out using either the planar (3.4) or the spherical (3.7) RBF. For the spherical case, we fitted the sphere using FieldTrip (95) toolbox. Depths d_{kk} (*i.e.*, distances between cortex and scalp) and, when necessary, angles α_{jk} were extracted from the MRI. We also extract the inner skull surface, which is assumed to be the cortical layer. We have also computed a DCM_{BEM} using the known BEM model (which can be seen as the best possible geometrical approximation).

ESI minimum norm estimates (MNE) were obtained by pseudo-inverting a realistic BEM model giving the gain matrix between the cortical surface and the electrodes ($P \times M$, with $P = 1309$ and $M = 64$ or 128.

The performance of the methods are evaluated using the correlation $\rho_{(\hat{\mathbf{s}},\mathbf{s})}$ between the estimated cortical activities using DCM, SL and ESI $\hat{\mathbf{s}}$ and the computed (true) cortical activity $\mathbf{s}$. We provide two type of comparison, a discrete one where the correlation is computed only considering the values obtained at the position of the underlying dipoles, and a continuous one where the DCMs discrete cortical maps are interpolated using cubic splines to provide a continuous image of the cortical activations.

The position of the dipoles on the cortical layer are set using a closest neighbour criterion (smallest euclidean distance from sensor e_i to cortical mesh points). This can be done due to the chosen head model, all layers (scalp, outer and inner skull) being smooth and convex type volumes which guarantee to find a closest mesh point on the inner skull surface approximately under the corresponding scalp electrode.

3.2.2 Results

The results presented here were obtained after averaging 1000 simulations performed using the set-up described above. In other words, 1000 random BEM generated cortical maps were compared with the estimated maps obtained either by SL, DCM or MNE.

Table (3.1) presents the results for the unique active region and for multiple simultaneous activations for noise-free measurements and for 2 noise levels (20dB and 10dB). All methods in noise free

Table 3.1: One active patch. Correlation percentage ρ between the forward computed cortical map and the different estimations, with 64 / 128 scalp electrodes whereas gray values under 64s / 128s corresponds to the correlation percentage between the forward computed scalp map and the different estimations. **DISCRETE** stands for the estimated potentials under the electrode sites. **CONTINUOUS** indicates that the discrete results were interpolated using spline interpolation as explained in (76). In all cases BEM_{mne} is estimated on the complete inner skull surface without interpolation.

	Noise-free				20dB				10dB			
DISCRETE	64	64s	128	128s	64	64s	128	128s	64	64s	128	128s
DCM_p	0,84	0,97	0,87	0,96	0,82	0,95	**0,77**	0,86	0,70	0,81	**0,49**	0,54
DCM_s	0,87	0,98	**0,88**	0,95	**0,84**	0,95	0,75	0,81	**0,71**	0,80	0,44	0,47
SSL_s	**0,93**	0,69	0,86	0,63	0,74	0,55	0,48	0,36	0,38	0,29	0,19	0,14
SSL_g	0,90	0,72	**0,88**	0,70	0,75	0,60	0,55	0,44	0,41	0,33	0,23	0,18
DCM_{BEM}	0,96	0,83	0,96	0,76	0,83	0,71	0,41	0,33	0,48	0,42	0,14	0,11
CONTINUOUS	64	64s	128	128s	64	64s	128	128s	64	64s	128	128s
DCM_p	0,84	0,98	0,88	0,96	0,83	0,96	**0,80**	0,88	**0,73**	0,84	**0,54**	0,59
DCM_s	0,86	0,98	**0,89**	0,95	**0,84**	0,96	0,78	0,84	**0,73**	0,83	**0,48**	0,52
SSL_s	**0,91**	0,71	0,88	0,67	0,76	0,60	0,54	0,42	0,43	0,34	0,22	0,18
SSL_g	0,90	0,75	**0,89**	0,72	0,77	0,65	0,60	0,50	0,46	0,38	0,26	0,22
DCM_{BEM}	0,94	0,84	0,96	0,77	0,84	0,75	0,47	0,39	0,53	0,47	0,17	0,14
BEM_{MNE}	0,94	0,23	0,97	0,22	0,72	0,18	0,23	0,05	0,34	0,09	0,08	0,02

case perform rather good with a strong advantage for BEM, as it was expected for such elaborated (informed) model. One might notice that the interpolated DCM_{BEM} proves to be a strong equivalent for standard BEM_{MNE} for noise-free case and outperforms when noise is present.

Both SSL_{sph} and SSL_{geo} perform well for high SNR with an advantage of SSL_{geo} for decreased SNR. Our DCMs proves to be competitive to standard SL when number of electrodes is rather small and outperforms for high resolution EEG set-up. In addition to the current simulation where dipoles were placed 5mm deep, we simulated also using depth of 2mm. We observed that all DCMs are sensitive to the depth of the equivalent dipoles where the results shows that superficial dipoles approximates less the true cortical potentials which is related to the simulated patch size spatial sampling

(number of equivalent dipoles).

Another interesting observation is related to the correlation of estimation and simulated scalp map. It is easy to see that all DCMs shares high correlations with scalp potentials. This leads to the conclusion that indeed the estimations are not far from the originally measured data especially DCM_p and DCM_s.

Further the results in **Table** 3.2 of 3 active patches are shown. In the same way as in **Table** 3.1, the results in **Table** 3.2 shows that all methods perform badly for noisy signals and high-density measurements, with at most 75% correlation for linearly interpolated DCM using 64 electrodes. Indeed, as the cut-off frequency of the surface Laplacian (high-pass) filters increases with the spatial

Table 3.2: Three active patches. Correlation percentage ρ between the forward computed cortical map and the different estimations, with 64 / 128 scalp electrodes whereas gray values under 64s / 128s corresponds to the correlation percentage between the forward computed scalp map and the different estimations. **DISCRETE** stands for the estimated potentials under the electrode sites. **CONTINUOUS** indicates that the discrete results were interpolated using spline interpolation as explained in (76). In all cases BEM_{mne} is estimated on the complete inner skull surface without interpolation.

	Noise-free				20dB				10dB			
DISCRETE	64	64s	128	128s	64	64s	128	128s	64	64s	128	128s
DCM_p	0,85	0,97	0,87	0,96	0,83	0,95	**0,79**	0,87	0,73	0,83	**0,51**	0,56
DCM_s	0,87	0,98	**0,88**	0,96	**0,85**	0,96	0,77	0,84	**0,73**	0,82	0,45	0,49
SSL_s	**0,91**	0,70	0,83	0,64	0,75	0,58	0,49	0,38	0,39	0,30	0,19	0,15
SSL_g	0,90	0,73	**0,87**	0,71	0,77	0,63	0,57	0,47	0,43	0,35	0,24	0,20
DCM_{BEM}	0,95	0,84	0,96	0,78	0,84	0,74	0,41	0,34	0,49	0,43	0,14	0,12
CONTINUOUS	64	64s	128	128s	64	64s	128	128s	64	64s	128	128s
DCM_p	0,85	0,97	0,88	0,96	0,84	0,96	**0,82**	0,89	**0,75**	0,86	**0,56**	0,61
DCM_s	0,87	0,98	**0,89**	0,96	**0,85**	0,96	0,80	0,86	**0,76**	0,85	**0,50**	0,55
SSL_s	**0,90**	0,72	0,86	0,68	0,78	0,63	0,56	0,45	0,45	0,36	0,23	0,19
SSL_g	0,89	0,76	**0,88**	0,74	0,79	0,68	0,62	0,53	0,48	0,41	0,27	0,24
DCM_{BEM}	0,94	0,85	0,95	0,79	0,85	0,77	0,48	0,40	0,55	0,49	0,17	0,14
BEM_{MNE}	0,94	0,24	0,97	0,23	0,73	0,19	0,23	0,06	0,35	0,09	0,08	0,02

density of the electrodes, the high density montages are more affected by noise. On the other hand, when the noise is absent, the estimations of DCM are competing with standard surface Laplacians

(besides the performance of SSL highly depends on the initialization step) when the electrode density is high. Finally, another general observation is that the number of active regions has a relatively low influence on the results.

Comparing the methods, one can notice that DCM_S performs slightly better than DCM_P in no-noise or low-noise cases which accords with our hypothesis that geometrical approximation indeed has an impact on estimation quality. Finally, as expected, the fully informed BEM performs better when noise is weak but the performance for increased noise levels the influence of the approximated geometry decreases.

An example of different estimations obtained from 128 electrodes in the no-noise situation is given figure 3.7. The cortical maps were interpolated for visualization purposes.

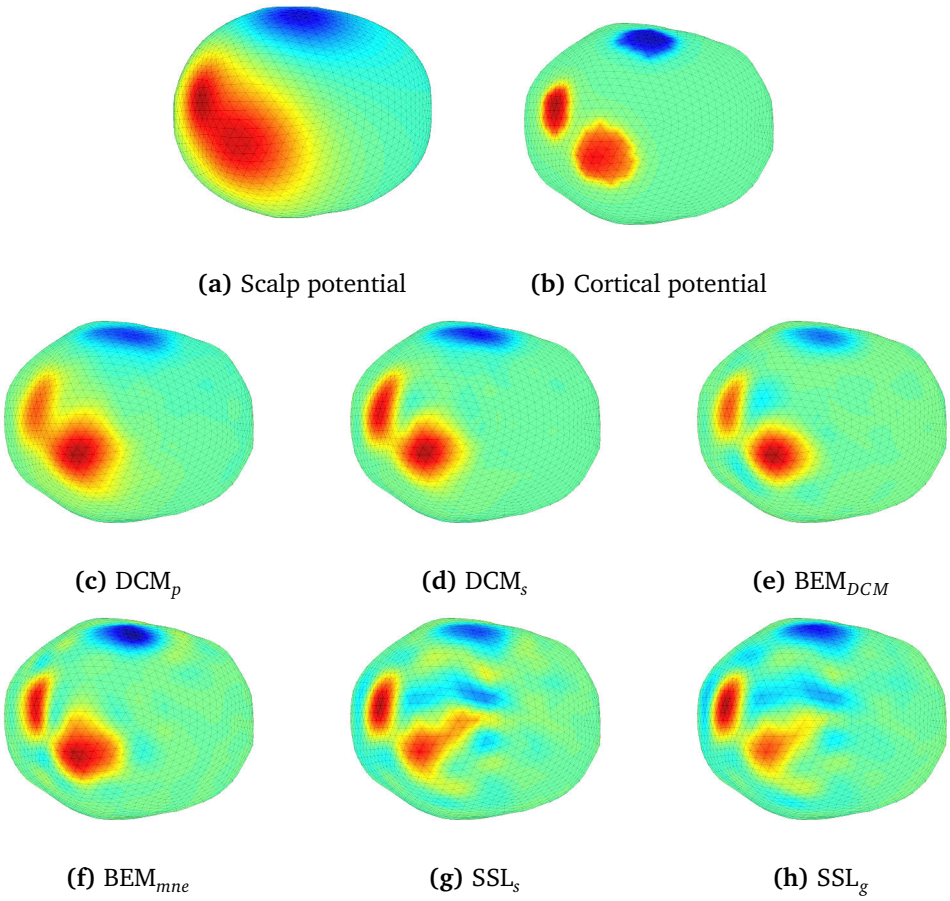

(a) Scalp potential **(b)** Cortical potential

(c) DCM_p **(d)** DCM_s **(e)** BEM_{DCM}

(f) BEM_{mne} **(g)** SSL_s **(h)** SSL_g

Figure 3.7: Forward computed cortical (a) and scalp (b) maps and the obtained cortical activation estimations (c,d,e,f,g) using 128 EEG sensors interpolated using 3D spherical splines (76).

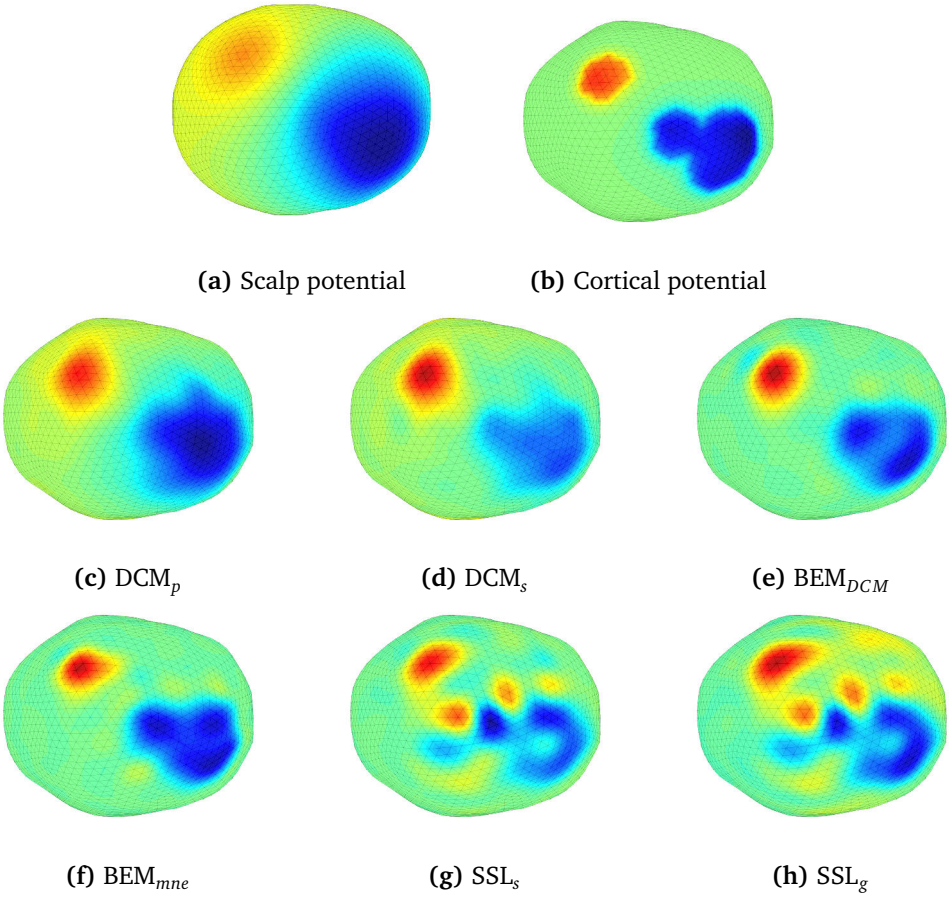

(a) Scalp potential **(b)** Cortical potential

(c) DCM_p **(d)** DCM_s **(e)** BEM_{DCM}

(f) BEM_{mne} **(g)** SSL_s **(h)** SSL_g

Figure 3.8: Forward computed cortical (a) and scalp (b) maps and the obtained cortical activation estimations (c,d,e,f,g) using 128 EEG sensors interpolated using 3D spherical splines (76).

The computational time for different cortical source imaging methods are presented in **Table** 3.3. One might notice that our approximations are beneficial from both initialization and computational time point of view when comparing to other methods. Initialization for DCM_p and DCM_s means the computation of a propagation matrix, given a geometrical approximation and the positions of the sensors. The initialization of SSL_{geo} is much more arduous due to the manual surface mesh

Table 3.3: Computational time for different cortical source imaging techniques.

Time	DCM_s	SSL	MNE
Initialization	**0.03s**	manualy	3min+0.38s
Estimation	**<0.01**	0.47s	<0.01

and electrode position alignment, as well as the head model creation it requires (for more detailed information see (32)). Once this is done, algorithm is fast and yield very nicely made visualization of the SL estimate. The generation of the BEM forward model is much more computationally demanding, up to about 3 minutes in our experiments. The cortical source imaging then reduces to the computation of a pseudo-inverse of the obtained propagation matrix.

3.3 Validation using real data

3.3.1 Data description

We deal with the EEG recording sessions of an epileptic patient, provided by the department of Neurology at the Nancy CHU. The patient was 22 years old at the recording time and was suffering from pharmacological resistant epilepsy. Several recording sessions were performed using a high resolution EEG (EEG-HR) of 64 electrodes, following the 10-10 classical scheme of placement. Sampling frequency was at 1024 Hz and a classical 50Hz notch filter was applied to eliminate a common electro-magnetic external artefact strongly corrupting the recordings.

The patient was explored during several days and several seizures and numerous interictal phenomena were recorded. The origin of the epileptic phenomena was investigated using different preprocessing (filtering) and source localization methods (from equivalent dipoles ECD to MUSIC and distributed approaches such as LORETA) and through clinical examination. Further, the patient was explored using intracerebral electrodes (SEEG) and the diagnosis was confirmed. After surgery, the crisis disappeared.

In order to illustrate the different methods developed in this thesis, we have chosen here a particular interictal window with a duration of 6 seconds, in which neurologists marked several epileptic spikes by inspecting both the F3 and FC3 channels, on which the epileptic spikes are the most visible, suggesting that this focal activity lies within the upper left region. To estimate the cortical areas responsible for these spikes, we manually pick 10 time instances, identified as either being a maximum of a spike or showing a low energy activity between spikes: at 3.74s (spike), 3.77s (spike), 4.18s (spike), 4.23s (spike), 4.42s (low activity, inter-spikes), 4.59s (spike), 4.63s (spike), 4.82s (low activity), 5.03s (spike) and 5.07 (spike) (see **Figure** 3.9).

3.3.2 Results

In all cases we use both DCM and SSL estimates, thus 5 methods in total. For DCM, we also interpolate the results using 3D splines (76) to provide interpretable visual rendering. For visualisation

purpose we scale the potential values between -1 and 1.

From the results **Figure** 3.10 we observed that the performance for all methods is visually comparable, although our DCM seems to be smoother, especially its planar version, as it was observed also in the simulation part. Cortical activations in figure 3.10 are rather difficult to interpret. It seems that a localized source is present in the front left part of the head (location that corresponds to the actual location of the epileptic spikes according to the neurologists, other localization methods, see also next chapter, and surgery outcome), as the red spot appears more or less clearly for time instants located on the peaks of the epileptic spike (columns 2, 3, 4, 6, 7, 9, 10). The rest of the map might be quite different from one method to another. Especially for SSL with multiple sources and sinks which complicate the interpretation. This might be the direct result of the spatial derivative, which could yield a too strong high-pass character to the SSL.

To deal with such complex multichannel recordings, one might apply a band pass filter to cancel low and high oscillations that are not related to the epileptic activity. Indeed, following the preprocessing steps applied for source localization in clinical routine, we applied a FIR band-pass filter between 8 and 48Hz. As it can be seen, the epileptic phenomena appear much clearer after this preprocessing (**Figure** 3.11).

The resulting cortical maps are shown in **Figure** 3.12. Band-pass filtered data shows much less spatial activity except those strong sources and sinks. As time goes one might notice the spatial evolution and correlation between the scalp maps. In the beginning one big active sink is present in the front-left part of the cortex. Further strong activated source can be easily seen in the front-left part of the cortex, except in the fifth and the eighth maps, corresponding to inter-spikes samples. No significant difference is observed between the estimations, except the smoothness, greater for DCM planar.

3.4 Conclusion

The goal of this chapter is to propose cortical potential estimation methods based on simple geometrical assumptions with low computational cost. As a result we propose here a family of informed cortical map estimators (Dipolar Cortical Mapping, DCM) related both to surface Laplacians (SL) and to ESI minimum norm estimates (MNE). The DCM is based on a family of parametrized physiologically plausible radial basis functions that can be seen, depending on the considered approximation, either as an SL technique or an approximate MNE solution. In other words, we show a formal connection between the MNE, the DCM and the SL estimations of the cortical activity.

Besides, some of simpler proposed DCM use easily available information even in the absence of imaging modalities, unlike the recently proposed SSL (and the MNE techniques). Our proposed DCM shows good performance even for simple approximations of the head geometry, such as planar or spherical and remains reliable when multiple cortical areas are simultaneously active.

Depending on the point of view, an advantage or a drawback of the proposed DCM is that it can be easily parametrized by varying the depth of the equivalent dipoles and therefore changing the smoothness of interpolation functions. This can be done by the user while analysing the data, but it could be in principle guided by the anatomy, *i.e.*, by the distance between the actual cortex and the scalp surface. Indeed, when placed closer to the cortical surface, the estimated amplitudes are less influenced by the non local electrodes. On the contrary, deeper placed dipoles take more into account the electrical potential distribution on larger neighbouring electrode sites.

Finally, it is noteworthy that, besides the reduced computational burden, the DCM estimates are much less prone to numerical errors. Indeed, during the simulations, the SSL methods showed an increased sensitivity to the quality of the mesh (faces and vertices must be uniformly distributed and it should be smooth in order to avoid computational errors, and the electrodes must be placed on the faces).

Future development directions could exploit better the anatomical information. The brain geometry in this chapter was approximated as inner skull surface which is very smooth and homogeneous comparing to the real cortical surface. Thus the next logical step would be to use different and more complex brain geometries. Our DCM estimate should also be evaluated for different skull thickness in order to analyse the performance of the smearing effect of the skull. Also, the performance of presented methods should be tested in more realistic noise cases using multiple random noise dipoles.

Another interesting perspective is to relax the constraints imposed on the positions of the equivalent cortical dipoles used by the DCM (*i.e.*, below each EEG electrode) and thus allow sparser solutions due to the fact that there may be not as many activated cortical areas as the electrodes. This research direction is explored further in this thesis.

From an applicative point of view, visualised cortical maps estimates using both DCM and SSL show very similar performance allowing to conclude that interpolation using physiological plausible functions yield similar results.

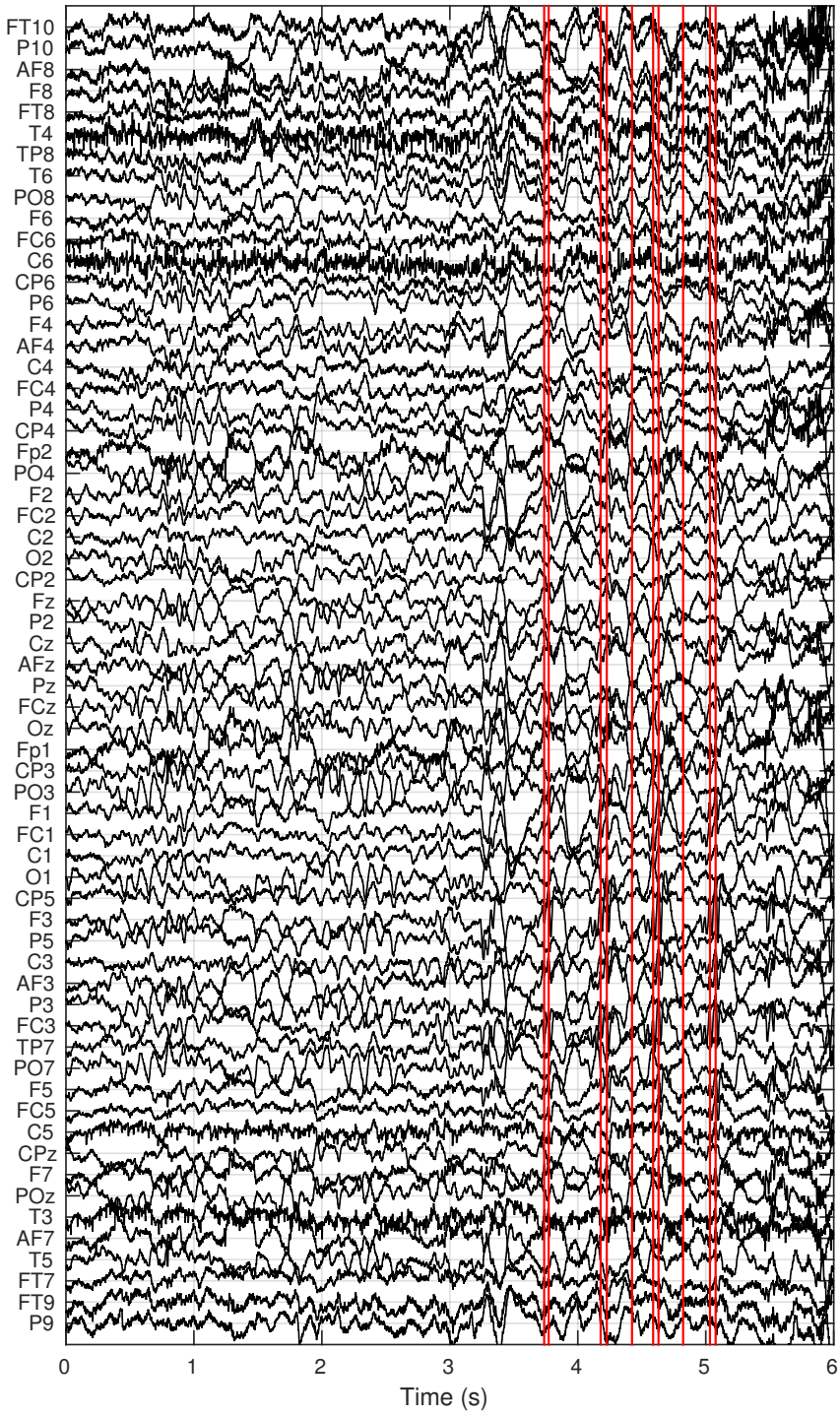

Figure 3.9: Chosen data window. The signals of interest are situated between 3.2s and 5.2s. Ten time instants for which the cortical maps were estimated are marked with vertical red lines (see details in the text).

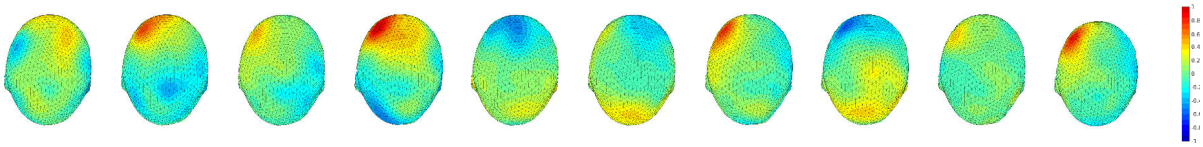

(a) SCALP

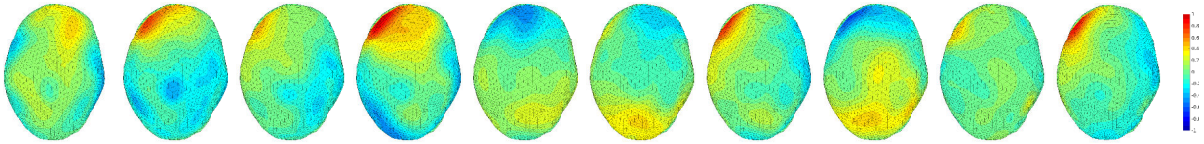

(b) SCALP projected on cortex

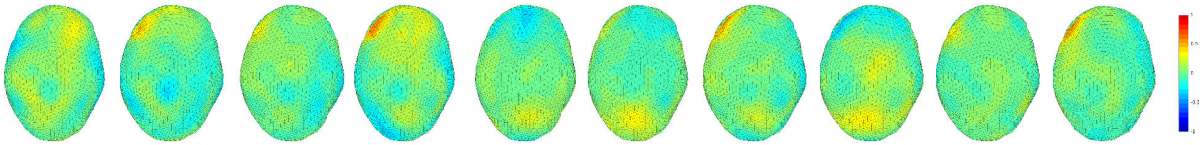

(c) DCM_{pln}

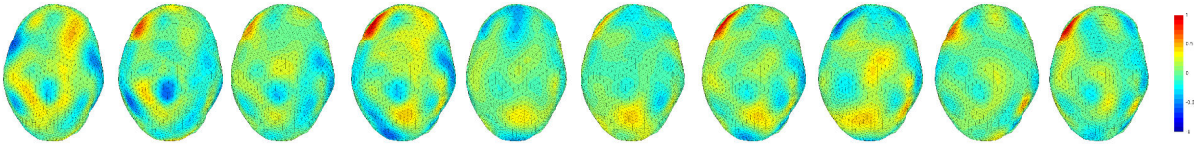

(d) DCM_{sph}

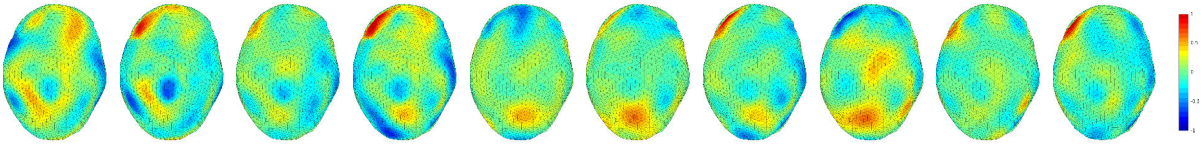

(e) DCM_{BEM}

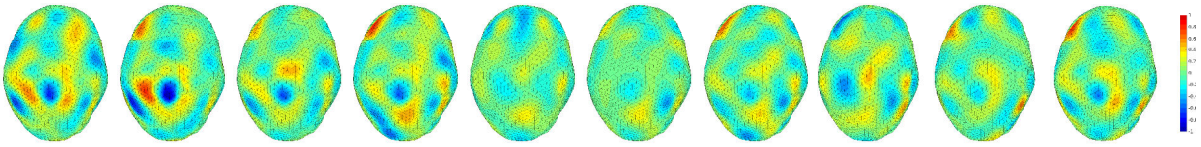

(f) SSL_{sph}

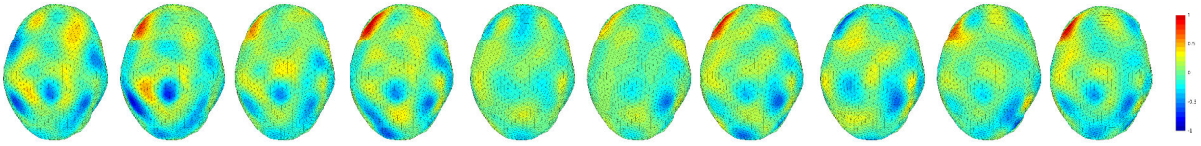

(g) SSL_{geo}

Figure 3.10: Surface Laplacian estimates of several time instances applied on notch-filtered data. For all images nose points up, left side to the left ear, right side to the right ear.

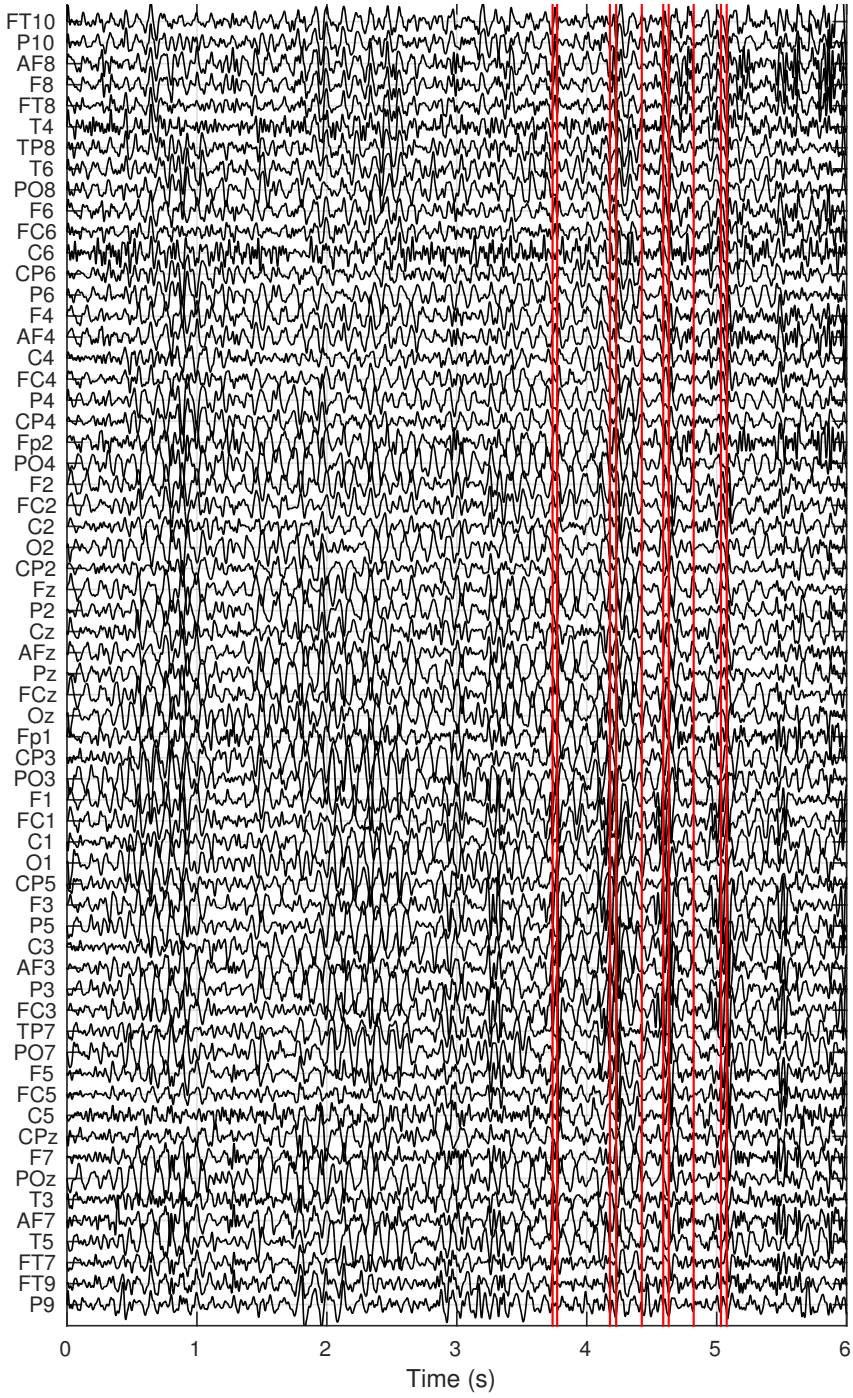

Figure 3.11: Filtered data, same window and marks as in figure 3.9.

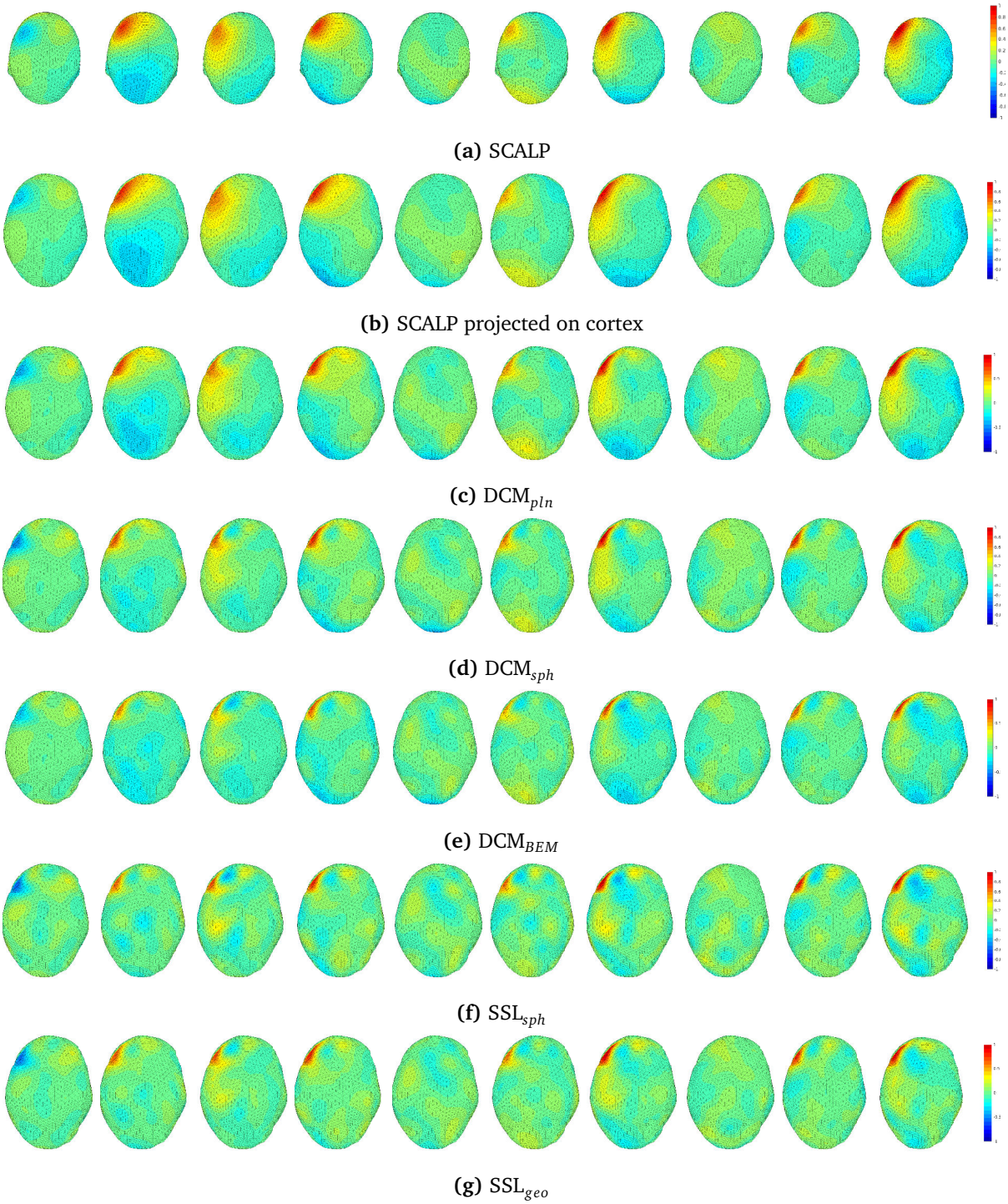

(a) SCALP

(b) SCALP projected on cortex

(c) DCM_{pln}

(d) DCM_{sph}

(e) DCM_{BEM}

(f) SSL_{sph}

(g) SSL_{geo}

Figure 3.12: Surface Laplacian estimates of several time instances applied on band-pass filtered data. For all images nose points up.

Chapter 4

Sparse spatio-temporal EEG decomposition

The Laplacian-derived approaches developed in chapter 3 propose a full rank estimate, providing a severe under-sampling of the cortical surface. To relax this constraint, further in this thesis we adopt a dipolar distributed model. A large number of dipole source candidates are placed in every point of the cortical mesh, with orthogonal orientation to the cortical layer. Pursuing the initial objective of estimating the underlying source configuration by fitting plausible spatial pattern on the measurements, the resulting inversion can be seen as a dictionary-based method where the dictionary atoms consist in the columns of a given forward model.

As mentioned in section 2.3, this family of models yield severely over-determined inverse problem, and a regularization strategy must be applied. We will here adopt a constraint of sparsity, following the assumption that only a few cortical sources are simultaneously active. Such hypothesis is particularly valid in e.g. epileptic context or in the case of cognitive tasks, where a limited number of strong sources are responsible of the visible activity on the EEG electrodes. We will consider the Single Best Replacement (SBR) and Source Deflated Matching Pursuit (SDMP) families of methods, producing efficient methods and avoiding the drawbacks of classical matching pursuit approaches, as stated in the section 2.3.4.5.

Considering a dense distribution of the dipoles on the cortical layer, the columns of the forward matrix share high correlations, a context where MP-based methods like the SBR approach are of particular interest to select the best set of atoms among a large number of solutions. However the inherent uncertainty of the data due to the noise and to the forward problem approximations make the problem particularly complex. To enforce the regularization as well as the sparsity of the solution,

we take benefit of the temporal dimension of the data, and we propose two combined spatio-temporal dictionaries similarly as shown in (103), where the temporal atoms are extracted from the data. First dictionary is constructed using the temporal atoms based on a principal component analysis. The second and more elaborated dictionary exploit a time-frequency decomposition of the data based on wavelets, such analysis being more robust to noise and well adapted to the non-stationary nature of the electrophysiologic data.

4.1 Space-Time dictionary

The Principal Component Analysis (PCA) is a popular technique for multivariate data denoising, data dimension reduction and significant temporal structure extraction. In this chapter, we would like to use PCA for extracting the essential structure of the signal and separate it from the the noise. If the sources are not synchronized, the scalp activity should be explained by at most K dipolar sources, with K the dimension of the source space. Each of these dipolar sources is given the temporal activity of one of the principal components. We will rely on the matching pursuit approach to select the best position for these dipoles based on the atoms of the spatial dictionary and to provide a sparse scalp map. The temporal structure given by the PCA is expected to impose the temporal stationarity of the sources on large portion of the analyzed windows, and to avoid flickering effect of the cortical map as observed when the decomposition is based on a spatial dictionary (lead-field) only. As opposite to MUSIC-like approach, synchronized sources can be retrieved by affecting the same PCA component(s) to several positions.

The main difficulty reside in the estimation of the number of significant features in the signal (*i.e.*, the size of the source space). Depending on the nature of the noise, the estimation of the source space dimension is not straightforward. Under independent white Gaussian noise assumption, one might use MDL (Minimum Description Length) to extract the K most significant eigen-vectors forming the source space.

The PCA decomposition classically begins by a computation of the covariance $\mathbf{C}$ of the surface potentials $\mathbf{V}$:

$$\mathbf{C} = \mathrm{E}[(\mathbf{V} - \mathrm{E}[\mathbf{V}])(\mathbf{V} - \mathrm{E}[\mathbf{V}])^T] \tag{4.1}$$

where $E[.]$ denotes the empirical expectation. We then apply the eigen decomposition of the covariance matrix $\mathbf{C} = \mathbf{U}\mathbf{\Sigma}\mathbf{U}^{-1}$, with $\mathbf{\Sigma}$ the diagonal matrix of eigenvalues and $\mathbf{U}$ the corresponding eigenvectors. The K selected principal components, selected from *e.g.*, a MDL analysis, form a PCA

temporal dictionary $\mathbf{D}_{pca}$:

$$\mathbf{D}_{pca} = \{U_1, U_2, \cdots, U_K\} \tag{4.2}$$

With such dictionary the measured potentials can be explained up to the estimated noise level, which directly depends of K $(N-K)$ being the size of the noise space, with N the number of electrodes. This dictionary is simple and fast to compute. It is noteworthy to point out that for this kind of dictionary the number of sources must be estimated correctly. When overestimated, the dictionary atoms will contain noise amplitudes which will disturb the reconstruction and localization performance.

We now combine the PCA time-frequency dictionary $\mathbf{D}_{PCA}$ with the spatial dictionary (*i.e.*, the lead-field matrix $\mathbf{A}$). Let this space-time-frequency dictionary be $\mathbf{H} = \{\mathbf{h}_{ij}\}$, where each element $\mathbf{h}_{ij}$ of size $N \times T$ (T being the number of time samples) is a rank one matrix obtained by:

$$\mathbf{h}_{ij} = \mathbf{a}_i \mathbf{d}_j \tag{4.3}$$

where a_i is the element of lead-field matrix $\mathbf{A}$, d_j a j—th principal component. For implementation reasons, we store each dictionary element $\mathbf{h}_{ij}$ as a vector with dimensions $(NT) \times 1$. The whole spatio-temporal dictionary $\mathbf{H}$ is with dimensions $(NT) \times K$, with K the number of estimated PCA components, and the decomposition is done on the reshaped data $\mathbf{V}^*$ of dimensions $(NT) \times 1$.

4.2 Space-Time-frequency dictionary

The PCA components does not take into account the non-stationary nature of brain sources. However the dynamics of the sources are most of the time transient and are known to lie within particular time-frequency subspaces. It is in particular the case when studying the dynamic of epileptic seizures (57) or of steady-state evoked potential (136). To address the more general case of non-stationary sources, we therefore propose to construct our dictionary in the wavelet domain, more precisely by using orthogonal real wavelets. The advantage of such approach is the small temporal support of the wavelet coefficients and they can be used individually to efficiently capture specific time-frequency characteristics of the sources, while preserving smoothness. Moreover, the compression ability of the wavelets leads to sparse time-frequency representations of the signal of interest and thus to less computationally expensive solutions. Fast algorithms are available for both wavelet decomposition and reconstruction.

In the following, we assume that every signal of length T is decomposed up to the depth J (the number of detail scales) and thus that on every scale j we have $T/2^j$ wavelet coefficients. To generate sparse wavelet dictionary $\mathbf{D}_w$, we apply wavelet coefficient threshold as a denoising procedure

directly to the noisy data. Although one might argue that proper multichannel de-noising require both PCA and wavelet thresholding steps (2), we want to highlight that even if in our simulations we use correlated signals, the results were similar for both cases with and without using PCA de-noising. This approach applies only on our particular set-up which is explained further in section 4.4.

A lot of thresholding techniques exist in the literature (see for example (5) for a review). We tested only the classical solutions proposed by Donoho and Johnstone (33) (universal and SURE thresholding), as well as a combination of them, suggested under the name of hysteresis thresholding in (105), and slightly modified here, as explained further.

By its construction (aiming to preserve as much signal as possible even if some noise remains present), the SURE threshold is rather low and preserves a lot of coefficients, increasing thus the size of the wavelet dictionary. On the other hand, the universal threshold aims to eliminate the estimated noise completely and keeps only the strong coefficients with big amplitudes. It yields a very sparse temporal approximation, in principle less accurate than the SURE threshold but almost noise-free (for details see (5) and (33)).

Hysteresis threshold aims to exploit the advantages of both: it preserves all the coefficients selected by the universal threshold and adds all the SURE-selected coefficients that are connected, in the time-frequency plane, with one of the universal coefficients. Taking into account that each universal coefficient is also preserved by SURE threshold, this technique simply consists in labeling the connected components in a 2-dimensional binary image. At first we label each isolated coefficient or isolated connected group of coefficients in time-frequency scale. Once binary images of both universal and SURE thresholds are labeled, one can detect the hysteresis coefficients by a simple subtraction, where each individual labeled coefficient group from universal threshold is being subtracted from the SURE labeled coefficients. Those groups of coefficient in the SURE labeled image impacted by the subtraction are preserved as Hysteresis coefficients (see coefficients in Fig. 4.1). Let $\mathbf{v}_w^i$ be the vector of "clean" wavelet coefficients after applying wavelet threshold to the noisy data channel $\mathbf{v}^i$. Each non-null coefficient represents the time-frequency support of a wavelet coding a significant feature of the analysed signal $\mathbf{v}^i$, and we can construct a binary mask corresponding to these supports (see Fig. 4.1). A logical OR among all masks (obtained for all channels) yields a complete mask, where the non-null elements designate all the necessary wavelets for the approximate noise free reconstruction of the complete measurements matrix $\mathbf{V}$. Each individual coefficient corresponds in fact to a time-frequency dictionary element $w_{p_j}^j$, which is a wavelet on scale (frequency band) j at time-shift p_j. The complete time-frequency dictionary is then the family of selected wavelets $\mathbf{D}_w = \{w_{p_j}^j\}$, with scales $j \in \{1, \cdots, J\}$ and time shifts $p_j \in \{1, \cdots, T/2^j\}$.

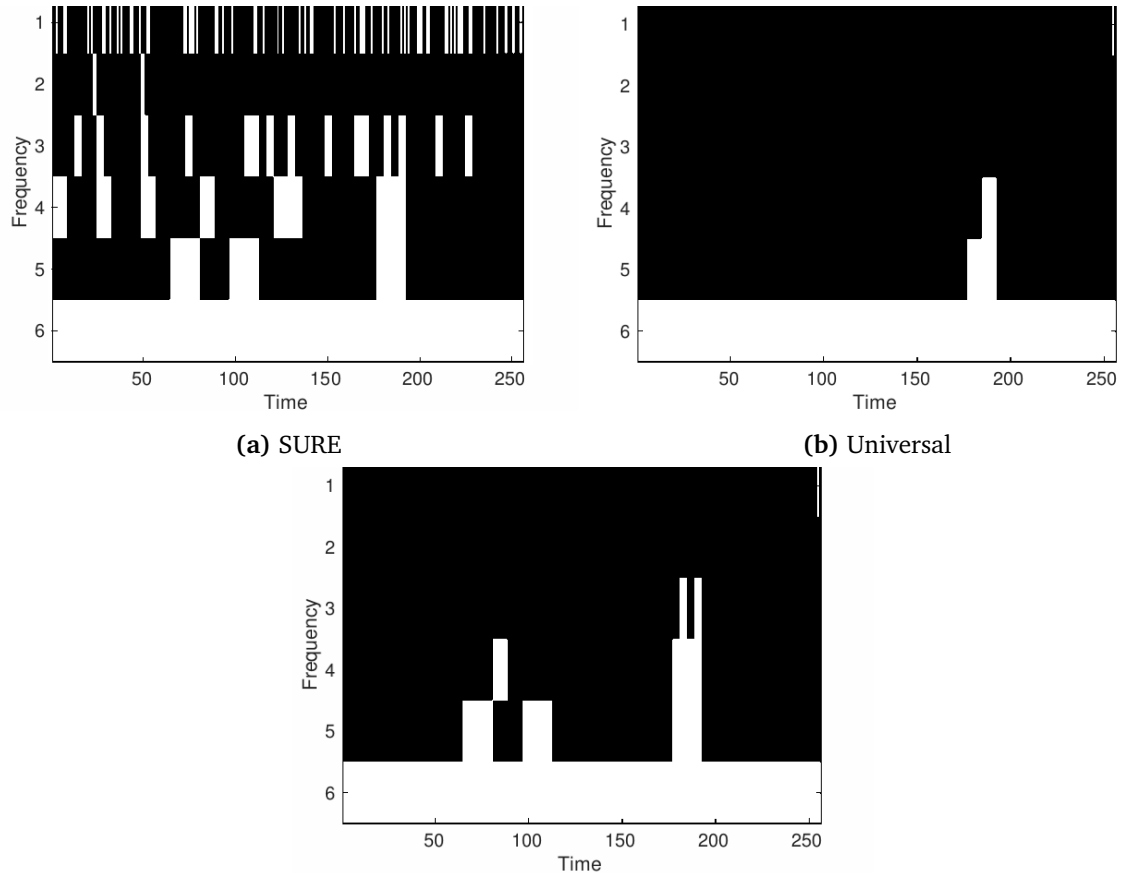

(a) SURE **(b)** Universal

(c) Hysteresis

Figure 4.1: Binary image of coefficients obtained using SURE, universal and hysteresis wavelet threshold. In all images horizontal axis - time, vertical - scale (frequency band).

Finally, the wavelet dictionary $\mathbf{D}_w$ need to be combined with the corresponding columns of the lead-field. Let this space-time-frequency element dictionary be $\mathbf{H} = \{\mathbf{h}_{ip_jj}\}$, where each element $\mathbf{h}_{ip_jj}$ of dimension $N \times T^j$ (T^j being the support size of the wavelets at scale j) is a rank one matrix obtained by:

$$\mathbf{h}_{ip_jj} = \mathbf{a}_i w^j_{p_j} \tag{4.4}$$

In the EEG application addressed in this work, $\mathbf{H}$ can be seen as a set of time-varying scalp-maps shifted in time and frequency. In the following, we will simplify the notation by dropping the subscript ${p_j}^j$, j will denote a given time shift in a given wavelet scale.

4.3 Spatio-Temporal Matching Pursuit

Regardless of the dictionary, multichannel observation data $\mathbf{V}$ can be approximated as a weighted sum of the spatio-temporal atoms:

$$\hat{\mathbf{V}} = \sum_i \sum_j b_{ij} \mathbf{h}_{ij} \tag{4.5}$$

where b_{ij} denotes the scalar amplitude whereas $\mathbf{h}_{ij}$ is a rank one matrix that implies the temporal characteristic $\mathbf{d}_i$ from temporal dictionary $\mathbf{D}$ for individual point dipole lead-field column $\mathbf{a}_j$. The minimization problem for Matching Pursuit (in our work we refer to SBR and SDMP) thus is formulated as follows:

$$min_{\mathbf{b}} \{\mathscr{J}(\mathbf{b}, \lambda) = ||\mathbf{V} - \hat{\mathbf{V}}||_2^2 + \lambda ||\mathbf{b}||_0\} \tag{4.6}$$

with the term $\lambda||\mathbf{b}||_0$ balancing the number of nonzero weighting elements in $\mathbf{b}$ (*i.e.*, selected rank one matrices $\mathbf{h}_{ij}$), regularizing the sparsity simultaneously in space and time-frequency.

The choice of an optimal sparsity parameter λ is a difficult task. As this parameter is used for selecting the significant atoms explaining the signal of interest (source projections) but not the noise components, it should be of the order of the noise energy $\mathscr{E}_n$ (144). A more detailed analysis of the influence of this parameter is given in the results section.

In case of SDMP the number of sources N_s is assumed to be known or estimated and thus writes:

$$min||\mathbf{V} - \sum_i \sum_j^{N_s} b_{ij} \mathbf{h}_{ij}||_2^2 \tag{4.7}$$

The residual is minimized considering the given fixed number of locations for each individual wavelet support. Similarly as the estimation of the parameter λ in the case of the SBR algorithm, the estimation of the number of sources is difficult. Both issues are actually connected because they both rely on a source/noise subspace analysis and they will be analyzed in the Results section.

Further we will briefly discuss the practical aspects of implementing such space-time and space-time-frequency dictionaries using the forward-backward matching pursuit extensions (SBR and SDMP) described in section 2.3.4.5.

4.3.1 Practical guidelines using $\mathbf{D}_{pca}$

In stationary case where the $\mathbf{D}_{pca}$ is assumed the dictionary $\mathbf{H}$ is computed as follows:

$$\mathbf{H} = \{\mathbf{h}_{ij}\} \tag{4.8}$$

As explained previously in equation (4.3), spatio-temporal atom is computed as follows: $\mathbf{h}_{ij} = \mathbf{D}_{pca,i}\mathbf{A}_j$, where $\mathbf{A}$ stands for the lead-field matrix and $\mathbf{D}_{pca,i}$ is the i-th element of the temporal dictionary. In fact such approach does not seem to be effective because the size of the space-time dictionary $\mathbf{H}$ changes a lot for small changes in D_w or $\mathbf{A}$. In fact, depending on the estimated principal components K, the size of $\mathbf{H}$ is $(N \times T) \times (K \times M)$. Thus slight changes in K cause huge increase/decrease in $\mathbf{H}$ and, thus, in memory consumption. This leads to a methodology that is very demanding of the computer working memory. Nevertheless if the number of sources is small, this approach is very easy to implement and use.

Decomposition is done over all data length thus assumes temporal stationarity. Therefore in real application one might choose a particular time window of recordings and process them independently. The only requirement is for the computation of PCA. One must consider enough data samples in order to compute the covariance matrix of the data required for the PCA.

The general structure of our proposed Spatio-Temporal SBR (ST_SBR) decomposition procedure is given in **Algorithm 7**.

Algorithm 6 Spatio-Temporal SBR, PCA version

1: **procedure** ST_SBR()
2: **Give or estimate** K: number of biggest principal components
3: **Compute** λ**:** Equation (4.14).
4: **Construct** $\mathbf{D}_{pca}$: 4.2.
5: **Compute H**: Equation (4.3).
6: **Decompose data**: Solve equation (4.6) using SBR.
7: **end procedure**

4.3.2 Practical guidelines using $\mathbf{D}_w$

In the case of PCA dictionary we decomposed all data at once and thus had to invert the $\mathbf{H}$ at each iteration. Here each row contains only N points and we invert only the lead-field matrix $\mathbf{A}$. One might take into account that wavelet de-noising can be seen as a signal compression technique and most of the columns of the resulting $\mathbf{V}_w$ thus are with zero values. This significantly speeds up the estimation process as only the most significant columns of $\mathbf{V}_w$ are reconstructed. Also the sources are allowed to be temporally non-stationary. At first we transform and threshold the noisy recordings $\mathbf{V}$ into the wavelet domain using one of the wavelet thresholds (Universal, Hysteresis or Rigorous) and obtain new de-noised version $\mathbf{V}_w$. The main difference is that the de-noised scalp potentials in

wavelet domain $\mathbf{V}_w$ actually preserves all coefficients of our dictionary $\mathbf{D}_w$ and thus, according to the used threshold, contains all important temporal characteristics we might be interested in. In fact, practical application requires fitting the lead-field columns on the columns of $\mathbf{V}_w$ and thus reconstruct the locations for given coefficients at a certain time-frequency band.

The general structure of our proposed Spatio-Temporal SBR (ST_SBR) decomposition procedure is shown in **Algorithm 7**. One might see 4 fundamental steps are required for data reconstruction.

Algorithm 7 Spatio-Temporal SBR, wavelet version

1: **procedure** ST_SBR()
2: **Estimate noise energy $\mathcal{E}_n$ to compute λ:** Equation (4.14)
3: **Construct $\mathbf{D}_w$**: Wavelet threshold (section 4.2).
4: **Compute H**: Equation (4.4).
5: **Decompose data**: Solve equation (4.6) using SBR.
6: **end procedure**

A very similar but slightly different structure of the Spatio-Temporal SDMP algorithm is given in **Algorithm 8**. The difference being only the fact that exact number of sources N_s must be known.

Algorithm 8 Spatio-Temporal SDMP

1: **procedure** ST_SDMP()
2: **Give or estimate N_s**
3: **Construct $\mathbf{D}_w$**: Wavelet threshold (section 4.2).
4: **Compute H**: Equation (4.4).
5: **Decompose data**: Estimate N_s sources (4.7) using SDMP.
6: **end procedure**

4.4 Simulations and results

The aim of this work is to evaluate the performance of cortical source localization and data reconstruction in the context of non-stationary sources, by use of the proposed spatio-temporal dictionary.

4.4.1 Forward model

In this work we use a realistic three layer (*Colin27*) head model extracted from BRAINSTORM (123) with the skull conductivity assumed as 1/20 of the skin and brain conductivity. We start by simulating a quasi-continuous brain surface using dense discrete layer of 1200 dipoles placed 5mm under the

inner skull surface. The dipoles have fixed orientation normal to the inner skull layer. For realistic simulations, we randomly choose a subset of 8 or 16 dipoles to be active among the 1200 positions. The potentials at 128 simulated BIOSEMI scalp sensors are computed using a isolated skull approach BEM forward model from the Helsinki toolbox (120).

To motivate the choice of the matching pursuit strategies (SDMP and SBR), we point out that the atoms forming our spatial dictionary (lead-field matrix) **A** are highly correlated. We have computed the mean correlation values for each of the cortical layer point lead-field with those of its 5 nearest neighbours (600 points taken as an approximation of the inner skull surface and 4000 points taken for an approximation of real cortical surface extracted from the patients MRI). These correlation values are given on **Figure** 4.2, scaled between 0.5 and 1. One might notice high correlation values

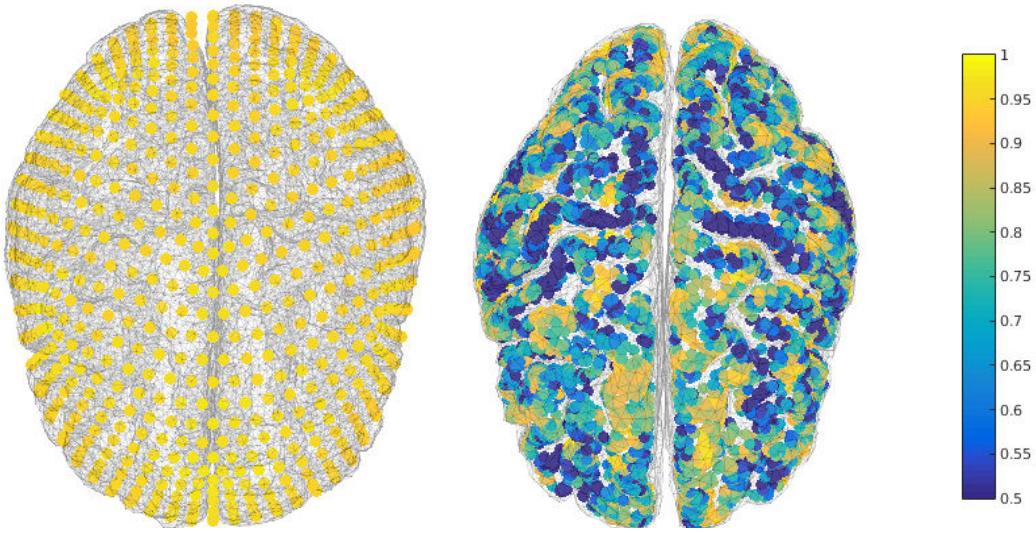

Figure 4.2: Mean of 5 lead-fields neighbor columns correlations. Innerskull (left) and cortical surface (right). Correlation values scaled between 0.5 and 1.

in a lot of regions, which means that the biggest part of the space-time dictionary atoms also will be highly correlated and thus is the main motivation to choose forward-backward optimization schemes.

Further in this thesis we consider both dictionaries: simplified cortical surface using inner skull for simulations and true geometry for validation on the patients data.

4.4.2 Data simulation

To simulate the temporal activity of the sources we assign to the selected dipoles the time-courses of real physiological intracranial recordings measured close to the real epileptic source. Namely, we

choose 2 seconds (512 points using 256Hz sampling frequency) of 8 or 16 SEEG signals to simulate the activated dipoles. Non-stationarity is obtained by considering that each of these dipoles is active during only one epoch within these 2 seconds, with two simultaneous active sources per epoch, *i.e.*, 4 (respectively 8) epochs of 500ms (respectively 250ms) for the 8 (respectively 16) dipoles case. Physiological background activity was simulated by adding to the simulated EEG recordings spatially coloured Gaussian noise (random covariance matrix), with two signal to noise ratios (SNR) of 10dB and 3dB. We provide mean results over 100 simulations for each of the simulated configurations. **Figure** 4.4 shows an example of such non-stationary set-up for the 8 sources configuration. As a

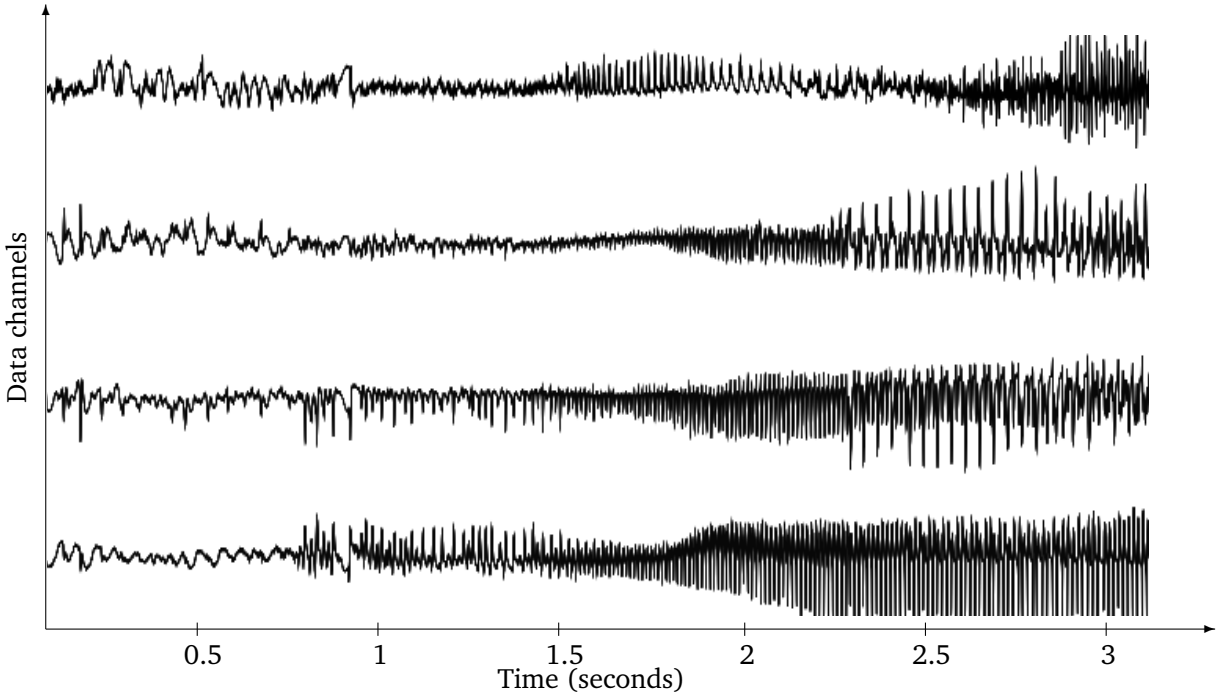

Figure 4.3: The time evolution of the eplipetic crisis measured using SEEG electrodes close to the source. Several seconds in 4 channels are shown.

forward model we further use a realistic three layer (*Colin27*) head model extracted from BRAINSTORM (123) which is based on a real MRI with the diameter of the spherical model. Potentials at 128 simulated BIOSEMI scalp sensors are computed using a BEM forward model from the Helsinki toolbox (120). Two realistic SNR ratios (10dB and 3dB) were tested, adding white Gaussian noise on the recordings. We provide mean results over 100 simulations for each of the simulated configurations.

Fig.4.4 shows and example of such non-stationary set-up for the 8 sources configuration.

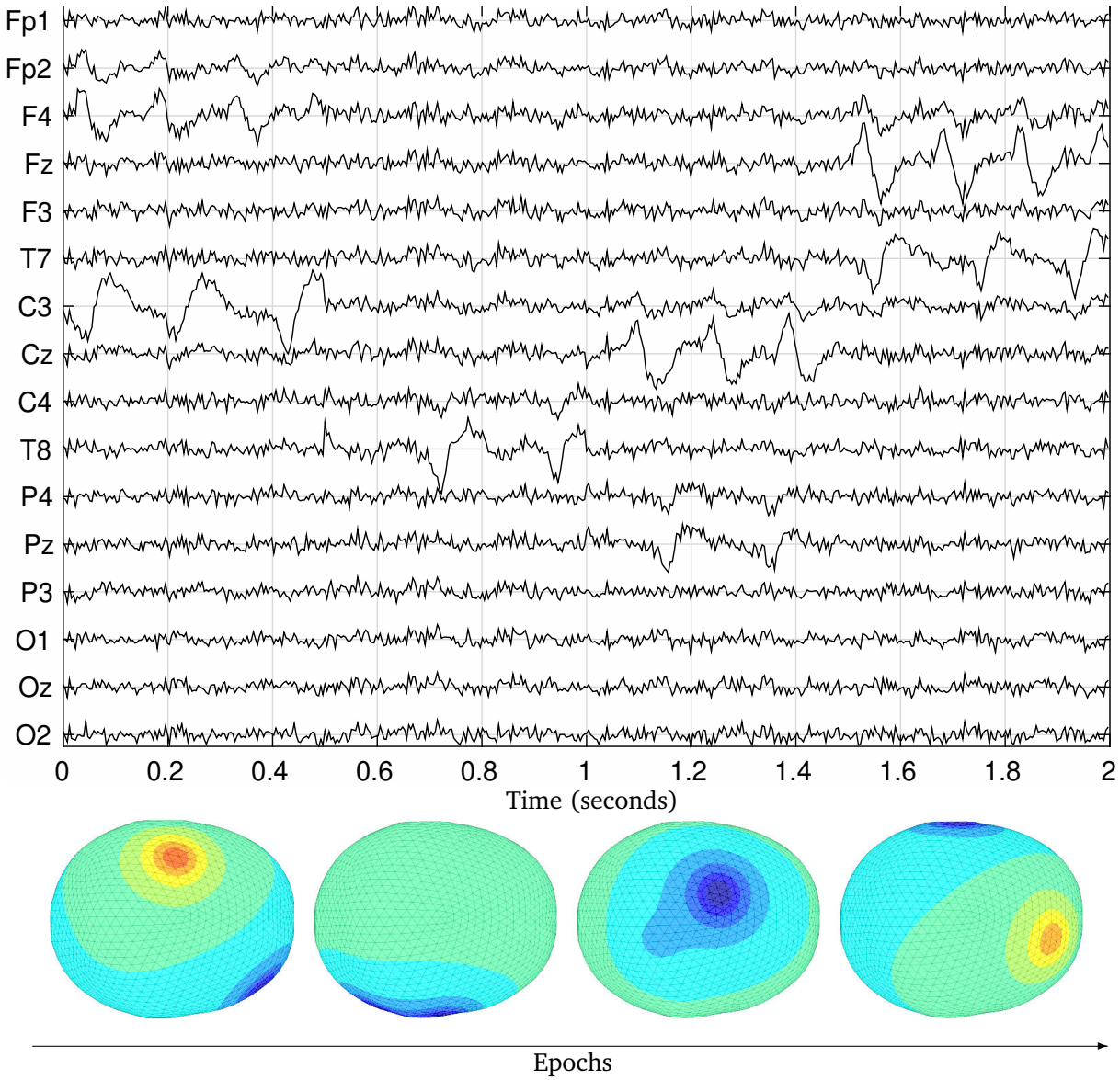

Figure 4.4: An example of the time evolution simulating 8 non-stationary sources over 4 epochs, 2 sources active per epoch. As time goes different locations are active, yielding distinct scalp maps.

The active regions were simulated with equal powers, in order to be able to define the signal-to-noise (SNR) between the active sources and noise scalp projections. The locations (as well as the time courses) of the active sources were randomly chosen, meaning that the SNR slightly varies from a trial to another. The SNR values provided in the tables were obtained by averaging over 100 trials.

Assuming that a numeric solution for the source localization problem (i.e. the possible dipole

locations) is necessarily discrete, we generate the spatial dictionary **A** and compute our solutions on much sparser grid of only 677 dipoles at the same depth (5mm). In other words, as the forward problem is a sampling of the solution space, the found solution will always be an approximation of the true source configuration. Therefore, we assume that a good localization is within an error of 15mm distance from the simulated dipoles (this values corresponds to the mean distance between two neighbouring vertices in the inverse problem), or within the sphere with 30mm diameter centred on the localized dipole position.

4.4.3 Performance measure

In the following, we will consider as a True Positive (TP) an estimated dipole located within 15mm from a simulated dipole. All estimated components that are farther than 15mm are False Positives (FP).

We are interested in both data reconstruction quality and localization accuracy. A Goodness-of-fit (GOF) is used to measure the quality of scalp potential reconstruction:

$$\text{GOF} = 1 - \frac{||\mathbf{V}_{clean} - \hat{\mathbf{V}}||^2}{||\mathbf{V}_{clean}||^2} \tag{4.9}$$

where $\mathbf{V}_{clean}$ corresponds to the noise-free source projection on the scalp, whereas $\hat{\mathbf{V}}$ stands for the reconstructed scalp potentials. We also compute GOF_s replacing in (4.9) $\hat{\mathbf{V}}$ by $\mathbf{V}_{TP}$, that is the reconstruction of the scalp potentials using only TP dipoles. This is done in order to evaluate if the resulting TP indeed explain the original data. The GOF is far from a sufficient statistic to evaluate the accuracy of the source reconstruction. Indeed the problem is under-determined and several configuration of sources might lead to the same scalp map. We thus propose additional criteria assessing the quality of the results.

The Distance Localization Error (DLE), as proposed in (12), gives an estimate of the localization accuracy taking into account both the missed simulated sources (TN) as well as the introduction of spurious sources (FP):

$$\text{DLE} = \frac{1}{2Q}\sum_{k\in I} min_{l\in\hat{I}}||r_k - r_l|| + \frac{1}{2\hat{Q}}\sum_{l\in\hat{I}} min_{k\in I}||r_k - r_l|| \tag{4.10}$$

Here, the I and $\hat{I}$ denote the original and estimated sets of dipole index with Q and $\hat{Q}$ being the simulated and estimated number of dipoles. r_k denotes the position of the k-th simulated source while r_l denotes the position of the l-th estimated dipole. This DLE equally penalize too sparse solutions with missed sources (first member of the criterion), as well as less sparse solutions introducing spurious

dipoles far from the true sources (second member of the criterion), and this even when the whole set of true sources are indeed localized. This statistic must be read along with the rate of false discovery (FDR):

$$\mathrm{FDR} = \frac{\mathrm{FP}}{(\mathrm{TP} + \mathrm{FP})} \tag{4.11}$$

where the number of false positives FP is divided by the total number of estimated source locations, and with the rate of true positives (TPR):

$$\mathrm{TPR} = \frac{\mathrm{TP}}{(\mathrm{TP} + \mathrm{FN})} \tag{4.12}$$

where the number of true positives TP is divided by the total number of simulated sources.

To measure the impact of estimated FP on overall performance, we use the relative power of the projected FP on the scalp map with respect to the power of the full estimated scalp map, computed as:

$$\mathrm{FDP} = \frac{\mathrm{P_{FP}}}{(\mathrm{P_{FP}} + \mathrm{P_{TP}})} \tag{4.13}$$

where $\mathrm{P_{TP}}$ and $\mathrm{P_{FP}}$ are respectively true positive and false positive projection powers. This helps in measuring the relative strength of FP values with regards to the TP source power.

We emphasize that none of the proposed metric taken individually are sufficient to evaluate the quality of the localization, *e.g.*, a low DLE might not be significant if the number of sources is over-estimated and/or if the contribution of the false positives to the estimated scalp map (FDP) is high. The localization methods will be evaluated considering these criteria altogether.

4.4.4 Results

To evaluate the advantage of using our proposed ST and STF dictionaries, we compare with the results when using a spatial dictionary made of columns of the lead-field. SBR_w and SDMP_w denote the STF versions trying to explain the data on each individual wavelet support. SBR_{pca} stand for ST dictionary constructed using leadfield columns and PCA components extracted from the data. Finally SBR_t and SDMP_t stand for those fitting the lead-field atoms on the full 2 seconds temporal windows. We also provide comparisons with two standard methods of the literature: RAP-MUSIC and FOCUSS where the same lead-field with fixed orientations is considered.

Choice of the parameters

As mentioned earlier, the two evaluated sparse algorithms have user chosen parameters, and a first brief statistical analysis was made in order to asses their robustness to variations in these parameters.

The sensitivity of the SBR method to the sparsity parameter λ is analyzed by varying it between 1% and 10% of the noise energy $\mathscr{E}_n$, *i.e.*, choosing a multiplicative factor α_n in the range [0.01 0.1] such as:

$$\lambda = \alpha_n \mathscr{E}_n \tag{4.14}$$

For the different SDMP versions, the key parameter is the number of desired sources N_s. As for λ, we tested different values of N_s around its true value, used in simulation.

The situation with SBR_{pca} is different as multiple parameters must be chosen. First parameter is required for the choice of the PCA components as explained in 4.1. The second parameter stands for the choice of sparsity and is briefly explained further in this chapter.

Choice of the STF dictionary

Different dictionaries using Universal, Hysteresis and SURE thresholds were tested using different λ values. We simulate 16 linearly independent sources and add spatially colored white Gaussian noise to the electrodes thus SNR is 10dB and 3dB. In **Table** 4.1 can be seen that indeed the performance of Hysteresis, Universal and SURE dictionaries is very similar. In fact the performance of Hysteresis dictionary is somewhat in between the classical threshold therefore proving to be a strong equivalent between both SURE and Universal. Overall performance varies only slightly. In fact Universal

Table 4.1: Comparison of performance using **U**niversal, **H**ysteresis and **R**igrsure thresholds. Bold values marks the highest performance for both 10dB (blue) and 3dB (black) SNR configurations.

$\lambda = 0.02\mathscr{E}$	SBR_w U 10dB	SBR_w U 3dB	SBR_w H 10dB	SBR_w H 3dB	SBR_w R 10dB	SBR_w R 3dB
GOF	**0.96**	0.83	**0.96**	0.84	0.95	**0.85**
DLE	**4.29**	5.58	4.30	5.57	4.38	**4.88**
FDP	**0.01**	**0.02**	**0.01**	**0.02**	**0.01**	**0.02**
TP	**1.00**	0.92	**1.00**	0.90	**1.00**	**0.96**
FDR	**0.01**	0.02	**0.01**	**0.01**	**0.01**	**0.02**
Time	0.12	0.06	**0.11**	**0.05**	0.18	0.07

threshold yield less coefficients thus degraded data reconstruction quality but as we are interested here in estimated locations, we re-estimate scalp potentials using the estimated locations. Therefore the GOF values presented in the tables is computed using simulated clean scalp potentials and re-estimated ones using estimated locations. Also when compared with SURE, both Universal and Hysteresis are smaller, thus faster.

Despite the small difference in performance, further in this thesis we will use our proposed Hysteresis dictionary.

Parameter sensitivity

As shown figure 4.5, SBR_w proves to be highly robust to the choice of λ (using equation (4.14)), with no significant variations of both DLE and FDP criteria with the variation of α_n. SBR_t shows a similar behavior with λ in terms of DLE, but the FDP is higher for low λ and it is consistently outperformed by SBR_w, proving the advantage of using our wavelet-based dictionary with this MP approach. When it comes to $SDMP_t$, an under-estimation of the number of sources highly degrades the performance in terms of localization accuracy (DLE), while an over-estimation penalizes the spurious source power (FDP). Once again one can see that for highly non-stationary sources (16 sources over 4 epochs), SBR_w constantly provides better localization accuracies while keeping low the relative power of the false detections. The $SDMP_w$ performances are not presented here, because they are systematically much lower than those of the other three approaches, as it will be explained in the next subsection.

We also tested different λ_{pca} values and achieved very similar performance when α_{pca} was chosen between $[0.03 - 0.06]$. Smaller λ_{pca} degrades DLE (increases the number of estimated sources), increases FDP and FDR. Bigger λ_{pca} also degrades DLE as less sources are estimated but FDP and FDR is smaller. In tested range the results were optimal thus leading to the conclusion that also estimation using PCA dictionary is not very sensitive to the parametrization when correct number of soruces is estimated, but much more sensitive than using wavelets.

This analysis shows that main drawback when considering MP type methods such as RAP-MUSIC (91) and SDMP (140) methods is that they require the number of sources as an input. Usually this parameter is deduced from a source/noise subspace analysis based on the Akaike Information Criterion or on the Minimum Description Length criterion (106). In case of critically low SNR, synchronized sources or correlated noise, the size of the source space can be either over or under-estimated, thus considerably decreasing the performance of such methods. We want to emphasize that from our simulations it seems that SBR is much less sensitive to the choice of its λ parameter, especially when working in the wavelet domain. Indeed, by focusing on the main time-frequency components of the sources, SBR_w can easily distinguish between activities of interest and background noise.

Dictionary evaluation

In this section, we evaluate the performances of the different algorithms/dictionaries under their most favorable parameter choice (see previous subsection). More precisely, $SDMP_t$ is informed with

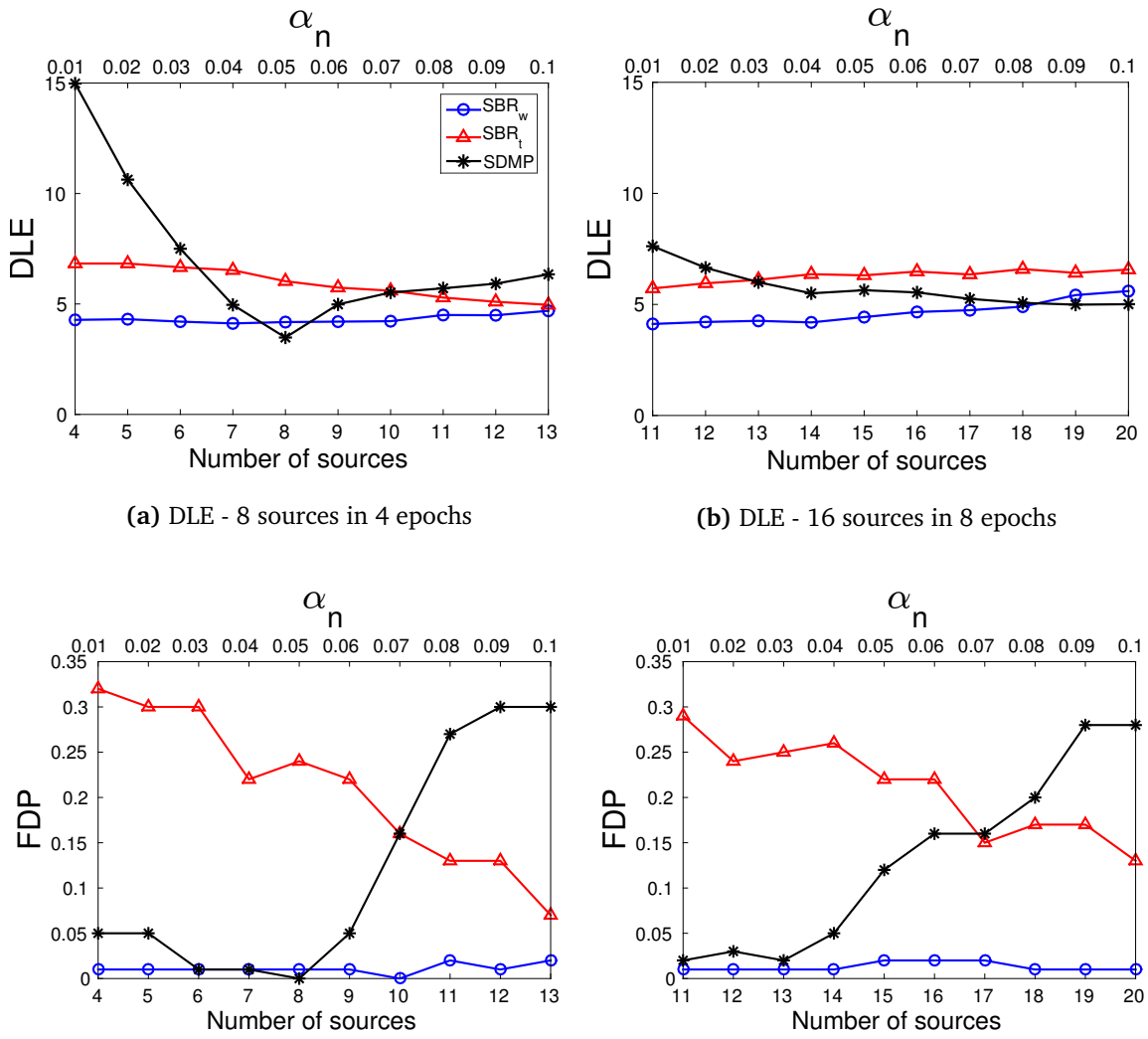

(a) DLE - 8 sources in 4 epochs

(b) DLE - 16 sources in 8 epochs

(c) FDP - 8 sources in 4 epochs

(d) FDP - 16 sources in 8 epochs

Figure 4.5: Sensitivity of SBR_w, SBR_t and $SDMP_t$ to parameter initialization, respectively to α_n fixing the λ parameter (upper axis, for SBR versions) and to the number of sources (bottom axis, for SDMP).

the total number of sources while $SDMP_w$ is informed with the true number of active sources per epoch. SBR_w is applied with $\lambda_w = 0.02\mathscr{E}_n$. For SBR_t, we have chosen a value of $\lambda = 0.05\mathscr{E}_n$, which is a compromise among the λ values yielding the best results on an extended number of source and noise configurations. Besides it should be highlighted that the RAP-MUSIC is informed correctly with the true number of sources, while FOCUSS is given the true noise standard deviation.

The metrics for the two configurations are given in tables 4.3 and 4.2. Analysing the perfor-

mance per algorithm (SBR and SDMP respectively), the benefit of using such space-time-frequency dictionary is clearly visible for the SBR approach, where the results using the SBR_w version are consistently better. The conclusions are however the opposite for the SDMP algorithm. The bad performance of $SDMP_w$ is due to the inherent strategy of this approach, which is forced to find a given number of sources for each wavelet support. Some sources can have negligible amplitudes for some support even in their respective active epoch, the informed number of sources being then *over-estimated*. More detailed analysis of the results show that SDMP indeed yields a high number of spurious sources (high FDR values), having a strong contribution on the estimated scalp map (high FDP values). Comparing the algorithms, the better performance of $SDMP_t$ over SBR_t (already emphasized in (140)) can be explained by the post-processing step in the SDMP strategy, where each source position is iteratively refined. The strengths of each dictionary are revealed when used with the appropriate MP approach. In the following, we will then be comparing the STF dictionary and the spatial dictionary through the comparison of SBR_w with $SDMP_t$.

Table 4.2: 8 sources in 4 epochs. $\alpha_{nw} = 0.01$, $\alpha_{pca} = 0.03$ and $\alpha_{nt} = 0.05$.

	TF DOMAIN		TIME DOMAIN				
10dB	SBR_w	$SDMP_w$	SBR_t	SBR_{PCA}	$SDMP_t$	FOCUSS	RMUSIC
GOF	**0.97**	0.89	0.92	0.95	**0.97**	0.96	0.94
DLE	4.23	11.99	6.05	6.48	**3.59**	6.88	6.42
FDP	0.02	0.13	0.23	0.14	**0.01**	0.04	0.03
TPR	**1.00**	**1.00**	0.99	0.99	0.99	0.97	0.92
FDR	**0.01**	0.38	0.14	0.27	**0.01**	0.06	0.07
Time	0.10	67.77	**0.03**	18.57	13.77	0.85	0.73

3dB	SBR_w	$SDMP_w$	SBR_t	SBR_{PCA}	$SDMP_t$	FOCUSS	RMUSIC
GOF	**0.90**	0.86	0.72	0.84	0.78	0.75	0.88
DLE	**5.95**	11.87	7.58	8.22	7.04	14.77	6.63
FDP	**0.01**	0.15	0.27	0.16	0.16	0.16	0.05
TPR	0.92	**1.00**	0.95	0.91	0.88	0.62	0.91
FDR	**0.01**	0.41	0.17	0.22	0.09	0.22	0.08
Time	**0.03**	81.47	**0.03**	18.41	13.63	0.75	0.73

As stated before, ST dictionary using PCA is highly sensitive to the estimation of source space. When underestimated, not all source information will be captured in the dictionary. In the contrary,

overestimation leads to the noise components and thus, yield spurious noise dipoles at localization. This problem is not present for wavelet dictionary where wavelet threshold somewhat *automatically* estimates the noise power, thus estimating the source and noise space is not a prerequisite for this approach.

In general when compared to other methods (see **Table** 4.2), SBR_{PCA} proves to be competitive to others. Although increased DLE indicates spurious sources that, in fact, are with relatively high amplitudes as FDP shows. It is also noteworthy that such dictionary has huge data size (several ≈5.41Gb for 128 sensors, 645 dipoles, 8 sources and 512 time samples) therefore computation time is significantly increased.

In case of highly non-stationary data with high number of sources, *i.e.*, 16 sources on 8 epochs, the data size of spatio-temporal dictionary $\mathbf{H}_{pca}$ used for SBR_{PCA} grows exponentially with the number of sources. In our experience, we observed that using such simulation set-up, SBR_{PCA} is very time and memory consuming. As can be seen in **Table** 4.2, the results using $\mathbf{H}_{pca}$ are similar to others, but with relatively high FDR. By taking into account the computational drawback of the PCA dictionary, we will not further provide results using these temporal atoms.

As it can be seen in **Table** 4.3, SBR_w approach outperforms SDMP_t. This is especially the case when the SNR is low (3dB). Because of the thresholding, the wavelet dictionary favors the most significant temporal elements and help in distinguishing between source and noise space. SBR_w yields TDR values very close to 1, meaning that all the sources are indeed retrieved, while the FDR and the FDP values remain of the order of 0.01. Under ideal parametrization (correct N_s) SDMP_t becomes more efficient than SBR_w as the number of sources is reduced and their stationarity increases, as well as when the SNR increases. For 8 sources over 4 epochs with a SNR of $10dB$, both methods are competing with a noticeable advantage for SDMP_t when looking to the DLE. This trend is further confirmed over all the simulated configurations with less sources and epochs (*i.e.*, with more stationary and less sources, not shown here). Still, one must recall that SDMP_t performances depend on the right choice of the N_s parameter.

From an implementation point of view, the computation burden for each method show that SDMP is the most consuming method, being between 100 to 1000 times slower than SBR depending on the configurations and the dictionary used. SBR_w proves to be very robust and fast, allowing to estimate the cortical map for 2 seconds of data within about 100ms.

The standard methods proposed in the literature based on minimum norm estimate such as FOCUSS, proves to be less accurate when facing highly non-stationary data especially for low SNR.

This algorithm further in this thesis will no longer be used. RAP-MUSIC however shows strong robustness over all the configurations.

Table 4.3: 16 sources in 8 epochs. $\alpha_{nw} = 0.01$, α_{nt} is 0.05.

	TF DOMAIN		TIME DOMAIN			
10dB	SBR_w	$SDMP_w$	SBR_t	$SDMP_t$	FOCUSS	RMUSIC
GOF	**0.96**	0.92	0.91	0.92	0.94	0.95
DLE	**4.37**	8.70	6.49	5.62	7.89	4.49
FDP	**0.01**	0.19	0.27	0.17	0.06	**0.01**
TPR	**1.00**	**1.00**	0.97	0.95	0.93	0.97
FDR	**0.01**	0.23	0.09	0.05	0.09	0.02
Time	0.19	31.25	**0.05**	26.03	0.80	2.39
3dB	SBR_w	$SDMP_w$	SBR_t	$SDMP_t$	FOCUSS	RMUSIC
GOF	**0.86**	0.46	0.57	0.56	0.65	0.81
DLE	**4.87**	11.17	10.25	8.22	19.13	4.92
FDP	**0.01**	0.19	0.30	0.34	0.25	0.05
TPR	0.95	**1.00**	0.72	0.85	0.46	0.96
FDR	**0.01**	0.45	0.13	0.13	0.35	0.03
Time	0.05	95.01	**0.04**	32.04	0.76	2.65

4.4.5 Discussion

We compare our algorithms using realistic simulation setup with three well-known inverse problem algorithms, namely RAP-MUSIC, FOCUSS and recently proposed SDMP. Among classical approaches, RAP-MUSIC (91) provides the best accuracies, while FOCUSS needs longer time windows to provide accurate performances. As emphasized in (140), SDMP applied with a spatial dictionary is efficient when the sources are rather stationary, and if the expected number of sources is known. However it fails in decomposing the data on the proposed STF dictionary, as it requires the number of sources as an input. Sufficiently large time windows with significant activations of these sources is then needed, which is not the case when considering short time supports. Our approach is competitive with all for all noise noise levels, but we outperform others when the number of sources is rather big and SNR is low. Besides the sparse approximation using spatio-temporal dictionaries proved to be very fast for

large data and highly robust to the choice of the parameters.

This contributes to the idea that no universal localization method can cover the full spectrum of applications. Our proposed STF dictionary combined with the SBR strategy might be favored when trying to localize highly transient phenomena like epileptic spikes or cognitive evoked potential. The next section aims to evaluate the performances of the proposed methods on real data, issued from EEG recordings of an epileptic patient.

4.5 Real data validation

4.5.1 Set-up

We will now perform the localization on the same data that those exploited in the chapter 3.3, with the same pre-processing steps (*i.e.*, 50Hz notch-filtered or band-passed). For the comfort of the reader, we give again the 64 channel time-courses of these real data within a selected 6 seconds window, for the notched (**Figure** 4.6) as well as the band-passed data (**Figure** 4.7). This window contains the same epileptic activity as those analyzed in the last chapter. In particular, we will focus on a sub-window of length 1.5 seconds (from 3.7 to 5.2s), containing interesting spiking activities as visually selected by the neurologists (especially within the channels PO3 to FC5 as outlined by the blue square in the figure). We apply SBR_w, SBR_t, SDMP_t as well as RAP-MUSIC on this data window.

In the same way as done in the chapter 3.3, we extract the surface meshes from the MRI and place 64 electrodes on the scalp surface, following the standard 10-20 system used for recording the data. Then each extracted surface is visually validated by aligning it on the corresponding segmented MRI structure (see **Figure** 4.8). We use cortical surface discretized in around $\sim$4000 points, and we define the dipole position just below the center point of the mesh triangle (for BEM computation reasons). In the same way as done in the simulations, we assume that the orientation of each dipole is fixed and normal to the cortical surface (mesh triangle). The computation of the BEM forward model based on three surfaces is carried out in the same manner as in the simulation section, by use of the isolated skull approach implemented in the Helsinki toolbox (120). The skull conductivity was classically assumed as 1/20 of the skin and brain conductivity.

4.5.2 Results

As pointed out in the methodological part, all of the algorithms need to be initialized or parametrized. For the SBR algorithm, the regularization parameter λ has to be given. As done in the simulation

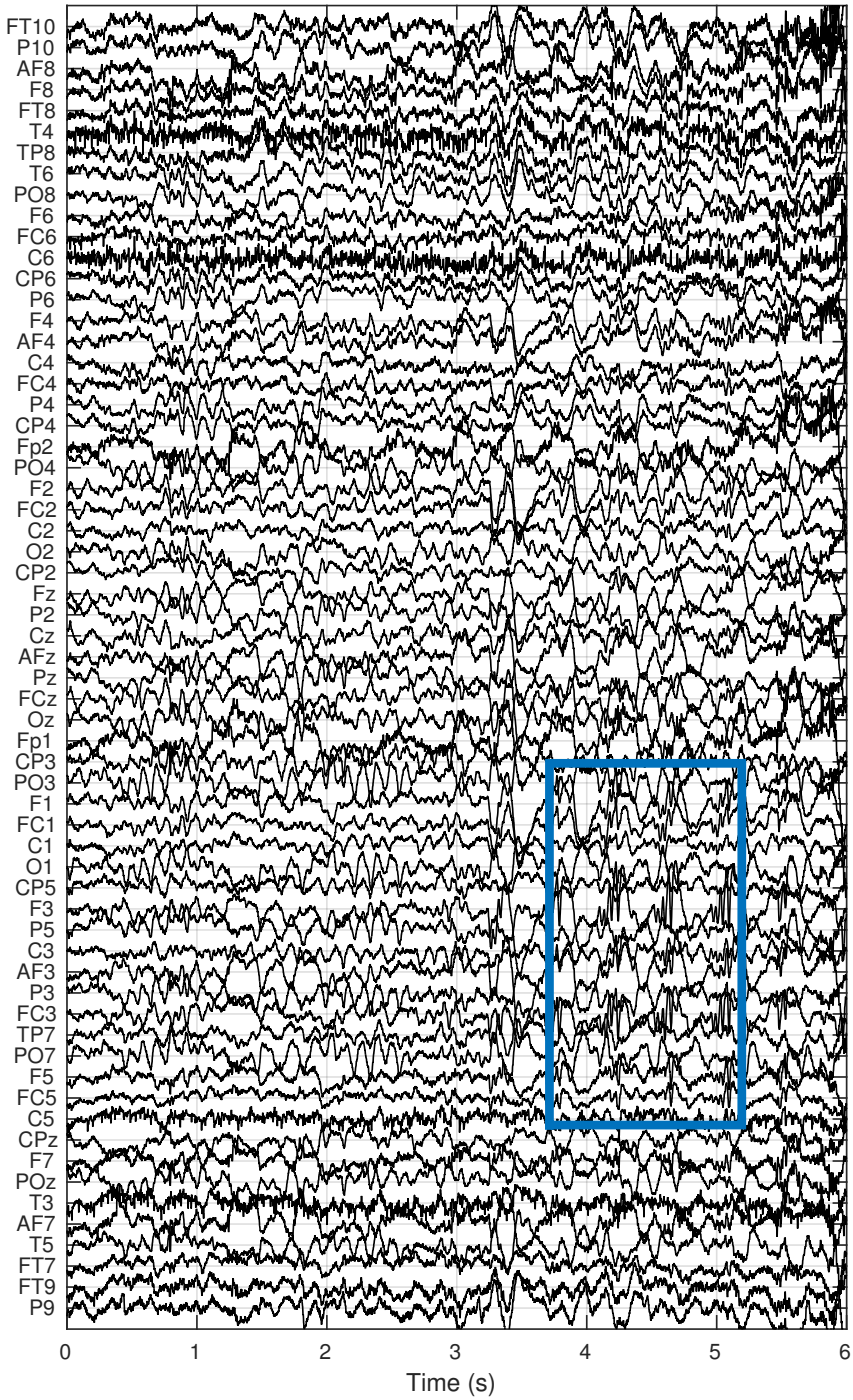

Figure 4.6: Notch-filtered data window of 6 seconds and chosen (square from 3.7s-5.2s) sub-window of 2 seconds representing the area of interest.

part, we compute the noise energy from the wavelet denoised data, such that:

$$\mathscr{E} = ||\mathbf{V}_w||_F - ||\mathbf{V}_{denw}||_F$$

, where $||\mathbf{V}_w||_F$ is the Frobenius norm of measured data in wavelet domain and $||\mathbf{V}_{denw}||_F$ the Frobenius norm of denoised data using Universal wavelet threshold. As already discussed in this chapter, λ can be set as a fraction α_n of this noise energy estimates. We perform several trials by varying α_n in the range 0.05 to 0.01, as done on the simulated data. Finally, we assume the following α_n values, yielding the best visual results, *i.e.*, limiting the number of estimated sources due to noise components while still identifying the strong ones: 0.010 for band-pass(8-48Hz) filtered data and 0.015 for notch-filtered data.

In order to inform both SDMP and RAP-MUSIC, the size of the source space must be estimated. This is a particularly arduous task when facing such real noisy data, and on which classic routine like the MDL procedure tend to over-estimates the number of significant components. Therefore the number of candidate sources still remains as a user parameter. Although one might choose the number of sources *a priori* by adopting an empirical rule, choosing those biggest eigenvalues that explain at least 95% (2.35, 2.36) of the EEG data(**Figures** 4.6,4.7). The estimated size of the source space is 8 for the notch-filtered data and 9 for the band-passed version. From medical priors, the number of underlying sources we are looking for goes from one to two, one active epileptic source in the left hemisphere and possibly one in the right hemisphere. With such informed size, these allegedly most significant sources will indeed be scanned by the SDMP and RAP-MUSIC procedures, while limiting the number of estimated noisy components. We do not restrict further the number of components in order to let these algorithms reveal other possible source locations.

In this chapter, the localization results are given as red points super-imposed on a representation of the cortical surface shown in **Figure** 4.9. On the right hand of the same figure, we also provide the positions of the scalp electrodes as labels super-imposed on the mesh of the head. In particular, it roughly provides the position of the electrodes F3 and FC3 under which, according to the analysis done by the experts, the main epileptic activities to be localized are supposed to lie.

Each method is applied on the full 1.5 seconds data window, and we extract the localization results of each methods within 6 contiguous sub-windows of $0.25s$, for the notched (**Figure** 4.10) as well as the band-passed data (**Figure** 4.11). The results are displayed for each methods using the same normalized color scale for all the sub-windows. Stronger dipoles are bigger in size and are red while the weaker dipoles are smaller and tend to be white. In the upper part of each figure of results are given time-courses of the channels as super-imposed black curves, temporally scaled with the

different localization pictures, bringing an overall vision of the temporal activities that have been localized window by window.

Results shows that pre-processing step (applied notch or band-pass filter) yields different results. We first consider the raw data where only the notch filter is applied (**Figure** 4.10). For all the 4 tested methods, the results are consistent and yield localizations mostly in the left hemisphere in the expected upper left area under electrodes F3 and FC3 corresponding to the left part of the frontal lobe. We remind that SBR_t, SDMP_t as well as RAP-MUSIC have to estimate a time-course for each source for the full data length of 1.5s, whereas the SBR_w works on local wavelet time support and is more adapted to handle non-stationary events. This is here nicely illustrated by (i) the vanishing of all activities in the 5^{th} window (1 to 1.25s) where the time-courses indeed do not contain strong activities, and also by (ii) the apparition of a strong sources in the upper left of the right hemisphere within the second, third and last windows, while SBR_t and SDMP_t also localize a source of hardly noticeable amplitude within these windows, and RAP-MUSIC totally miss it. it is noteworthy that the neurologists have indeed identified the apparition of slow and highly transient epileptic activities in channels $FC4$ and $F4$ within these time windows (see 4.6). According to their expertise, it is very likely that this identification indicate a location directly or indirectly connected with the source of the left hemisphere.

Taking benefit of the *priors* given by the medical expertise, we consider to band-pass the data and to carry out the localizations in the frequency bands of interest between 8 and 48Hz, as explained in the chapter 3. The results are shown in **Figure** 4.11. The SBR optimization based on the STF dictionary brings very sparse results, and is very consistent from a window to another, confirming the robustness of the approach. The estimated locations are still consistent with the positions validated by the neurologists, but with enhanced degree of spatial sparsity. In addition, the 2^{nd} and 5^{th} windows remain both silent, as indeed no evident spiking activity can be observed in the corresponding temporal activities. It emphasizes the ability of the method to separate the significant physiological activities from noisy components.

The results produced by the three other methods are very similar, also identifying the presence of a source in the suspected region. However, all these methods seem to produce spurious activation in the lower part of the brain. These localizations cannot be validated by the experts, and might be produced due to the presence of noise/artifact components.

On the other hand, these results highlights the performance limitation of the SBR_w approach (space-time-frequency dictionary based on wavelet coefficients). On these band-passed data, a

strong spiking activity in the window 1.25-1.5s is revealed by the localization procedure, this activity being indeed clearly visible on the data time-courses. This source has been missed by the SBR_w method when applied on the notched data (see **Figure** 4.10). After analyzing the algorithm outcomes, we conclude that particularly this spiking activity has been suppresed by the presence of the strong sources localized in the right hemisphere within this particular sub-window (and later eliminated by the band-pass filtering). In fact, SBR_w localizes the most energetic signals allowed by the STF dictionary. This means that indeed smaller sources (with less energy) but more important can be missed. To avoid such drawback one might analize the signals and keep those atoms corresponding for the sources of interest. Inversely, the other methods bring an under-estimation of this right hemisphere activity while still localizing the left one. We have then to be very careful when recommending one or the other method, each having their advantages and drawbacks. No universal approach exist yet, and cross-checking the output given by several algorithms seems still the best way to provide a reliable source localization estimate.

4.5.3 Discussion

As for the simulated case, we evaluate different optimization strategies for choosing the relevant atoms from the dictionary against classical approaches such as RAP-MUSIC. The performance of FOCUSS is not discussed here because the simulation results were significantly worse that the others and we tend to compare the matching pursuit type methods.

The main difference with respect to the simulation is the presence of strong background activity, *i.e.*, sources not relevant to the epilepsy. These sources with relatively high signal energy are not eliminated by wavelet denoising so supplementary preprocessing steps are needed like band pass filtering. Using this preprocessing, the results obtained on the real epileptic EEG data confirm that the SBR_w approach preserves its properties (sparsity and correct localization), as the expected position of the epileptic sources are indeed consistently identified. The produced localizations are very sparse spatially as well as temporally with some estimated time windows remaining silent when no significant source is active.

On the other hand, the increased sparsity comes with a price when applied on the raw data. In particular, the SBR_w method clearly identifies a strong source in the opposite hemisphere (with respect to the band-passed filtered data), that was missed or underestimated by the other algorithms, while missing the spike in the correct location. According to medical expertise, the generator in the right hemisphere is not an artefact, but a real secondary epileptic source (for this patient, the epileptic activity was initiated in the left hemisphere but spread rapidly to the opposite one). This illustrates

the difficulties in real situations, when one must either compare several localization methods or to vary the user parameters (λ in the SBR case) in order to obtain a valid solution.

4.6 Conclusion

It is clear that no universal and completely autonomous approach has been proposed to date for solving the EEG inverse problem, so the panel of available methods in the literature is extremely large and one can chose a particular method likely to provide the best performance for a given application. The main contribution of this chapter is a formulation of this problem within a sparse optimization framework and using a data-driven space-time-frequency dictionary, where the atoms are constructed using a realistic lead-field model for the space component and a thresholded wavelet decomposition for the time-frequency one. We evaluate different optimization strategies for choosing the relevant atoms from the dictionary against classical approaches such as RAP-MUSIC and FOCUSS. In particular, among these optimization strategies, SBR_w proves to be very efficient in decomposing the data on such atoms, with limited computational cost, high robustness to noise and to user chosen parameters, while providing enhanced localization results when the non-stationarity of the sources increases. These advantages can be explained by the details of this algorithm: while most of the algorithms estimate the source time-courses over the whole data window, this approach analyse the data wavelet support by wavelet support, and is able to focus on transient activities that might be underestimated by the other methods. The denoising implicitly carried out by the wavelet atom extraction prevents the algorithm to produce spurious sources due to noisy components.

We also shed light on a sensitive aspect shared by all algorithms, that is their parametrization. Indeed, some algorithms, *e.g.*, SDMP or RAP-MUSIC, require the estimation of the size of the source space (*i.e.*, roughly the number of independent underlying source components). If theoretical criteria exists for producing such estimates, they seem to be unfortunately based on too simplistic assumption (*e.g.*, noise modelling as white and Gaussian), and do not provide relevant results from our experiments. Methods based on mixed norm regularization does not require such information, but still need to fix a trading parameter between adequation to the data and respect of the regularization criteria (although the SBR_w approach seems to be less sensitive to variations of this parameter). From our experiments on real data, these parametrization issues still remains unresolved, and are for now left as user parameters.

Several future research directions can be imagined. First, one of the drawbacks of the used methods is the fact that the orientations of candidate dipoles are fixed and that their locations are limited

to the cortex. The model can be extended to allow free orientation and deep brain sources. In this case, other optimization scheme must be chosen based on a block sparsity estimation, *i.e.*, methods that are able to choose the best atom from the dictionary and estimate the orientation. It also is interesting to notice (see figure 4.2) that the degree of correlation between dictionary atoms (lead-field columns) is not spatially homogeneous. Indeed, for inner skull surfaces where the cortical layer has a small curvature and thus the neighbouring dipoles have the same or very close orientations, the correlation are high. On the the other hand, in the areas of high cortical curvature one might notice significantly lower correlation values whereas high correlation is still present at the gyral crowns. A possible way to avoid such highly correlated atoms is to adaptively modify the mesh and allow coarser grid in places where the correlation is high. In practice, this would boil down to a reduced spatial dictionary corresponding to a subsampled lead-field matrix.

Using a space-time-frequency dictionary might also open other interesting perspectives, as using other techniques (instead of simple band pass-filtering followed by wavelet denoising) for selecting physiologically relevant atoms (for example, selecting the atoms based on some adapted thresholds tuned according to *a priori* user knowledge, such as the frequency content for epileptic high-frequency activities (82)).

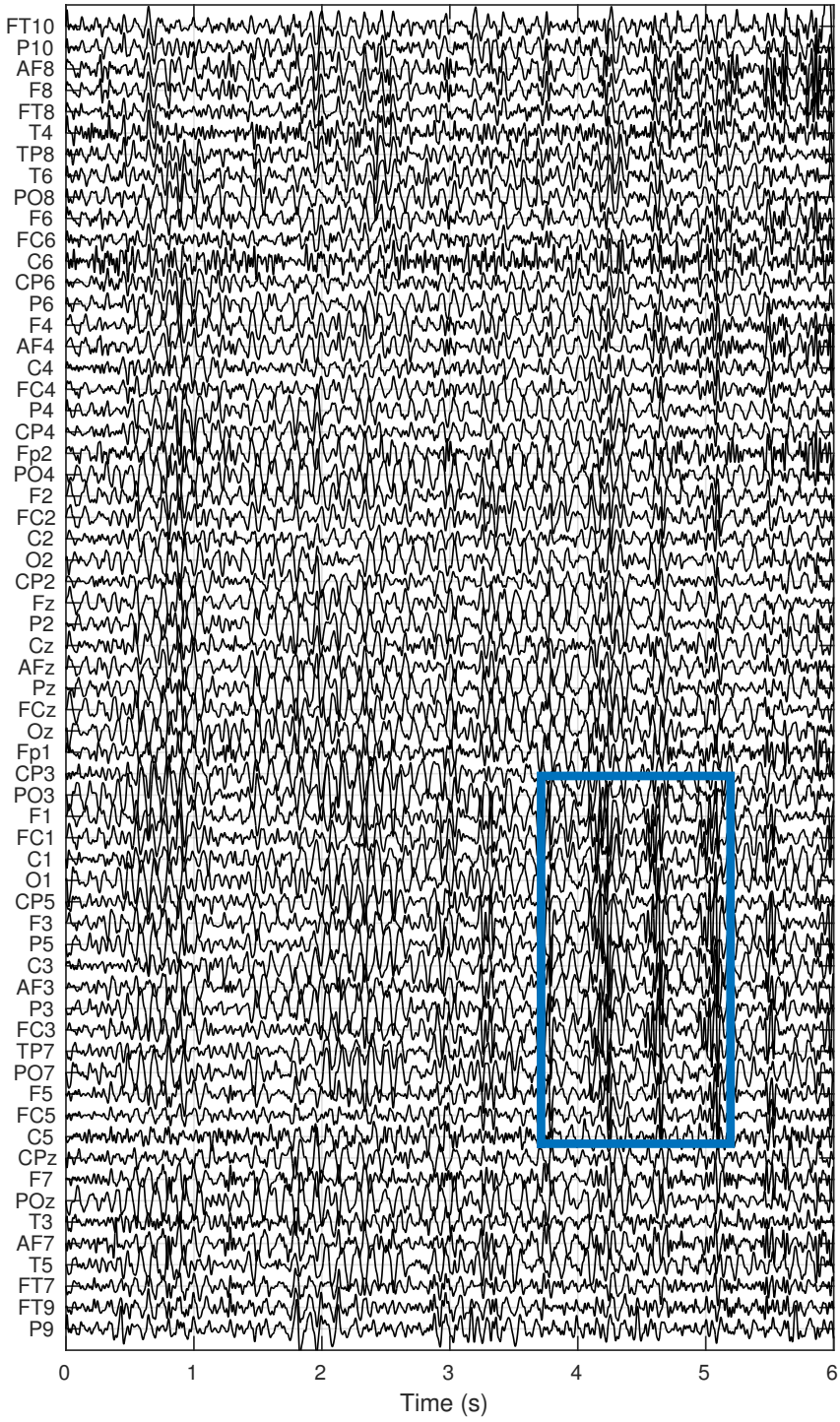

Figure 4.7: Band-pass filtered data window of 6 seconds and chosen (square from 3.7s-5.2s) sub-window of 2 seconds representing the area of interest.

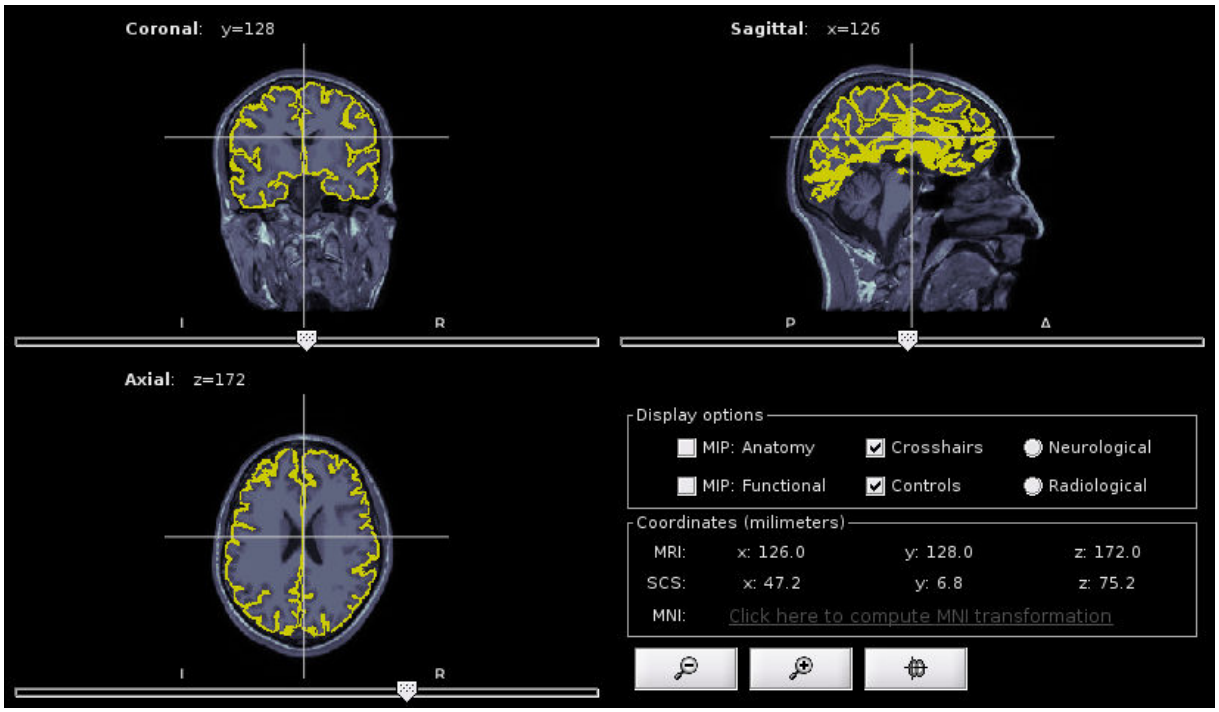

Figure 4.8: Aligned cortical surface mesh in the MRI. Screenshot from BRAINSTORM toolbox (123).

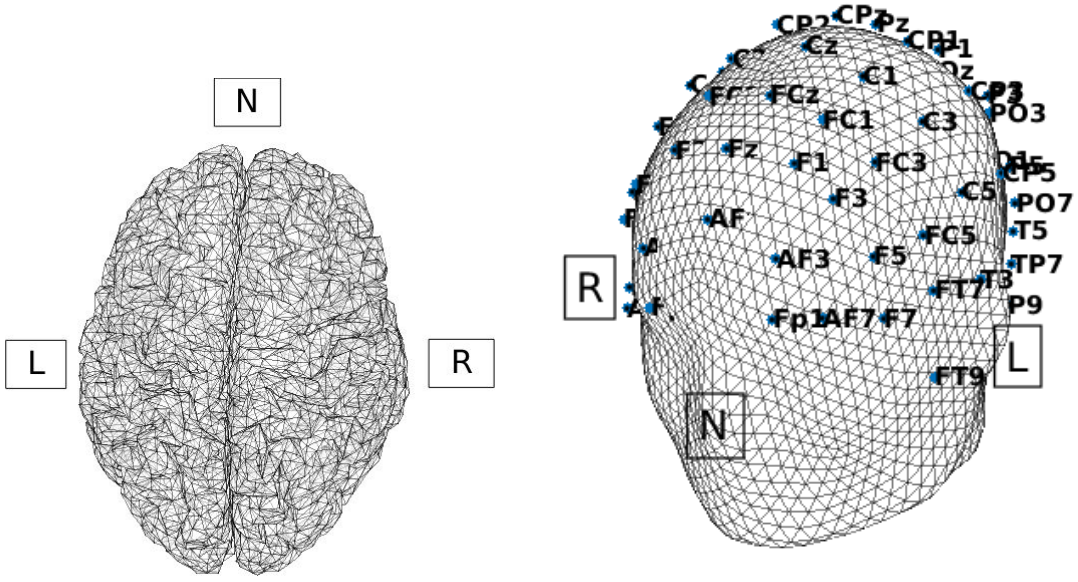

Figure 4.9: Cortical surface with following directions: **L**eft,**R**ight, **N**ose.

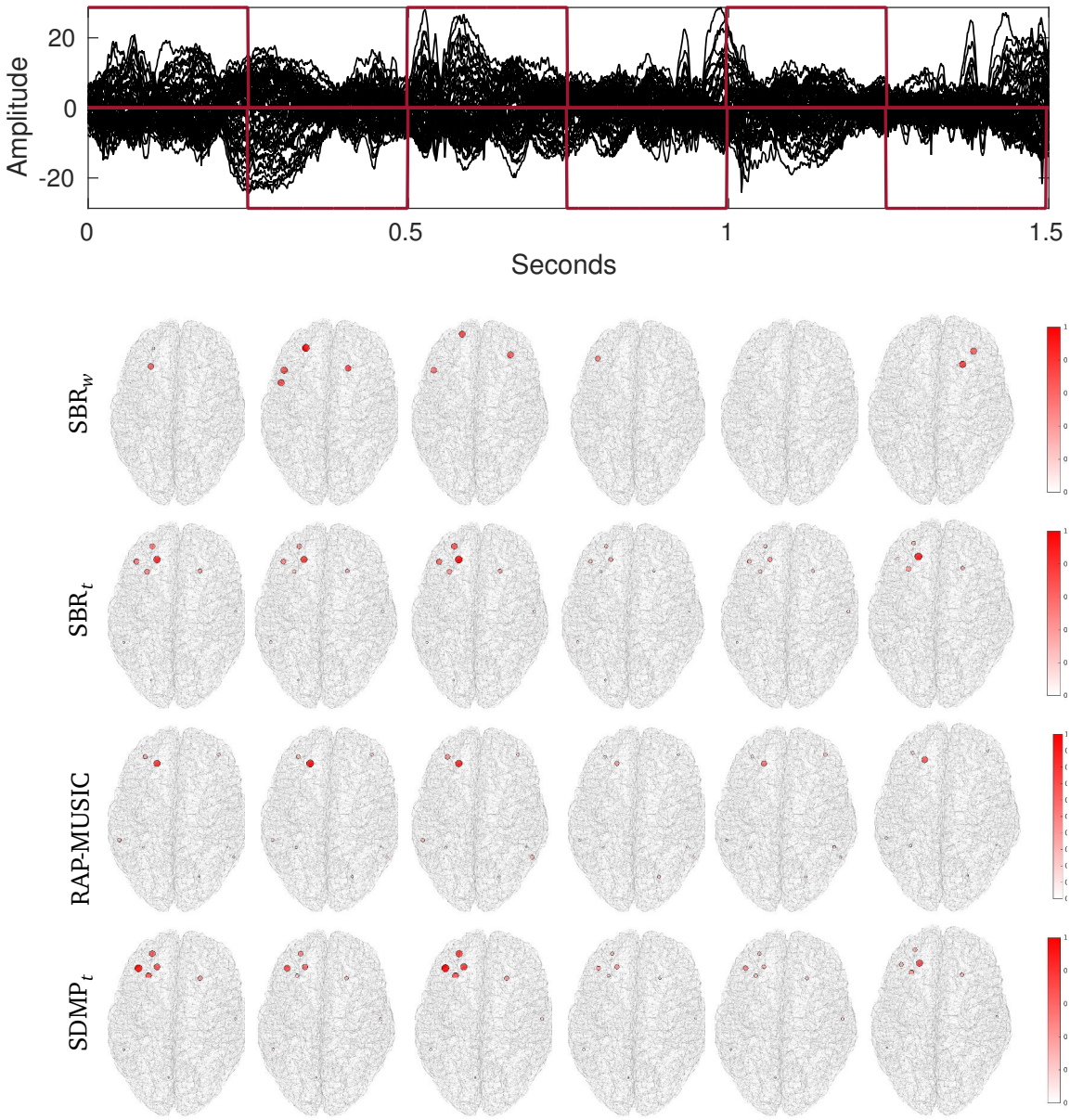

Figure 4.10: Estimated spatial activity of notch-filtered data splitted in equal windows of 0.25 seconds each. Amplitudes represents normalized dipole power. For visualization purposes color values are scaled between 0 and 1.

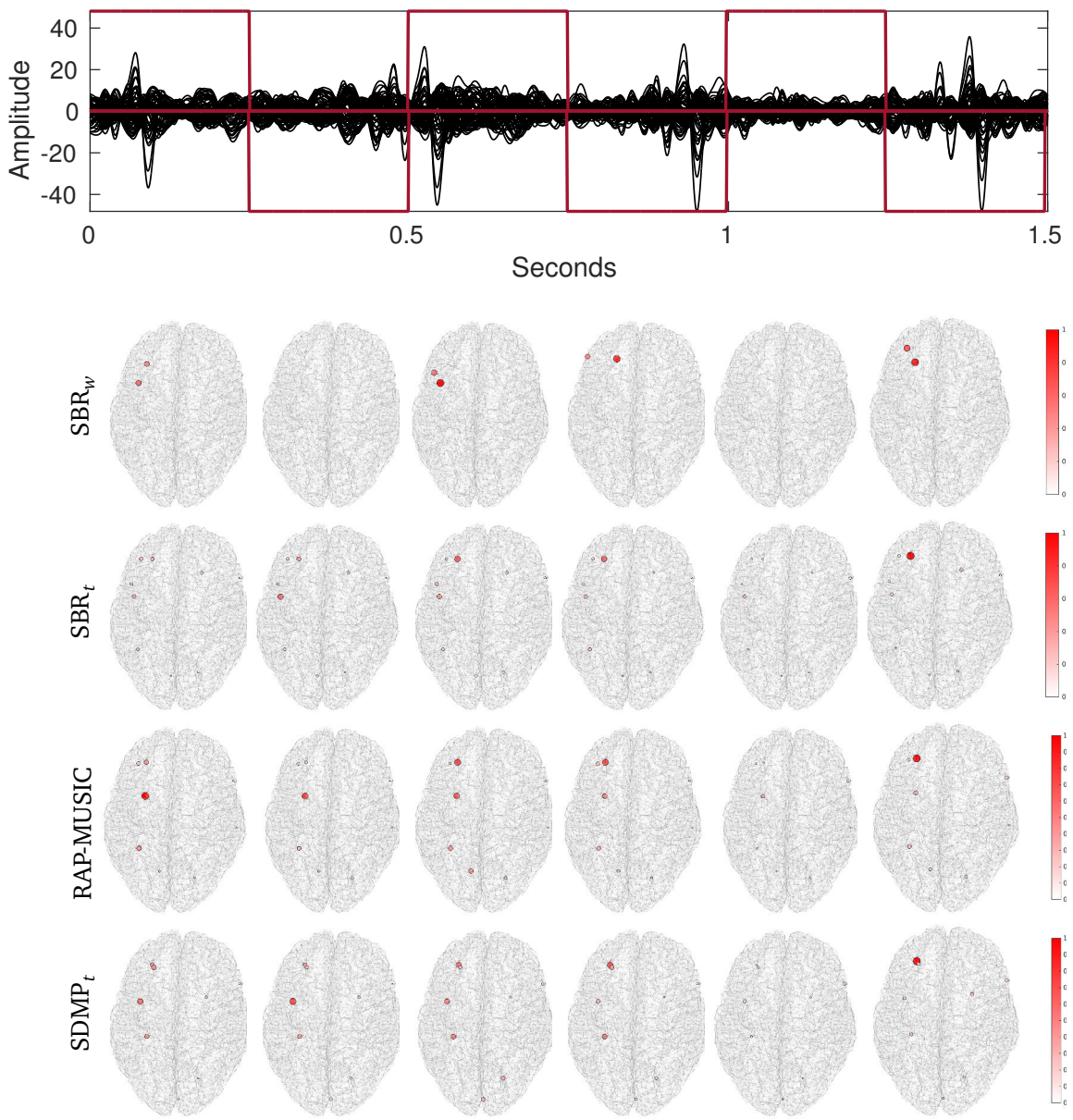

Figure 4.11: Estimated spatial activity of band-pass filtered data splitted in equal windows of 0.25 seconds each. Amplitudes represents normalized dipole power. For visualization purposes color values are scaled between 0 and 1.

Conclusion and Perspectives

Summary and Main Contributions

Functional specialization of different cortical areas is now a well established field of knowledge. Nevertheless, most cerebral functions are distributed over several areas organized in networks and, on the other hand, some areas might participate in several networks. This complex organization appears both in normal and pathological brain functioning. The production of dynamic activation maps of the cortex from non-invasive measurements, *i.e.*, localize the network nodes and detect the dynamics of their activations, is still an active topic of research. This thesis deals with the estimation of cortical sources from two main perspectives. First one being the development of cortical imaging methods based on the EEG measurements and on simple geometric hypothesis alone (chapter 3), the second one exploring dictionary-based methods using realistic anatomical models and sparse Matching Pursuit algorithms (chapter 4).

One of the first cortical imaging method is the Hjorth Laplacian montage (68), which provides a discrete image of the underlying sources from the second spatial derivatives of the surface potential. This principle has been extended to the estimation of continuous activation maps, where an interpolation of the discrete measurements on the head surface is carried out before its derivation (8, 32). Inspired by such interpolation scheme, we interpolate the surface measurements using Radial Basis Functions modelling the projection of the cortical sources on the scalp. These basis functions are built using two different geometrical approximations of the head - planar and spherical - producing physiologically plausible (dipolar) patterns on the scalp surface. Considering a full-rank propagation matrix (i.e, equal number of sources and electrodes), the interpolation weights represent the estimated strength of the sources, producing discrete scalp maps. Using this methodology, we put forward obvious links between the surface laplacians (SL) and the most usual electrical source imaging (ESI) methods based on Minimum Norm Estimation, which often appear as two disconnected fields of research in the literature. The resulting estimator is called Dipolar Cortical Mapping (DCM)

and is compared to recent SL methods and to a basic minimum norm estimate on simulated signals. While an full rank ESI approach based on an accurate BEM model gives better results for high SNR configuration, our DCM approach is less sensitive to the additive noise and yields satisfactory results up to a 10dB SNR ratio. It competes with more complex SL approach while keeping very low the algorithmic complexity, and requiring very few and easily available anatomical information.

If in chapter 3 we estimate sources having fixed positions beneath the electrodes (and thus the same number of sources and electrodes), in chapter 4, we relax these fixed location constraints (and thus the full-rank hypothesis) and dipole candidates are placed all over the cortical surface. Unlike the DCM, an under-determined inverse problem is now to be solved, as now all possible positions on the cortex need to be considered. This approach implies that we must use a complete lead-field matrix, computed through a forward modelling approach. On the other hand, unlike in classical minimum norm ESI, our aim is still to explain the measured signals (scalp map) with a reduced number of sources, in principle much smaller than the number of electrodes. Following the physiological assumption that few cortical sources are simultaneously activated, we take benefit of the matching pursuit framework for the production of sparse solutions. Such approaches aim to explain the measured data as a decomposition on a highly correlated dictionary constructed from the columns of the lead-field matrix and they have proved to be efficient for EEG source imaging (56, 72, 140). While the decomposition is usually carried out in the spatial domain by selecting the dipole projections which best fit the data, we enforce the regularization by using space-time/frequency (STF) dictionaries. We use two types of dictionaries extracting the temporal characteristics directly from the data, either using PCA decomposition or wavelets. Using the PCA components, the algorithms are able to identify stationary neural generators. The main drawback is of computational order, being far too memory demanding when the number of sources increases. The wavelet dictionary brings high performance for non-stationary data regardless of the number of sources. While most of the methods are very sensitive to their initial conditioning, which is often related to a pre-estimation of the number of sources, the SBR optimization scheme combined with the proposed STF dictionary is robust to its parametrization. We have illustrated the applicative potential of the method by considering the data of an epileptic patient, estimating the localization of spike generators with very local spatial and temporal nature. The results are concordant with the expertise of neurologists and further validated by the surgical outcome.

Discussion and perspectives

One of the key aspects when it comes to source localization is the head modeling at the basis of the construction of the forward model. Numerous works in the past ten years tend to establish more and more sophisticated models thanks to the growing available computational power. However such modelling involves sensitive pre-requisites, as the estimation of conductivity parameters and precise segmentation of the head tissues, such procedure being prone to uncertainties and approximations. As pointed out by recent publications (16, 26), these efforts might not be relevant when quantifying the localization precision. Such conclusion might also be drawn from the results of this thesis, where rough planar and spherical approximations of the head used in the DCM approach are shown to compete with BEM MNE method and sophisticated SL approaches, with drastically reduced computation cost. The question which naturally arises is where to put the cursor when it comes to the construction of a forward model. Similarly to the reduction of the temporal dictionary provided in this thesis, we might think of a reduction of the spatial dictionary by adapting the size of the lead-field to the expected localization precision, this precision being irreducible and dependent of the uncertainties inherent to the forward model, and to the imprecision of the data due to the presence of noise.

Applied on such electro-physiological brain measurements, the localization of activities lying within particular time-frequency bands is of particular interest. In this thesis we have illustrated its ability to provide accurate localization of epileptic generators, such activities showing well defined time-frequency characteristics. Using alternative learning techniques for selecting physiologically relevant atoms, it is possible to further adapt the method to a given application. One might think of cognitive applications, where the localization of the generators of evoked-potential is required for the identification of the brain structures responsible for a given cognitive task (136). These evoked activities being highly reproducible, constructing a temporal dictionary formed by atoms learned on such data brings a promising way to built a dedicated and robust localization tool.

Finally, the sparse philosophy we adopt all along this work has been developed on purpose for treating a key neuroscientific question not tackled within the framework of this thesis: the identification of functional or pathological brain networks at local or large scale, in which distant brain structures cooperate and who are widely believed to be at the root of the normal or abnormal brain mechanisms. By summing up the recorded measurements using few point sources, each standing for the mean activation of the brain structure they are lying in, we greatly simplify the analysis of these underlying networks, where each identified point source can be considered as a node of a graph of

connected structures. We profoundly believe that the study of the source relationships in the reconstructed source space using Source Imaging methods is at the basis of a better understanding of the human brain machinery (85).

Bibliography

[1] ABOITIZ, F., SCHEIBEL, A. B., FISHER, R. S. et ZAIDEL, E. (1992). Fiber composition of the human corpus callosum. *Brain Research*, 598(1-2):143–153. 17

[2] AMINGHAFARI, M., CHEZE, N. et POGGI, J.-M. (2006). Multivariate denoising using wavelets and principal component analysis. *Computational Statistics & Data Analysis*, 50(9):2381–2398. 92

[3] and others ANATOLE, L AND LOTTE, FABIEN AND REILLY, RICHARD B AND LEEB, ROBERT AND HIROSE, MICHITAKA AND SLATER, M. (2008). Brain-computer interfaces, virtual reality, and videogames. *Computer*, (10):66–72. 33

[4] ANSARI ASL, K. (2005). *Mesure De Couplage Statistique Entre Signaux Eeg : Application a L'Evaluation Quantitative Des Relations Fonctionnelles Entre Structures Cerebrales En Epilepsie*. Thèse de doctorat. 31

[5] ANTONIADIS, A., BIGOT, J. et SAPATINAS, T. (2001). Wavelet Estimators in Nonparametric Regression : A Comparative Simulation Study. *Insight*, 6(6):1–83. 92

[6] ARFKEN, G. B. (1999). Mathematical Methods for Physicists, 4th ed. *American Journal of Physics*, 67(2):165. 45

[7] BABILONI, F., BABILONI, C., CARDUCCI, F., FATTORINI, L., ONORATI, P. et URBANO, a. (1996). Spline Laplacian estimate of EEG potentials over a realistic magnetic resonance-constructed scalp surface model. *Electroencephalography and Clinical Neurophysiology*, 98(4):363–373. 49, 50, 51, 67

[8] BABILONI, F., BABILONI, C., FATTORINI, L., CARDUCCI, F., ONORATI, P. et URBANO, a. (1995). Performances of surface Laplacian estimators: A study of simulated and real scalp potential distributions. *Brain Topography*, 8(1):35–45. 48, 50, 51, 119

[9] BABILONI, F., CINCOTTI, F., MARCIANI, M., SALINARI, S., ASTOLFI, L., TOCCI, a., ALOISE, F., DE VICO FALLANI, F., BUFALARI, S. et MATTIA, D. (2007). The estimation of cortical activity for brain-computer interface: applications in a domotic context. *Computational intelligence and neuroscience*, 2007:91651. 33

[10] BAILEY, D.L; TOWNSEND, D.W; FALKE, P. (2005). *Positron Emission Tomography: Basic Sciences*. 30

[11] BAILLET, S., MOSHER, J. et LEAHY, R. (2001). Electromagnetic brain mapping. *IEEE Signal Processing Magazine*, 18(6):14–30. 11, 13, 57, 67

[12] BECKER, H., ALBERA, L., COMON, P., GRIBONVAL, R., WENDLING, F. et MERLET, I. (2014). A performance study of various brain source imaging approaches. *In ICASSP, IEEE International Conference on Acoustics, Speech and Signal Processing - Proceedings*, pages 5869–5873. IEEE. 100

[13] BECKMANN, C. F., SMITH, S. M., HUETTEL, S. A., SONG, A. W. et MCCARTHY, G. (2004). *Functional Magnetic Resonance Imaging*, volume 23. Sinauer Associates Sunderland. 30

[14] BERG, P. et SCHERG, M. (1994). A fast method for forward computation of multiple-shell spherical head models. *Electroencephalography and Clinical Neurophysiology*, 90(1):58–64. 41

[15] BERGER, H. (1929). Uber das electrenkephalogramm des menschen. *Archiv für Psychiatrie und Nervenkrankheiten*, 87:527–570. 25

[16] BIROT, G., SPINELLI, L., VULLIÉMOZ, S., MÉGEVAND, P., BRUNET, D., SEECK, M. et MICHEL, C. M. (2014). Head model and electrical source imaging: a study of 38 epileptic patients. *NeuroImage: Clinical*, 5:77–83. 121

[17] BLACK, a. H. (1971). The direct control of neural processes by reward and punishment. *American Scientist*, 59(2):236–245. 27

[18] BLUMENSATH, T. et DAVIES, M. E. (2007). On the Difference Between Orthogonal Matching Pursuit and Orthogonal Least Squares. *Ieee*, 44(0):1–3. 63

[19] BONNET, L., LOTTE, F. et LÉCUYER, A. (2013). Two brains, one game: Design and evaluation of a multiuser bci video game based on motor imagery. *IEEE Transactions on Computational Intelligence and AI in Games*, 5(2):185–198. 33

[20] BRAZIER, M. A. B. (1962). A History of the Electrical Activity of the Brain. *Proceedings of the Royal Society of Medicine*, 55(4):338. 31

[21] BRUYANT, P. P. (2002). Analytic and Iterative Reconstruction Algorithms in SPECT. *J Nucl Med*, 43(10):1343–1358. 30

[22] BUZSÁKI, G. (2004). Large-scale recording of neuronal ensembles. *Nature neuroscience*, 7(5): 446–451. 24

[23] CAI, T. et WANG, L. (2011). Orthogonal Matching Pursuit for Sparse Signal Recovery. *Information Theory, IEEE Transactions on*. 61, 62

[24] CARVALHAES, C. et de BARROS, J. A. (2015). The Surface Laplacian Technique in EEG: Theory and Methods. *International Journal of Psychophysiology, Elsevier*. 46

[25] CARVALHAES, C. G., DE BARROS, J. A., PERREAU-GUIMARAES, M. et SUPPES, P. (2014). The joint use of the tangential electric field and surface laplacian in EEG classification. *Brain Topography*, 27(1):84–94. 37, 67

[26] CAUNE, V., RANTA, R., LE CAM, S., HOFMANIS, J., MAILLARD, L., KOESSLER, L. et LOUIS-DORR, V. (2014). Evaluating dipolar source localization feasibility from intracerebral SEEG recordings. *NeuroImage*, 98:118–133. 121

[27] CHEN, S., BILLINGS, S. a. et LUO, W. (1989). Orthogonal least squares methods and their application to non-linear system identification. *International Journal of Control*, 50(5):1873–1896. 62, 63

[28] CICHOCKI, A., CICHOCKI, A., AMARI, S.-I. et AMARI, S.-I. (2002). *Adaptive Blind Signal and Image Processing*. 57

[29] COHEN, M. X. (2014). *Analyzing Neural Time Series*. MIT Press Cambridge, MA, USA. 47

[30] DANNHAUER, M., LANFER, B., WOLTERS, C. H. et KNÖSCHE, T. R. (2011). Modeling of the human skull in EEG source analysis. *Human Brain Mapping*, 32(9):1383–1399. 43

[31] DE MUNCK, J. C. et PETERS, M. J. (1993). A fast method to compute the potential in the multisphere model. *IEEE Transactions on Biomedical Engineering*, 40(11):1166–1174. 41

[32] DENG, S., WINTER, W., THORPE, S. et SRINIVASAN, R. (2012). Improved surface laplacian estimates of cortical potential using realistic models of head geometry. *IEEE Transactions on Biomedical Engineering*, 59(11 PART1):2979–2985. 12, 35, 49, 50, 51, 52, 53, 67, 77, 82, 119

[33] DONOHO, D. et JOHNSTONE, I. (1995). Adapting to unknown smoothness via wavelet shrinkage. *Journal of the american statistical association*, 90:1200–1224. 92

[34] DUCHON, J. (1976). Interpolation des fonctions de deux variables suivant le principe de la flexion des plaques minces. *Revue francaise d'automatique, informatique, recherche operationnelle. Analyse numerique*, 10(3):5–12. 52

[35] DURKA, P. (2007). Matching Pursuit and Unification in EEG Analysis. *Engineering In Medicine And Biology*, pages xii, 184 p., [8] p. of plates. 61

[36] DURKA, P., DURKA, P., BLINOWSKA, K. et BLINOWSKA, K. (2001). A Unified Time Frequency Parametrization of EEGs. *IEEE Engineering in Medicine and Biology*, 20(5):47–53. 61

[37] EDELMAN, ROBERT R AND WARACH, S. (1993). Magnetic Resonance Imaging. *New England Journal of Medicine*, 328(10):708–716. 22

[38] EVRARD, P. (2003). Normal and abnormal development of the central nervous system I. *Developmental medicine and child neurology. Supplement*, 95:7. 18

[39] EYSENCK, H. J. (1958). *Introduction To Psychology*, volume 2. Flat World Knowledge. 18

[40] FERMAGLICH, J. (1982). *Electric Fields of the Brain: The Neurophysics of EEG*, volume 247. Oxford University Press, USA. 44

[41] FRACKOWIAK, RICHARD AND MARKRAM, H. (2015). The future of human cerebral cartography: a novel approach. *Philosophical Transactions of the Royal Society of London B: Biological Sciences*, 370(1668):20140171. 2, 16

[42] FRANK, E. (1952). Electric potential produced by two point current sources in a homogeneous conducting sphere. *Journal of Applied Physics*, 23(11):1225–1228. 39

[43] FUCHS, MANFRED AND WAGNER, MICHAEL AND KOHLER, THOMAS AND WISCHMANN, H.-A. (1999). Linear and nonlinear current density reconstructions. *Journal of clinical Neurophysiology*, 16(3):267–295. 55

[44] GAUTE T. EINEVOLL (2015). Measuring brain activity and modeling what you can measure. 21, 26

[45] GENÇER, N. G. et AKALIN-ACAR, Z. (2005). Use of the isolated problem approach for multi-compartment BEM models of electro-magnetic source imaging. *Physics in medicine and biology*, 50(13):3007–3022. 43

[46] GEODESICS, E., NOTE, T., FERREE, T. et SRINIVASAN, R. (1992). Theory and Calculation of the Scalp Surface Laplacian. pages 1–6. 45, 48

[47] GESELOWITZ, D. B. (1967). On bioelectric potentials in an inhomogeneous volume conductor. *Biophysical journal*, 7(1):1–11. 42

[48] GEVINS, A., LE, J., BRICKETT, P., REUTTER, B. et DESMOND, J. (1991). Seeing through the skull: Advanced EEGs use MRIs to accurately measure cortical activity from the scalp. *Brain Topography*, 4(2):125–131. 44, 45

[49] GLOOR, P. (1975). Contributions of electroencephalography and electrocorticography to the neurosurgical treatment of the epilepsies. *Advances in neurology*, 8:59–105. 29

[50] G.MALLAT, S. et ZHANG, Z. (1993). Matching Pursuits With Time-Frequence Dictionaries. *IEEE transactions on signal processing*, 41(12):3397–3415. 61

[51] GOLUB, GENE H AND VAN LOAN, C. F. (1996). Matrix computations. *Johns Hopkins University, Press, Baltimore, MD, USA*, pages 374–426. 63

[52] GORODNITSKY, I. et RAO, B. (1997). Sparse signal reconstruction from limited data using FOCUSS: a\nre-weighted minimum norm algorithm. *IEEE Transactions on Signal Processing*, 45(3):600–616. 13, 55

[53] GORODNITSKY, I., RAO, B. et GEORGE, J. (1992). Source localization in magnetoencephalography using an iterative\nweighted minimum norm algorithm. *[1992] Conference Record of the Twenty-Sixth Asilomar Conference on Signals, Systems & Computers*, pages 167–171. 55

[54] GORODNITSKY, I. F., GEORGE, J. S. et RAO, B. D. (1995). Neuromagnetic source imaging with FOCUSS: a recursive weighted minimum norm algorithm. *Electroencephalography and clinical neurophysiology*, 95(4):231–251. 67

[55] GOWREESUNKER, B. V. et TEWFIK, A. H. (2009). A Shift Tolerant Dictionary Training Method. *In SPARS'09-Signal Processing with Adaptive Sparse Structured Representations*. 63

[56] GRAMFORT, a., STROHMEIER, D., HAUEISEN, J., HÄMÄLÄINEN, M. S. et KOWALSKI, M. (2013). Time-frequency mixed-norm estimates: Sparse M/EEG imaging with non-stationary source activations. *NeuroImage*, 70:410–422. 60, 120

[57] GRAVE DE PERALTA MENENDEZ, R., GONZALEZ ANDINO, S., LANTZ, G., MICHEL, C. M. et LANDIS, T. (2001). Noninvasive localization of electromagnetic epileptic activity. I. Method descriptions and simulations. *Brain topography*, 14(2):131–7. 91

[58] GRECH, R., CASSAR, T., MUSCAT, J., CAMILLERI, K. P., FABRI, S. G., ZERVAKIS, M., XANTHOPOULOS, P., SAKKALIS, V. et VANRUMSTE, B. (2008). Review on solving the inverse problem in EEG source analysis. *Journal of neuroengineering and rehabilitation*, 5:25. 55

[59] GÜLLMAR, D., HAUEISEN, J. et REICHENBACH, J. R. (2010). Influence of anisotropic electrical conductivity in white matter tissue on the EEG/MEG forward and inverse solution. A high-resolution whole head simulation study. *NeuroImage*, 51(1):145–163. 43

[60] HALLEZ, H., VANRUMSTE, B., GRECH, R., MUSCAT, J., DE CLERCQ, W., VERGULT, A., D'ASSELER, Y., CAMILLERI, K. P., FABRI, S. G., VAN HUFFEL, S., LEMAHIEU, I., et others HALLEZ, HANS AND VANRUMSTE, BART AND GRECH, ROBERTA AND MUSCAT, JOSEPH AND DE CLERCQ, WIM AND VERGULT, ANNELEEN AND D'ASSELER, YVES AND CAMILLERI, KENNETH P AND FABRI, SIMON G AND VAN HUFFEL, S. (2007). Review on solving the forward problem in EEG source analysis. *Journal of neuroengineering and rehabilitation*, 4(1):46. 23

[61] HÄMÄLÄINEN, M. S. et ILMONIEMI, R. J. (1994). *Interpreting measured magnetic fields of the brain:minimun norm estimates*, volume 32. Helsinki University of Technology, Department of Technical Physics. 55

[62] HAMALAINEN, M. S. et SARVAS, J. (1989). Realistic conductivity geometry model of the human head for interpretation of neuromagnetic data. *IEEE Transactions on Biomedical Engineering*, 36(2):165–171. 43

[63] HASHIGUCHI, K., MORIOKA, T., YOSHIDA, F., MIYAGI, Y., NAGATA, S., SAKATA, A. et SASAKI, T. (2007). Correlation between scalp-recorded electroencephalographic and electrocorticographic activities during ictal period. *Seizure*, 16(3):238–247. 29

[64] HAUEISEN, J., TUCH, D. S., RAMON, C., SCHIMPF, P. H., WEDEEN, V. J., GEORGE, J. S. et BELLIVEAU, J. W. (2002). The influence of brain tissue anisotropy on human EEG and MEG. *NeuroImage*, 15(1):159–166. 43

[65] HE, B., LIAN, J. et LI, G. (2001). High-resolution EEG: a new realistic geometry spline Laplacian estimation technique. *Clinical neurophysiology : official journal of the International Federation of Clinical Neurophysiology*, 112(5):845–52. 51

[66] HEBERT, R. et LEHMANN, D. (1977). Theta bursts: an EEG pattern in normal subjects practising the transcendental meditation technique. *Electroencephalography and clinical neurophysiology*, 42(3):397–405. 29

[67] HERMAN, G. T. (2009). *Fundamentals of computerized tomography: Image reconstruction from projection*. 22

[68] HJORTH, B. B. (1975). An on line transformation of EEG scalp potentials into orthogonal source derivations. *Electroencephalography and Clinical Neurophysiology*, 39(5):526–530. 12, 47, 48, 119

[69] H.L. ATTWOOD, W.A., P. M. (1989). *Essentials of Neurophysiology*. 22

[70] HOFMANIS, J. (2013). *Contribution to the cerebral forward model by depth electric stimulation and SEEG measurements: application in epilepsy*. Theses, Universit{\'e} de Lorraine. 43

[71] JUNGHÖFER, M., ELBERT, T., TUCKER, D. M. et BRAUN, C. (1999). The polar average reference effect: A bias in estimating the head surface integral in EEG recording. *Clinical Neurophysiology*, 110(6):1149–1155. 44

[72] KAUR, A. et BUDHIRAJA, S. (2014). Sparse Signal Reconstruction via Orthogonal Least Squares. *2014 Fourth International Conference on Advanced Computing & Communication Technologies*, pages 133–137. 63, 120

[73] KOESSLER, L., BENAR, C., MAILLARD, L., BADIER, J. M., VIGNAL, J. P., BARTOLOMEI, F., CHAUVEL, P. et GAVARET, M. (2010). Source localization of ictal epileptic activity investigated by high resolution EEG and validated by SEEG. *NeuroImage*, 51(2):642–653. 59

[74] KORATS, G., RANTA, R., LE CAM, S. et LOUIS-DORR, V. (2013). Smoothness constraint for cortical dipolar sources estimation. *In Engineering in Medicine and Biology Society (EMBC), 2013 35th Annual International Conference of the IEEE*, pages 6796–6799. IEEE. 69

[75] LALOR, EDMUND C AND KELLY, SIMON P AND FINUCANE, CIAR{\'A}N AND BURKE, ROBERT AND SMITH, RAY AND REILLY, RICHARD B AND MCDARBY, G. (2005). Steady-state VEP-based brain-computer interface control in an immersive 3D gaming environment. *EURASIP journal on applied signal processing*, 2005:3156–3164. 32

[76] LAW, S. K., NUNEZ, P. L. et WIJESINGHE, R. S. (1993). High-resolution EEG using spline generated surface Laplacians on spherical and ellipsoidal surfaces. *IEEE Transactions on Biomedical Engineering*, 40(2):145–153. 49, 50, 51, 78, 79, 80, 81, 82

[77] LESKI, S., WOJCIK, D. K., TERESZCZUK, J., SWIEJKOWSKI, D. a., KUBLIK, E. et WROBEL, A. (2007). Inverse current-source density method in 3D: Reconstruction fidelity, boundary effects, and influence of distant sources. *Neuroinformatics*, 5:207–222. 49

[78] LESKI, SZYMON AND PETTERSEN, KLAS H AND TUNSTALL, BETH AND EINEVOLL, GAUTE T AND GIGG, JOHN AND W{\'O}JCIK, D. K. et WÓJCIK, D. K. (2011). Inverse current source density method in two dimensions: Inferring neural activation from multielectrode recordings. *Neuroinformatics*, 9(4):401–425. 49, 76

[79] L.NUNEZ PAUL et SRINIVASAN RAMESH (2006). Electric Fields of The Brain 2nd edition (2006). 17, 18, 19, 23, 37, 44, 45, 46, 52, 77

[80] LOPES DA SILVA, F. (2004). Functional localization of brain sources using EEG and/or MEG data: Volume conductor and source models. *Magnetic Resonance Imaging*, 22(10 SPEC. ISS.):1533–1538. 23, 24

[81] LOPES DA SILVA, F. H. (2002). Electrical Potentials. *Encyclopedia of the Human Brain*, 2:147–167. 21

[82] LU, Y., WORRELL, G. A., ZHANG, H. C., YANG, L., BRINKMANN, B., NELSON, C. et HE, B. (2014). Noninvasive Imaging of the High Frequency Brain Activity in Focal Epilepsy Patients. *Biomedical Engineering, IEEE Transactions on*, 61(6):1660–1667. 114

[83] MASON, S. G. et BIRCH, G. E. (2003). A general framework for brain-computer interface design. *IEEE transactions on neural systems and rehabilitation engineering : a publication of the IEEE Engineering in Medicine and Biology Society*, 11(1):70–85. 34

[84] MEIJS, J. W. H., WEIER, O. W., PETERS, M. J. et VAN OOSTEROM, a. (1989). On the numerical accuracy of the boundary element method. *IEEE Transactions on Biomedical Engineering*, 36(10): 1038–1049. 43

[85] MICHEL, C. M. et MURRAY, M. M. (2012). Towards the utilization of EEG as a brain imaging tool. *NeuroImage*, 61(2):371–385. 13, 122

[86] MICHEL, C. M., MURRAY, M. M., LANTZ, G., GONZALEZ, S., SPINELLI, L. et GRAVE DE PERALTA, R. (2004). EEG source imaging. *Clinical Neurophysiology*, 115(10):2195–2222. 57, 59, 67

[87] MILLÁN, J. D. R. et MOURIÑO, J. (2003). Asynchronous BCI and local neural classifiers: An overview of the adaptive brain interface project. *IEEE Transactions on Neural Systems and Rehabilitation Engineering*, 11(2):159–161. 27

[88] MITZDORF, U. (1985). Current source-density method and application in cat cerebral cortex: investigation of evoked potentials and EEG phenomena. *Physiological reviews*, 65(1):37–100. 48, 49, 75

[89] MIZUKI, Y., TANAKA, M., ISOZAKI, H., NISHIJIMA, H. et INANAGA, K. (1980). Periodic appearance of theta rhythm in the frontal midline area during performance of a mental task. *Electroencephalography and Clinical Neurophysiology*, 49(3):345–351. 29

[90] MOSHER, J. C., BAILLET, S. et LEAHY, R. M. (1999). EEG source localization and imaging using multiple signal classification approaches. *Journal of clinical neurophysiology : official publication of the American Electroencephalographic Society*, 16(3):225–238. 58

[91] MOSHER, J. C. et LEAHY, R. M. (1998). Recursive MUSIC: A framework for EEG and MEG source localization. *IEEE Transactions on Biomedical Engineering*, 45(11):1342–1354. 13, 58, 59, 103, 107

[92] MOSHER, J. C. J., LEWIS, P. S. P. et LEAHY, R. M. R. (1992). Multiple dipole modeling and localization from spatio-temporal MEG data. *IEEE Transactions on Biomedical Engineering*, 39(6): 541–557. 58

[93] MULLINGER, K. et BOWTELL, R. (2011). Combining EEG and fMRI. *Methods Mol Biol*, 711:303–326. 31

[94] NUNEZ, P. L. et WESTDORP, a. F. (1994). The surface Laplacian, high resolution EEG and controversies. *Brain topography*, 6(3):221–226. 44

[95] OOSTENVELD, R., FRIES, P., MARIS, E. et SCHOFFELEN, J. M. (2011). FieldTrip: Open source software for advanced analysis of MEG, EEG, and invasive electrophysiological data. *Computational Intelligence and Neuroscience*, 2011:1. 77

[96] PAKKENBERG, B. et GUNDERSEN, H. J. G. (1997). Neocortical neuron number in humans: Effect of sex and age. *Journal of Comparative Neurology*, 384(2):312–320. 19

[97] PASCUAL-MARQUI, R. D. (2007). Discrete, 3D distributed, linear imaging methods of electric neuronal activity. Part 1: exact, zero error localization. pages 1–16. 55

[98] PASCUAL-MARQUI, R. D., MICHEL, C. M. et LEHMANN, D. (1994). Low resolution electromagnetic tomography: a new method for localizing electrical activity in the brain. *International Journal of Psychophysiology*, 18(1):49–65. 55

[99] PATI, Y. C., REZAIIFAR, R. et KRISHNAPRASAD, P. S. (1993). Orthogonal matching pursuit: recursive function approximation with applications to wavelet decomposition. *Proceedings of 27th Asilomar Conference on Signals, Systems and Computers*, pages 1–5. 61

[100] PERRIN, F., PERNIER, J., BERTRAND, O. et ECHALLIER, J. F. (1989). Spherical splines for scalp potential and current density mapping. *Electroencephalography and clinical neurophysiology*, 72(2):184–7. 12, 50

[101] PETTERSEN, K. H., DEVOR, A., ULBERT, I., DALE, A. M. et EINEVOLL, G. T. (2006). Current-source density estimation based on inversion of electrostatic forward solution: Effects of finite extent of neuronal activity and conductivity discontinuities. *Journal of Neuroscience Methods*, 154(1-2):116–133. 48, 49, 76

[102] PFURTSCHELLER, G., NEUPER, C., GUGER, C., HARKAM, W., RAMOSER, H., SCHLOGL, a., OBERMAIER, B. et PREGENZER, M. (2000). Current trends in Graz Brain-Computer Interface (BCI) research. *IEEE Transactions on Rehabilitation Engineering*, 8(2):216–219. 33

[103] POLONSKY, A. et ZIBULEVSKY, M. (2004). *MEG/EEG source localization using spatio-temporal sparse representations*. Springer. 90

[104] POTTER, LEE C AND ARUN, K. (1989). Energy concentration in band-limited extrapolation. *Acoustics, Speech and Signal Processing, IEEE Transactions on*, 37(7):1027–1041. 55

[105] RANTA, R. et LOUIS-DORR, V. V. (2010). Hysteresis Thresholding: A Graph-Based Wavelet Block Denoising Algorithm. *The Open Signal Processing Journal*, 3(1):6–12. 92

[106] RISSANEN, J. (1978). Modeling by shortest data description. *Automatica*, 14(5):465–471. 57, 103

[107] RUSH, S. et DRISCOLL, D. a. (1969). EEG electrode sensitivity-an application of reciprocity. *IEEE transactions on bio-medical engineering*, 16(1):15–22. 40

[108] SANEI, S. et CHAMBERS, J. (2007). *EEG Signal Processing*. Wiley-Interscience. 15, 19, 22, 26, 27, 29, 32, 38

[109] SARVAS, J. (1987). Basic mathematical and electromagnetic concepts of the biomagnetic inverse problem. *Physics in medicine and biology*, 32(1):11–22. 39, 42

[110] SATO, N. et YAMAGUCHI, Y. (2007). Theta synchronization networks emerge during human object-place memory encoding. *Neuroreport*, 18(5):419–424. 29

[111] SCHERG, M. (1990). Fundamentals of Dipole Source Potential Analysis. *Auditory evoked magnetic fields and electric potentials. Advances in audiology*, 6:40–69. 24, 25, 59

[112] SCHMIDT, R. (1986). Multiple emitter location and signal parameter estimation. *IEEE Transactions on Antennas and Propagation*, 34(3):276–280. 58

[113] SHARBROUGH, F. W. (1999). Nonspecific abnormal EEG patterns. *Electroencephalography. Basic Principles, Clinical Applications, and Related Fields*, pages 215–234. 32

[114] SOUSSEN, C., IDIER, J., BRIE, D. et DUAN, J. (2011). From Bernoulli Gaussian deconvolution to sparse signal restoration. *IEEE Transactions on Signal Processing*, 59(10):4572–4584. 60, 62, 63, 64, 65

[115] SOUSSEN, C., IDIER, J., DUAN, J. et BRIE, D. (2014). L2-L0 regularization path tracking algorithms. (28):1–28. 65

[116] SPRUSTON, N. (2008). Pyramidal neurons: dendritic structure and synaptic integration. *Nature reviews. Neuroscience*, 9(3):206–221. 21

[117] SQUIRE, L. R. et ZOLA-MORGAN, S. (1991). The medial temporal lobe memory system. *Science (New York, N.Y.)*, 253(5026):1380–1386. 18

[118] STANGOR, C. (2010). *Introduction to psychology. Flat World Knowledge*. 20

[119] STENROOS, M. et HAUK, O. (2013). Minimum-norm cortical source estimation in layered head models is robust against skull conductivity error. *NeuroImage*, 81:265–72. 55

[120] STENROOS, M., MÄNTYNEN, V. et NENONEN, J. (2007). A Matlab library for solving quasi-static volume conduction problems using the boundary element method. *Computer Methods and Programs in Biomedicine*, 88(3):256–263. 39, 76, 97, 98, 108

[121] STOK, J. C. (1986). The inverse problem in {EEG} and {MEG} with application to visual evoked responses. 40

[122] SWARTZ, B. E. (1998). The advantages of digital over analog recording techniques. *Electroencephalography and Clinical Neurophysiology*, 106(2):113–117. 10

[123] TADEL, F. F., BAILLET, S., MOSHER, J. C., PANTAZIS, D. et LEAHY, R. M. (2011). Brainstorm: A user-friendly application for MEG/EEG analysis. *Computational Intelligence and Neuroscience*, 2011:8. 76, 96, 98, 116

[124] TALAIRACH, J., BANCAUD, J. et SZIKLA, G. (1974). Approche Nouvelle De La Neurochirugie De L'Epilepsie. Méthodologie Stérérotaxique Et Résultats Thérapeutiques. *Neurochirurgie*, 20:1–240. 29

[125] TANDONNET, C., BURLE, B., HASBROUCQ, T. et VIDAL, F. (2005). Spatial enhancement of EEG traces by surface Laplacian estimation: comparison between local and global methods. *Clinical neurophysiology : official journal of the International Federation of Clinical Neurophysiology*, 116(1):18–24. 48, 49

[126] TEPLAN, M. (2002). FUNDAMENTALS OF EEG MEASUREMENT M . Teplan. 2:1–11. 22

[127] THICKBROOM, G. W., MASTAGLIA, F. L., CARROLL, W. M. et DAVIES, H. D. (1984). Source derivation: application to topographic mapping of visual evoked potentials. *Electroencephalography and clinical neurophysiology*, 59(4):279–285. 48

[128] TIBSHIRANI, R. (1996). Regression shrinkage and selection via the lasso. *Journal of the Royal Statistical Society. Series B (Methodological)*, pages 267–288. 60

[129] TROPP, J. et GILBERT, A. (2007a). Signal recovery from partial information via orthogonal matching pursuit. *IEEE Trans. Inform. Theory*, 53(12):4655–4666. 62

[130] TROPP, J. a. et GILBERT, A. C. (2007b). Signal recovery from random measurements via orthogonal matching pursuit. *IEEE Transactions on Information Theory*, 53(12):4655–4666. 61, 62

[131] VALLABHANENI, A., WANG, T. et HE, B. (2005). Brain - Computer Interface. *In Neural Engineering*, pages 85–121. Springer. 33, 34

[132] VALLAGHE, S. (2008). *Modelisation du probleme direct de la magneto et electroencephalographie: methodes numeriques et calibration*. Thèse de doctorat, Universite Nice Sophia Antipolis. 30, 43

[133] VAN VEEN, B. D. et BUCKLEY, K. M. (1988). Beamforming: A versatile approach to spatial filtering. 57

[134] VARELA, F., LACHAUX, J.-P., RODRIGUEZ, E. et MARTINERIE, J. (2001). The brainweb: phase synchronization and large-scale integration. *Nature reviews neuroscience*, 2(4):229–239. 29

[135] VESPIGNANI, H. (2003). *L'EEG - De la Technique à la Clinique*. John Libbey Eurotext, Novartis. 29

[136] WANG, Z., MAIER, A., LEOPOLD, D. A., LOGOTHETIS, N. K. et LIANG, H. (2007). Single-trial evoked potential estimation using wavelets. *Computers in Biology and Medicine*, 37(4):463–473. 91, 121

[137] WAX, M. et KAILATH, T. (1985). Detection of signals by information theoretic criteria. *Acoustics, Speech and Signal Processing, IEEE Transactions on*, 33(2):387–392. 57

[138] WICKELGREN, I. (2003). Neuroscience. Tapping the mind. *Science (New York, N.Y.)*, 299(5606):496–499. 33

[139] WOLPAW, J. R., BIRBAUMER, N., HEETDERKS, W. J., MCFARLAND, D. J., PECKHAM, P. H., SCHALK, G., DONCHIN, E., QUATRANO, L. a., ROBINSON, C. J. et VAUGHAN, T. M. (2000). Brain-computer interface technology: A review of the first international meeting. *IEEE Transactions on Rehabilitation Engineering*, 8(2):164–173. 33

[140] WU, S. C. et SWINDLEHURST, A. L. (2013). Matching Pursuit and Source Deflation for Sparse EEG/MEG Dipole Moment Estimation. *Biomedical Engineering, IEEE Transactions on*, 60(8):2280–2288. 63, 64, 103, 105, 107, 120

[141] WU, X.-F., LANG, Z.-Q. et BILLINGS, S. a. (2005). An Orthogonal Least Squares based approach to FIR designs. *International Journal of Automation and Computing*, 2(2):163–170. 62

[142] YAO, D. (2000). Electric Potential Produced by a Dipole in a Homogeneous Conducting Sphere. *Ieee Transactions on Biomedical Engineering*, 47(7):964–966. 39

[143] ZHANG, T. (2008). Adaptive forward-backward greedy algorithm for sparse learning with linear models. *Advances in Neural Information Processing Systems 21*, (1):1–8. 63

[144] ZIBULEVSKY, M., PEARLMUTTER, B. *et al.* (2001). Blind source separation by sparse decomposition in a signal dictionary. *Neural computation*, 13(4):863–882. 94

Declaration

I herewith declare that I have produced this paper without the prohibited assistance of third parties and without making use of aids other than those specified; notions taken over directly or indirectly from other sources have been identified as such. This thesis has not previously been presented in identical or similar form to any other examination board.

December 18, 2015, Nancy

Résumé

L'imagerie de sources corticales joue un rôle important pour la compréhension des mécanismes fonctionnels et pathologiques du cerveau. Elle permet de relier l'activation de certaines zones corticales en réponse à un stimulus cognitif donné, et ainsi d'étudier les co-activations des réseaux fonctionnels sous-jacents. Parmi les modalités d'acquisition à disposition, les mesures électroencéphalographiques (EEG) ont le grand avantage de fournir une résolution temporelle de l'ordre de la millisecondes à l'échelle des processus étudiés, tout en demeurent une technique non-invasive exploitée en routine clinique. Cependant l'identification des sources activées à partir d'enregistrements EEG reste une tâche extrêmement difficile en raison de la faible résolution spatiale de cette modalité, de l'effet de filtrage important de l'os crânien et des erreurs inhérentes au modèle de propagation à inverser. Dans cette thèse, différentes approches pour l'estimation de l'activité corticale de surface à partir de l'EEG ont été explorées. Les méthodes d'imagerie corticales les plus simples se basent uniquement sur des caractéristiques géométriques de la tête. La charge de calcul est très réduite et les modèles utilisés sont simples à mettre en oeuvre. En revanche, de tels approches n'apportent pas d'informations précises sur les générateurs neuronaux ainsi que sur leurs propriétés spatio-temporelles. Des techniques plus élaborées peuvent alors être employées pour construire un modèle de propagation réaliste, et ainsi reconstruire plus précisément les sources par inversion. En revanche, le problème d'inversion de ce modèle est sévèrement mal posé, et des contraintes doivent être imposées pour réduire l'espace des solutions. Nous avons d'abord repris le problème de l'imagerie de sources corticales en se basant uniquement sur les activités électriques fournis par les mesures EEG de surface. Les méthodes développées reposent sur des considérations simplifiées mais universelles sur la géométrie de la tête ainsi que sur les caractéristiques de propagation physiologiques des sources. Les opérateurs à appliquer aux données sont des matrices de plein rang, semblable aux méhodes par Laplacien de surface (SL), et sont basées sur l'hypothèse que les données de surface sont faites d'un mélange linéaire de fonctions de base radiale produites par les sources sous-jacentes. Dans la deuxième partie de la thèse, nous levons la contrainte de rang plein en adoptant des modèles de dipoles distribués. Pour ce faire, une régularisation de type parcimonie est développée en s'appuyant sur l'hypothèse physiologique que seules quelques sources corticales sont actives simultanément, une hypothèse bien adaptée au contexte de sources épileptiques ou encore dans le cas de tâches cognitives. Cette contrainte est imposée à la fois dans les dimensions spatiale et temporelle des mesures. Deux dictionnaires d'atomes spatio-temporelles sont proposés, l'un construit par analyse en composantes principales des données, le second exploitant une décomposition sur une base d'ondelettes, plus robuste au bruit et bien adapté à la nature non-stationnaire des données électrophysiologiques. L'ensemble des méthodes proposées ont été testées sur des données simulées et comparées à des approches classiques de la littérature. Les performances obtenus sont satisfaisantes et montrent une bonne robustesse dans des conditions de rapport signal à bruit difficiles. Nous avons également validé nos approches sur des données réelles épileptiques fournies et expertisées par les neurologues du Centre Hospitalier Universitaire de Nancy affiliés au projet. Les localisations estimées concordent avec la détermination de la zone épileptogène obtenue par exploration intracérébrale en Stéréo-EEG.

Mots-clés: EEG, Problème inverse, Imagerie de sources corticales, Solutions Parcimonieuses

Abstract

Cortical source imaging plays an important role for the comprehension of the functional or pathological brain. It allows to relate the activation of particular cortical areas in response to a given cognitive stimuli, hence to study the co-activations of underlying functional networks. It is also helpful in identifying the location of pathological activities. Various methods of clinical investigation can be used, from imaging modalities (PET, MRI) to electroencephalography (EEG, SEEG, MEG). The electroencephalographic (EEG) measurements have the great advantage to yield very high temporal resolution in milliseconds while being a non-invasive technique often used in primary clinical investigation. However the identification of the activated sources from EEG recordings remains an extremely difficult task due to the low spatial resolution this modality provides, to the smearing effect of the skull, to propagation model errors, as well as spatial (location and size) and temporal (synchronization) properties of the sources. In this thesis, different path to the estimation of cortical activities based on the EEG have been explored. Simplest cortical imaging methods requires only the assumptions of the geometrical properties of the head. Second order derivation of the interpolated scalp recordings removes smearing effect of the skull and yields an approximate estimation of the dura potentials. Despite small computational burden and simplified models such estimation do not provide accurate information about the individual neural generators nor their spatio-temporal properties. To overcome this, more elaborated models are used to construct realistic forward model and, thus, localize the sources by inverting it. In addition to the difficulty of forward model construction, inversion step requires regularization and/or sparsity constrains. Although dozens of methods already exists in the literature, only few are designed for the non-stationary nature of the unknown number of the sources. We reconsider the problem of cortical source imaging using as less information as possible in addition to the electrical activities provided through the EEG scalp measurements. We have avoided statistical assumptions due to the poor amount of physiological considerations they are able to integrate, and we have rather focused on methods that rely on basic geometrical and physiological considerations. Resulting full rank estimator is at the root of a large family of interpolation-based Surface Laplacian (SL) methods, based on the assumption that the scalp map is made of a linear mixing of smooth basis functions produced by the underlying sources. In the second part of the thesis, we relax the full rank constraint by adopting a dipolar distributed model and we follow the assumption that only a few cortical sources are simultaneously active. Such hypothesis is particularly valid in e.g., epileptic context or in the case of cognitive tasks, where a limited number of sources are responsible of the visible activity on the EEG electrodes. To enforce the regularization as well as the sparsity of the solution, we take benefit of the temporal dimension of the data, and propose two combined data-driven spatio-temporal dictionaries. At first the temporal atoms are learned based on a principal component analysis. Finally we exploit a time-frequency decomposition of the data based on wavelets, being more robust to noise and well adapted to the non-stationary nature of the electrophysiologic data.

Keywords: EEG, Inverse problem , Cortical Source Imaging, Sparse solutions